Narrow-Line Cooling Light for a Magneto-Optical Trap of Erbium Atoms

master thesis

by

Alexander Rietzler

submitted to the Faculty of Mathematics, Computer Science and Physics of the University of Innsbruck

in partial fulfillment of the requirements for the degree of master of science

advisor:
Prof. Dr. Francesca Ferlaino,
Institute of Experimental Physics, University of Innsbruck

Innsbruck, September 2012

Summary

In this thesis, we describe the main steps for the production and stabilization of the laser light used to cool erbium atoms in a magneto-optical trap (MOT). The line that we use for the MOT has a narrow-line character with a 190-kHz linewidth and has a wavelength of 583 nm.

To generate the light at 583 nm, we use a dye laser, operated with Rhodamine 6G. The laser light from the dye laser has a linewidth of about 1 MHz and a frequency drift of about 100 MHz/h. For MOT operation, we need to reduce the laser linewidth and to stabilize the laser on the resonance frequency for the different Er isotopes. For this purpose, we use a pre-locking cavity, which narrows the linewidth down to 45 kHz and we build a ultra low expansion (ULE) cavity for long-term frequency stability. A special and convenient feature of our stabilization scheme is that it allows locking of the cooling light on the atomic transition of each Er isotope in a very straightforward manner - it can in fact bridge the isotope shifts, corresponding to several GHz.

The part of our locking setup that is responsible for long-term frequency stability is based on the Pound-Drever-Hall locking technique in combination with a home-build ULE cavity. This cavity is made of ultra low expansion glass, which we cool down to the zero-expansion temperature. At this temperature, the thermal expansion of the cavity is minimized. By stabilizing the laser to the ULE cavity, we reduce the long-term drift to 0.16 Hz/s.

Using this light, we cooled down the five most abundant erbium isotopes to 15 μK in the MOT, and recently we achieved the first BEC of erbium atoms.

Zusammenfassung

In dieser Arbeit werden die entscheidenen Schritte für die Produktion und Stabilisierung von Laserlicht beschrieben, welche für das Kühlen von Erbium Atomen in einer magneto-optischen Falle (MOT) benötigt werden. Der schmalbandige MOT-Übergang hat eine Linienbreite von 190 kHz und eine Wellenlänge von 583 nm.

Für die Erzeugung dieses Lichts verwenden wir einen mit Rhodamin 6G betriebenen Farbstofflaser. Dieser Laser emittiert Licht mit einer Linienbreite von ca. 1 MHz, die Frequenz des Lichts driftet mit einer Rate von ca. 100 MHz/h. Für den Betrieb der MOT ist es notwendig die Linienbreite zu reduzieren und den Laser auf die Resonanzfrequenzen der verschiedenen Erbium Isotope zu stabilisieren. Für diesen Zweck verwenden wir einen optischen Resonator zur Reduktion der Linienbreite auf ca. 45 kHz und einen zweiten, selbst gebauten optischen Resonator zur Erreichung der Langzeitstabilität des Laserlichts. Eine spezielle Eigenschaft unseres Aufbaus zur Frequenzstabilisierung ist, dass es sehr einfach ist, die Frequenz in Resonanz mit den Übergängen der verschiedenen Isotope zu stabilisieren - eine Verschiebung des Stabilisierungsbereichs entsprechend der Isotopenverschiebungen von mehreren GHz ist möglich.

Der Teil unseres Aufbaus, der für die Langzeitstabilisierung des Laserlichts verantwortlich ist, basiert im Wesentlichen auf dem Pound-Drever-Hall-Verfahren in Verbindung mit einem optischen Resonator aus “ultra low expansion” Glas (ULE), welches einen sehr geringen thermischen Ausdehnungskoeffizienten besitzt. Wir regeln die Temperatur des optischen Resonators auf eine bestimmte Temperatur (“zero-expansion temperature”), bei welcher die Wärmeausdehnung des optisches Resonators vernachlässigt werden kann. Nach Stabilisierung des Lasers auf den ULE Resonator erzielen wir eine Frequenzdrift von 0.16 Hz/s, gemessen über den Zeitraum von ca. einem Monat.

Wir verwenden das Licht zum Kühlen der fünf meist vorkommenden Erbium Isotope in einer MOT und erzielen dabei eine Temperatur von 15 µK.
Erst kürzlich gelang es uns, das erste BEC von Erbium Atomen zu erzeugen.

Danksagung

First of all I want to thank Francesca for giving me the opportunity to do my master thesis in the erbium team. I want to thank her for her support in preparing my seminar talk and for the assistence in writing this thesis, especially during the time of my community service. I am also thankful for allowing me to work independently on such an important part of our project.

Furthermore I want to express my gratitude to Rudi Grimm - the research group he built up is very professional and has been a supporting and pleasant environment for me.

Besonderer Dank gilt auch den Institutsmitarbeitern. Zu nennen ist hier Nicole, die sehr viele meiner Bestellungen entgegen nehmen musste, Helmut für seine energiereichen Unterhaltungen und seine Unterweisung im Drehen. Mathias und Toni haben einen großen Beitrag zur Realisierung der Cavity geleistet.

Ich möchte mich herzlich bei allen Gruppenmitgliedern - Diplomstudenten, Doktoranden und Post-Doktoranden - bedanken. Besonders viel verdanke ich Hans, von ihm konnte ich einiges vom Design der Cavity übernehmen. Raffaels Know-How über das optische Kontaktieren ersparte mir viel Zeit im Reinraum. Dank an Benjamin, der mich auf viele Probleme aufmerksam gemacht hat, die beim Zusammenbau einer Cavity auftreten können.

Vielen Dank an das Erbium Team. Interessante und lehrreiche Diskussionen bei Almdudler, Prinzenrollen und Thorlabs-Süßigkeiten haben mir sozusagen die Arbeitszeit versüßt. Albert lehrte mich wie man Probleme am besten anpackt und ohne sein technisches und elektronisches Wissen wäre vieles nicht möglich gewesen. Kiyotaka half mir sehr bei den vielen Messungen und ohne seine magischen Hände wäre der Farbstofflaser nicht so schnell angesprungen - Thanks a lot! Die Unterhaltungen mit Johannes und die lockeren Sprüche von Michi wären auch nicht wegzudenken gewesen.

Spezieller Dank gilt Stefan. Danke für die vielen Korrekturen und Verbesserungsvorschläge für die schriftliche Arbeit und für die langjährige Freundschaft und Zusammenarbeit während des Studiums.

Es gebührt natürlich auch vielen Menschen Dank, die nicht direkt an meiner Arbeit beteiligt waren, mich aber in allen Belangen großzügig unterstützt und geprägt haben und somit dieses Studium erst möglich gemacht haben. An erster Stelle steht meine Familie.

Ich danke meiner Mutter für all die philosophischen Diskussionen rund um die Physik und ihr grenzenloses Vertrauen in mich. Ich danke meinem Vater für die Entscheidungshilfe kurz vor Beginn meines Physikstudiums. Danke Martin und und Laura, ohne euch wäre das Leben nur halb so schön. Vielen Dank an meinen Onkel Stefan, der es immer wieder schafft, dank des Einflusses von Raumschiff Enterprise, mich daran zu erinnern, dass das scheinbar Unmögliche vielleicht doch möglich sein könnte. Dank an meinen Großvater - ich glaube zwar

immer noch nicht an UFOs, aber unsere Diskussionen haben mich dem wissenschaftlichen Denken wesentlich näher gebracht. Danke auch an alle in meiner Familie, dass ich immer auf euch zählen kann.

Contents

Introduction

At temperatures near absolute zero, atomic gases begin to reveal their quantum behavior and fascinating effects can be observed. A key feature is the high level of control over the interparticle interaction, which allows us to study phenomena that are strongly connected to other branches of research like high-temperature superconductivity [Chi06], quantum chemistry [Osp10], condensed matter [Gre08] and few body physics [Fer10].

The achievement of the first Bose-Einstein condensation in 1995 marked the beginning of a rapid growth in the field of ultracold quantum gases [And95, Bra95, Dav95]. A further important development has been the cooling of atomic Fermi gases well below the degeneracy temperature [DeM99, Tru01, Sch01]. The large majority of experiments have been performed with elements from the alkali series, as these atoms show isotropic contact-like interaction and provide suitable optical transitions for laser cooling.

The progresses made in cooling and trapping alkali atoms have stimulated studies on more exotic species for ultracold gas experiments [Ste09, Esc09, Kra09]. Of particular interest are the atomic species, which interact via dipole-dipole interaction (DDI). The anisotropic and long-range character of the DDI leads to totally new phenomena in quantum systems. Predictions show spectacular quantum phases and new kind of experiments exploiting the geometry-dependent tunability in these systems [Lah09, Bar08]. Systems with DDI are atoms with a permanent magnetic dipole moment. Another example are polar molecules, which carry an electric dipole moment.

Up to the moment three species of magnetic atoms have been Bose condensed. Among them are a condensate of chromium [Gri05], dysprosium [Lu11] and erbium[1] [Aik12]. Chromium was the first dipolar atom to be Bose condensed by the group of T. Pfau in Stuttgart [Gri05] and later by the group of O. Gorcieux in Paris [Bea08]. With Cr, many fascinating effects have been observed. Among all, the most spectacular is the d-wave collapse of the Bose gas [Lah08].

In order to increase the dipolar strength, novel species with higher magnetic moments have to be considered. With the recent BECs of dysprosium by the Group of B. Lev at Stanford [Lu11] and of erbium by our group in Innsbruck [Aik12], strongly dipolar gases are now available in the laboratories.

As a rare earth element with multivalence-electrons character, Er has a very rich atomic spectrum, which opens up many opportunities for laser cooling. Narrow, intermediate and broad optical transitions are thus available [Han04, McC06b, Ber08].

Our main experimental goal is the creation of the first BEC of erbium atoms. With an

[1] During writing of this thesis, our group achieved a Bose-Einstein condensate of erbium.

ultracold sample, we plan to investigate the unknown scattering properties of Er, to produce Feshbach molecules, and to explore few-body physics with DDI.

The first fundamental step towards quantum degeneracy requires the application of laser cooling - laser cooling has proven to be a very powerful technique to cool the atoms by orders of magnitude down to the μK regime [Met99]. In this context, erbium is a rather unknown species. The first magneto-optical trap of Er has been demostrated at NIST by the group of J.J McClelland, using a broad $J \rightarrow J + 1$[2] transition at 401 nm. Although the 401-nm line has the advantage to produce a strong radiation force, this transition has the drawback of not being optically closed and to have a high Doppler temperature[3]. Inspired by works on Ca [Kra09], Sr [Ste09], Yb[Py09], we choose a narrow-line transition at 583 nm for MOT operation.

The purpose of my master thesis was to create narrow-line cooling light, which we use for magneto-optical trapping (MOT) of the erbium atoms. For creation of the light, we use a dye laser, which is locked to a self-made ultra low expansion (ULE) cavity. The setting up of the locking setup including the construction of the ULE cavity has been the main part of my work.

This thesis is structured as follows. In Chap. 1 we discuss properties of erbium, which are relevant for the MOT. The requirements for the cooling light are outlined.

Chapter 2 explains the setup of the dye laser. Chapter 3 decribes the ULE cavity including construction details and temperature stabilization. In Chap. 4 the optical setup needed for creation of the cooling light is explained as well as details of our locking technique. Chapter 5 shows the results of the measurements done on the cavity performance and the laser linewidth. Finally, Chap. 6 concludes and gives a short outlook on the future of our experiment.

[2] J is the total angular momentum quantum number

[3] Cooling limit for Doppler cooling

Chapter 1

Erbium

Erbium is a chemical element with an atomic number of 68. It belongs to the lanthanide series and it is part of a set of 17 elements with similar geochemical properties, the so-called rare earth metals. In the field of ultracold quantum gas experiments, there is an increasing interest on those elements, since they have exotic level schemes with several transitions suited for laser cooling. Further, most of the rare earth elements have a high magnetic moment, which allows the investigation of dipolar effects.

In this Chapter, we discuss properties of erbium relevant to our experiment, in particular the energy level scheme of Er and the laser cooling transitions we use and may want to use in the future. Finally, we discuss the requirements for the light which we use for magneto-optical trapping of Er.

1.1 Laser cooling transitions

The ground state configuration for Er is [Xe]$4f^{12}6s^2$, where [Xe] means that the electronic shells are filled with electrons up to the $5p$ shell like in [Xe]. In addition, two of the remaining valence electrons fill up the $6s$ shell, whereas the subjacent $4f$ shell is filled with 12 electrons having a two-electron vacancy. This kind of structure is called submerged shell structure, which results in a rich, complex energy level scheme [Ban05, Mar78]; see Fig. 1.1.
Erbium possesses six stable isotopes. Five of them are bosons, which have no hyperfine structure because the nuclear spin quantum number I is zero. This means that the relevant quantum number describing the different transitions is the total angular momentum quantum number J.

In Fig. 1.1, 110 levels of erbium with J ranging from 2 to 12 are shown. Black marked horizontal lines indicate even parity states, whereas odd parity states are shown in red. The arrows identify 5 different transitions, which have been proposed to be suitable for laser cooling applications [McC06b]. These dipole-allowed transitions couple the $J = 6$ ground state to an excited state with $\Delta J = +1$ and opposite parity [Dra96].

For describing the quantum states of erbium, we need two different angular momenta coupling schemes. If the coulomb interaction is dominant over the spin-orbit (LS-) coupling, the spin $\vec{s}_i$ of each electron adds up to the total electron spin $\vec{S} = \sum_i \vec{s}_i$. The same is true for

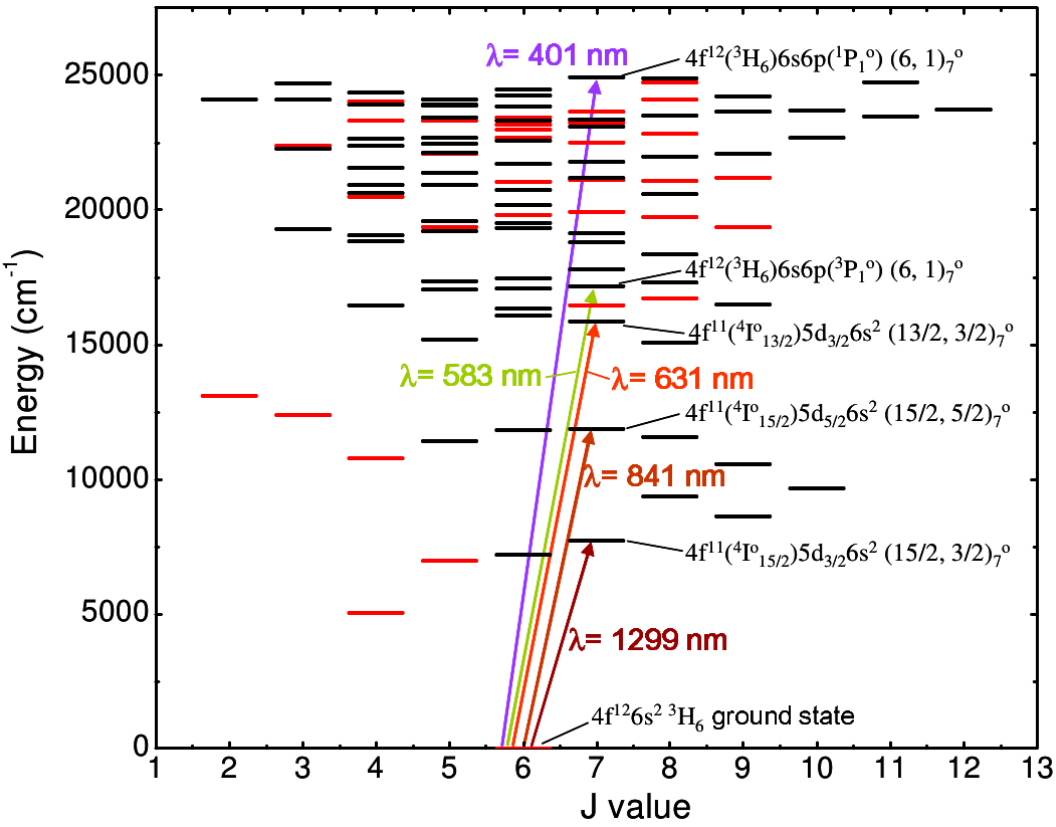

Figure 1.1: Level scheme of atomic erbium. Black (red) horizontal lines indicate even (odd) parity states. Five transition marked by arrows have been identified to be suited for cooling and trapping of Er [Ban05]. So far we use the 401-nm and the 583-nm transition in our experiment. Grafic taken from [Ban05].

the total angular momentum, $\vec{L} = \sum_i \vec{l}_i$. The total spin and total orbital angular momentum then couple to the total angular momentum, $\vec{J} = \vec{L} + \vec{S}$ [Dem05]. The resulting quantum state is denoted by ${}^{2s+1}L_J$. The L states are labeled with the following letters [Dra96].

L	0	1	2	3	4	5	6	...
symbol	S	P	D	F	G	H	I	...

This coupling scheme is often used to describe light elements.
In the case of heavier atoms, which have a large nuclear charge, the spin-orbit interaction becomes stronger than the interaction between individual spins or orbital angular momenta. Here, the spin and orbital angular momentum of each electron couples individually to form an individual angular momentum, $\vec{J}_i = \vec{L}_i + \vec{S}_i$. These momenta then add up to the total angular momentum $\vec{J} = \sum_i \vec{J}_i$. This coupling scheme is referred to as the jj-coupling.
For the lanthanides, a special case of this scheme, the J_1J_2-coupling, is applied to describe many of the excited states [Wyb07]. Here, the $4f$ electrons and the remaining outer electrons couple independently via LS-coupling to form two states with $\vec{J}_1$ and $\vec{J}_2$, which then add up to a total angular momentum. These states are labeled with $(J_1, J_2)_J$.

The $4f^{12}6s^2$ electrons in the outer shells of the Er ground state follow a LS-coupling scheme, which gives a $^3\mathrm{H}_6$ term. Other states of erbium, e.g. the 583-nm transition, which we use for the MOT, is described by J_1J_2 coupling.
This state is denoted as $[\mathrm{Xe}]4f^{12}(^3\mathrm{H}_6)6s6p(^3\mathrm{P}_1^0)(6,1)_7^0$, where one of the electrons in the $6s$ shell is excited to the $6p$ shell. In this expression, the $4f$ electrons couple to a $^3\mathrm{H}_6$ term, whereas the two $6s6p$ electrons couple to a $^3\mathrm{P}_1^0$ state. The superscript '0' indicates odd parity of the state. Here, the $6p$ electron changes its spin state, which leads to a narrower transition compared to the 401-nm transition. These kind of transitions are called intercombination lines.

Table 1.1 lists the main relevant parameters for laser cooling of the five transitions marked in Fig. 1.1.

	transition				
parameter	400.91 nm	582.84 nm	631.04 nm	841.22 nm	1299.21 nm
$\Gamma\,(\mathrm{s}^{-1})$	1.7×10^8	1.2×10^6	1.8×10^5	5.0×10^4	13
τ	5.8 ns	0.857 µs	5.6 µs	20 µs	75 ms
$\Delta\nu$	27.5 MHz	190 kHz	28 kHz	8.0 kHz	2.1 Hz
I_{sat}	55.7 $\mathrm{mW/cm^2}$	0.13 $\mathrm{mW/cm^2}$	15 $\mathrm{\mu W/cm^2}$	1.8 $\mathrm{\mu W/cm^2}$	0.13 $\mathrm{nW/cm^2}$
T_{Doppler}	659 µK	4.8 µK	680 nK	190 nK	51 pK
v_{Doppler}	0.26 m/s	15 mm/s	5.8 mm/s	3.1 mm/s	50 µm/s
T_{recoil}	717 nK	170 nK	140 nK	81 nK	34 nK
v_{recoil}	6.0 mm/s	4.1 mm/s	3.8 mm/s	2.8 mm/s	1.8 mm/s

Table 1.1: Laser cooling parameters for five transitions in Er: spontaneous decay rate Γ, lifetime τ, linewidth full width at half maximum (FWHM) $\Delta\nu$, saturation intensity I_{sat}, Doppler temperature T_{Doppler}, Doppler velocity v_{Doppler}, recoil temperature T_{recoil} and recoil velocity v_{recoil}. Parameters are taken from Ref. [Ban05] with corrections from [McC06a, Den10, Fri12].

The scattering force acting on an atom resonant to a laser is proportional to the linewidth of the transition used. At the same time, the linewidth limits the Doppler temperature, which is the fundamental limit of the Doppler cooling mechanism[1]. Therefore, it is beneficial to use combinations of strong lines and narrow lines to cool atoms down to very low temperatures.

In our experiment, we use the strong 401-nm transition with a linewidth of 27.5 MHz for the Zeeman slower (ZS) and the narrow 583-nm transition with a linewidth of 190 kHz for the MOT. The 583-nm transition provides a low Doppler temperature of 4 µK and a low recoil temperature[2] of 170 nK due to the high mass of erbium. In general, a transition used for laser cooling needs to be optically closed, which means that no atoms decay to metastable states and thus, get dark to the cooling light. The branching ratio, which is the probability of a decay to a metastable state per cooling cycle, limits the atomic population reaching the desired temperature.

[1] $T_{\mathrm{Doppler}} = \frac{\hbar\Delta\nu}{4\pi k_B}$ [Foo05]

[2] The recoil temperature $T_{\mathrm{recoil}} = \frac{\hbar^2k^2}{m}$ is the fundamental limit for sub-Doppler cooling [Foo05].

Figure 1.1 shows that the 401-nm as well as the 583-nm transition are optically open. Decay can happen via electric dipole allowed transitions to several states with even parity and $J = 6, 7, 8$. According to Ref. [Ban05], the branching ratios can be estimated to about 10^{-4} for the 401-nm transition and about 2×10^{-8} for the 583-nm transition.
The branching ratio for the 401-nm transition suggests that operating a MOT on this line shows bad performance. However, the group around J.J McClelland has demonstrated a MOT with an atom number of more than 10^6 atoms using the 401-nm transition [Ber08]. They explain this result with a recycling mechanism, where the atoms decaying to metastable states stay in the vicinity of the MOT due to trapping by the quadrupole magnetic field, until they decay back to the ground state and are recaptured by the MOT. Trapping is only possible due to the high magnetic moment of $7\mu_B$ of erbium.

1.2 Isotopes

Er possesses six stable isotopes with masses ranging from 162 amu to 170 amu. Table 1.2 shows the abundance and the nuclear spin quantum number I for each of the isotopes.

Table 1.2: Abundance and spin quantum number for the different Er isotopes.

mass m (amu)	**abundance (%)**	**nuclear spin I**	**statistic**
162	0.1	0	boson
164	1.6	0	boson
166	33.5	0	boson
167	22.9	$\frac{7}{2}$	fermion
168	27.0	0	boson
170	14.9	0	boson

None of the bosonic isotopes shows hyperfine structure due to $I = 0$, whereas the fermionic isotope with $I = \frac{7}{2}$ has eight hyperfine states from $F = \frac{19}{2}$ to $F = \frac{5}{2}$. The abundance of ^{167}Er of more than 20% is exceptionally high compared to other fermionic alkaline atomics species such as ^{40}K [DeM99] and ^{6}Li [Sch01], which are often used for cold atoms experiments. The exact transition frequency between two atomic states depends slightly on the mass of the atom core and therefore, changes with different isotopes. This effect is called isotope shift [Foo05]. Figure 1.2 shows the inter-isotope shifts for three different transitions (401 nm, 583 nm, 841 nm) of the bosonic isotopes of erbium. These transition couple to states with $J = 7$ and therefore, ^{167}Er has 21 different transitions between the hyperfine states, which are not shown in this plot.

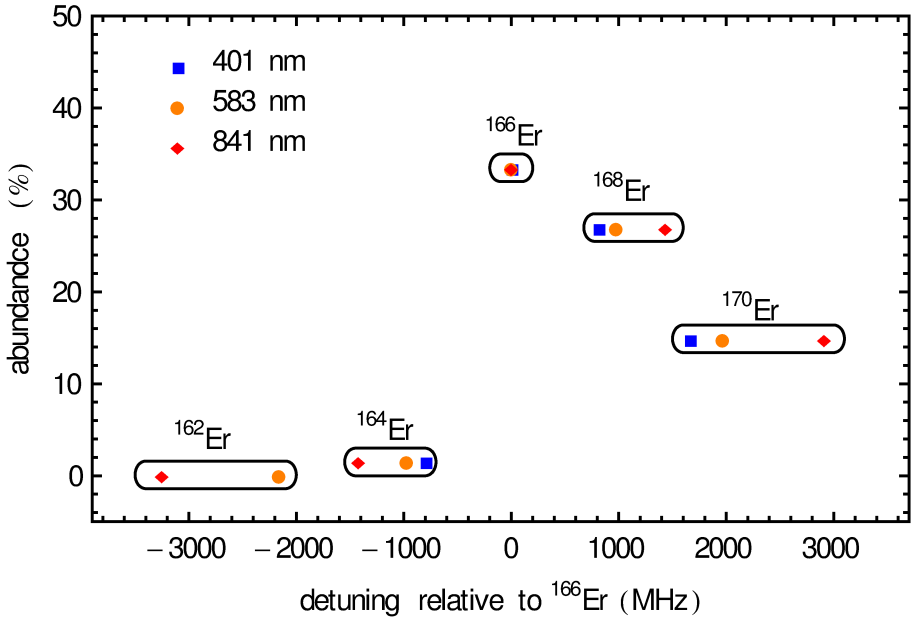

Figure 1.2: Isotope shift of three laser cooling transitions of Er vs. the natural abundance. The transitions for the fermionic isotope is not shown, as it involves 21 different transitions due to hyperfine splitting. Data taken from [Con10, Lip93, Jin90].

Typically, the isotope shift for Er is in the order of GHz, so one can reach the transition frequency of every isotope with a single laser system.

1.3 Magnetic properties

Compared to alkali atoms, Er has a high magnetic moment in its ground state. The absolute ground state has a total angular momentum quantum number of $J = 6$ and magnetic quantum number of $M_J = 6$. The magnetic moment μ is then calculated by

$$\mu = g_J M_J \mu_B, \tag{1.1}$$

where g_J is the Landé g-factor. For the Er ground state $g_J = 1.16$, which gives a magnetic moment of $6.98\,\mu_B$. The high magnetic moment has a huge impact on the quantum behavior due to the dipole-dipole interaction (DDI) energy. For polarized dipoles, the DDI reads as

$$U_{\mathrm{DD}} = \frac{\mu_0 \mu^2}{4\pi} \frac{1 - 3\cos^2(\theta)}{|\,\vec{r}\,|^3}. \tag{1.2}$$

Here, $\vec{r}$ is the relative coordinate between the two dipoles and θ is the angle between $\vec{r}$ and the dipole axis [Lah09]. Interesting properties of the DDI is its anisotropy and long-range character, which could introduce novel collisional behavior. For example, the prohibition of ultracold collisions between identical fermions could be lifted due to the anisotropy of the DDI [Bar08].

1.4 Narrow-line transition for magneto-optical trapping

In summary, the 583-nm laser used for magneto-optical trapping of Er has to fulfill the following specifications.

- The linewidth of the laser light has to be in the order of or below the linewidth $\Delta\nu$ of the 583-nm transition, which is 190 kHz, to get enough power into the transition during MOT operation.

- To get a large capture volume for our 3D-MOT, the laser beams are expanded to the diameter of the viewports of the MOT chamber, which is about 3 cm. For a good cooling performance, the beam intensity should be several times the saturation intensity of the transition; e.g. for the ytterbium MOT a intensity of $45 \times I_{\mathrm{sat}}$ is used [Yam08]. For the 583-nm transition the saturation intensity is $0.13\,\mathrm{mW/cm^2}$. For example, if we use $45 \times I_{\mathrm{sat}}$, a power of about 40 mW per beam is needed.
  In order to have enough power including losses from optical elements, the laser should provide an output power of several 100 mW.

- The laser-frequency has to be stable during the typical timescale of an experiment, before the laser drops out of the resonance. An acceptable change in frequency of one $\Delta\nu = 190$ kHz in one hour implies that the frequency drift of the laser has to be less than about 50 Hz/s.

- The isotope shift for the different Er isotopes has to be bridged and thus, the laser and the locking setup has to be capable of changing its working-frequency continuously over several GHz.

Chapter 2

Dye laser for MOT operation

As a laser source for MOT operation, we use a continuous-wave ring dye laser[1]. The laser emits light at a wavelength of 583 nm. The active medium of the dye laser is pumped by a 10 W solid-state laser[2] at 532 nm. Our dye laser, as provided by the manufacturer, is specified to an output power of about 1 W, a linewidth of around 1 MHz and a frequency-drift of 100 MHz/h. An output power of 1 W is sufficient to operate the MOT, but we need to narrow down the linewidth below 190 kHz, which is the linewidth of the 583-nm transition of Er. In addition, we need to stabilize the laser frequency to reduce the long-term drift below several kHz/h. This requirement is necessary to keep the laser light resonant to the 583-nm transition during the data acquisition time, which is typically several hours. Therefore, the laser has been modified and locked to an external ULE cavity; see Chap. 3. Here, we present the basic concepts of the operation principle of our dye laser and the modified locking scheme.

2.1 Dye-laser active medium

One of the important parts of a laser is the active medium or gain medium. External energy is used to create a population inversion in a metastable upper state of the active medium. The population inversion is needed to make the stimulated emission to be the dominating process.
In a dye laser, the active medium is a liquid, which consists of organic dye-molecules mixed with a solvent. These molecules have a complex energy level diagram with several bands composed of a large number of rovibrational states. Absorption and emission of light can occur between bands and additional relaxation processes occur between rovibrational states within the band. This gives a large tuning range of several tens of nanometers, which is one of the advantages of a dye laser over other laser sources like diode lasers. Another advantage is, that there are dyes for nearly every wavelength in the visible spectrum available; see Fig. 2.1. We use Rhodamine 6G dissolved in ethylene glycol, as it has the largest conversion efficiency at 583 nm and further, it has the advantage of not being toxic.

[1] Radiant Dyes CW ring dye laser
[2] Coherent Verdi V10

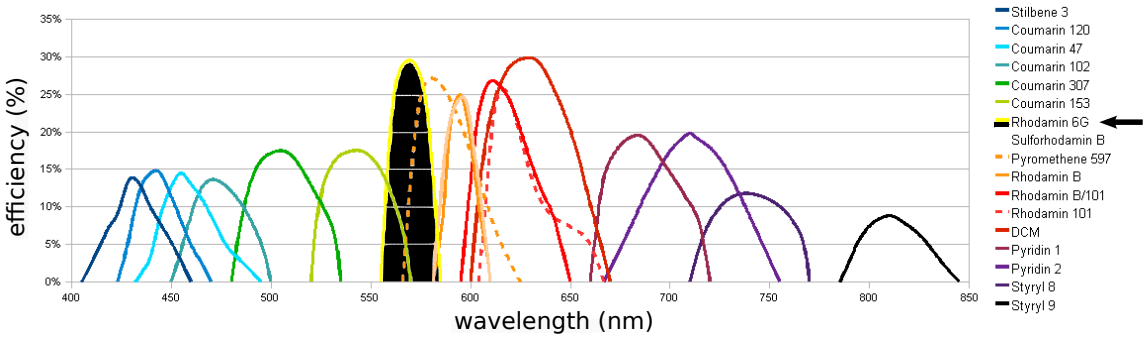

Figure 2.1: Tuning curves for different dyes in the visible spectrum. Dashed lines are for dyes that can only be used for pulsed lasers. The curve with the black filled background is the one for Rhodamine 6G, which is one of the interest for the present work. Graphic adapted from [Rad11].

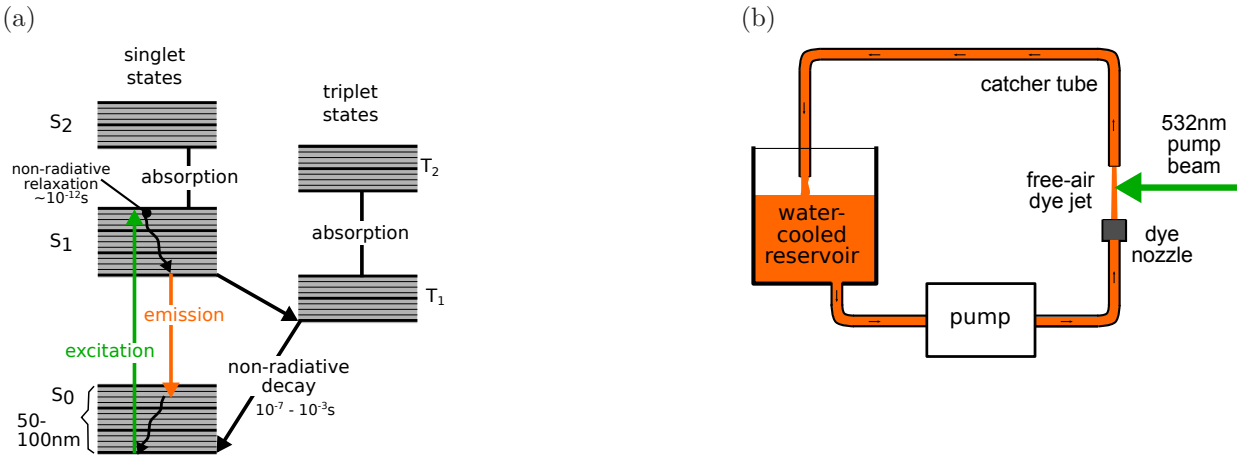

Figure 2.2: The active medium. (a) Level structure of a typical dye. The structure on which lasing occurs is a four-level system between the zeroth and first singlet state, which are very broad due to rotational and vibrational splitting. Vibrational states are indicated by thick lines, rotational states by thin lines. (b) Flow diagram of the dye circulator.

The lasing mechanism is based on absorption of pump light at 532 nm and emission of a broad spectrum of $560 - 585$ nm, from which one can choose the desired wavelength using optical filters; see Fig. 2.2(a). Dye molecules are pumped from the S_0 ground state into a higher rovibrational state of the excited singlet state S_1, followed by a non-radiative decay to the lowest rovibronic state of S_1. Lasing can occur on any transition going from the lowest S_1 state to the S_0 state. Loss processes are mainly absorption into the singlet state S_2 and triplet absorption between the states T_1 and T_2. Here, the problem is that the emission band, on which lasing occurs, and the absorption band may overlap. Triplet absorption is only possible, if there is a population in the T_1 state. The probability of $S_1 \Rightarrow T_1$ is low, while the transition rate of $T_1 \Rightarrow S_0$ can be as high as $10^3\,\mathrm{s}^{-1}$. As a result, the population can get

piled up fast in the triplet states. This would stop the laser emission after a time of about 0.1 ms. For this reason and due to heating of the dye liquid one has to constantly remove the dye solution from the interaction region with the pump laser, using a dye circulator[1]. The dye liquid is pumped with a pressure of about 7 bar into a nozzle, creating a homogeneous free-air dye jet; see Fig. 2.2(b). After interacting with the pump laser, the dye liquid is catched by a tube, in where the dye liquid flows back into a water-cooled reservoir.

2.2 Optical setup of the dye laser

Another important part of a laser is the laser cavity, which amplifies and frequency-selects the emission from the active medium. The simplest laser cavity is set up by two or more highly reflective mirrors acting as a resonator for light. The ideal geometrical alignment and the mode matching of the cavity mirrors sets the spatial mode of the output beam, which in our case is a Gaussian mode (also called TEM_{00} mode [Dem03]). For an overview on cavity behavior, see Sec. 3.1. Transmission through such a resonator is only possible if the optical length of the resonator is a multiple of the laser wavelength. This creates a comb-like transmission curve. In the case of a dye laser, the tuning curve of the active medium is very broad. Thus, the laser will run on multiple longitudinal modes (multiple frequencies) which are separated by the frequency distance between the transmission peaks of the laser cavity called free spectral range (FSR). To get a dye laser to operate on a single mode, additional optics are needed inside the laser cavity.

The optical setup for our dye laser is illustrated in Fig. 2.3. We use a ring cavity made of the four mirrors M1 to M4. The optical path in the cavity is about 1.5 m long. An astigmatism-correction rhomb is placed inside the cavity to increase the quality of the spatial mode of the laser beam. The rotate-able Brewster plate as well as the piezo-attached mirror M2 ("tweeter") are able to change the optical length of the ring cavity for fine adjustment and control of the output frequency. For selecting a single, longitudinal mode, a birefringent filter (BF), thin etalon (TNE) and thick etalon (TKE) are introduced into the beam path. An optical diode, which consists of a Faraday rotator followed by a thin $\lambda/2$ plate, is used for unidirectional operation. Without the optical diode the laser-beam would run in both directions around the ring cavity. This would lead to beam interference and spatial hole-burning in the active medium. The frequency of the laser is stabilized to a reference cavity, the photodiodes PD 1 and PD 2 are used to generate the error signal for feedback.

Frequency selective elements

The transmission curves for birefringent filter, thin etalon and thick etalon are schematically illustrated in Fig. 2.4(a). They are all periodic in frequency space. The periodicity is given by the free spectral range. Another important quantity is the width of one transmission peak. Often a small width is important to suppress the oscillation of all modes except one. If these elements are combined in the right way, which means a multiplication of the transmission curves, a single longitudinal mode can be selected from the ring cavity; see Fig. 2.4(b).

[1] Radiant Dyes RD1000CW dye circulator

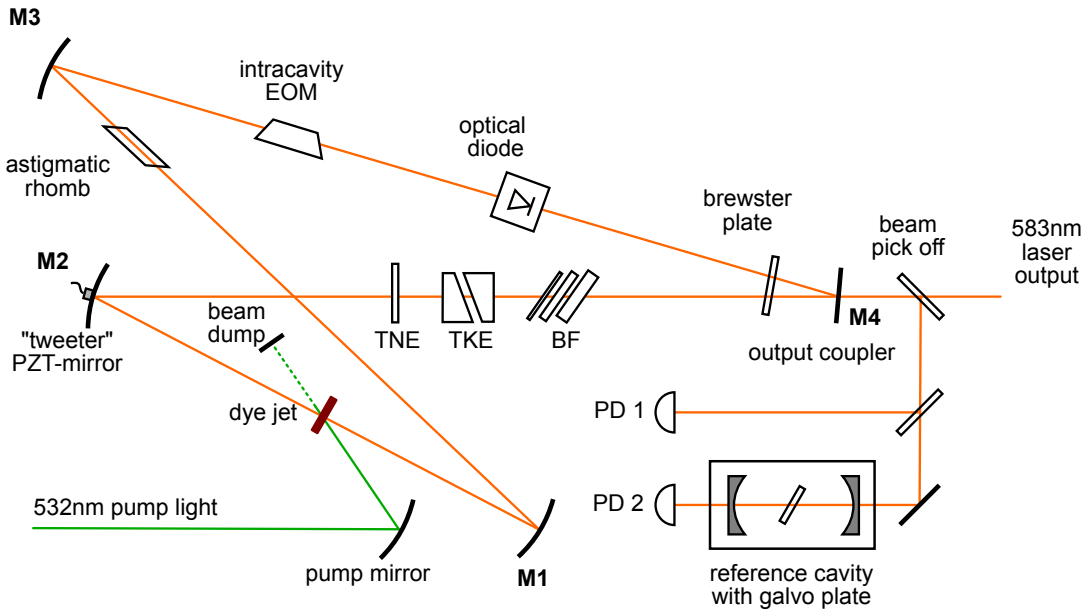

Figure 2.3: Optical setup of the dye laser. The dye jet is pumped by 532-nm light. The ring cavity is set up by the four mirrors M1 to M4. The elements inside the cavity are for single mode operation and to tune the laser frequency. The intracavity EOM has been added to the original configuration of the laser in order to narrow the linewidth of the laser below 1 MHz. Additionally, the reference cavity is drawn, which has been used to frequency-stabilize the laser in its original configuration.

Birefringent filter

Our three-stage birefringent filter is a combination of three birefringent plates in series. Three stages are used to amplify the filter effect. In the following, I explain the filter effect of one birefringent plate.

A birefringent plate has different refraction indices for different propagation directions inside the crystal. These directions are defined by the optical axis of the crystal, which is set by its structure. For a uniaxial crystal, this would be the direction along the speed of light is lowest or highest compared to the rest of the crystal. If polarized light is transmitted through a birefringent plate, the different velocities for ordinary and extraordinary rays result in a polarization rotation of

$$\Delta\Phi \approx \frac{2\pi d\Delta n}{\lambda \sin(\alpha)} \sin^2(\beta). \tag{2.1}$$

Here, λ is the optical wavelength, d is the distance covered by the ray inside the plate and Δn the difference of the refraction indices for extraordinary and ordinary ray [Bon86]. The angle β is between the optical axis of the birefringent crystal and the wave vector direction of the beam inside the crystal; see Fig. 2.5. If the plate is placed at Brewster's angle α into the beam path, a vertical polarized beam will have almost no losses in transmission, whereas other polarizations will exceed substantial losses. As the polarization rotation angle $\Delta\Phi$ depends on the wavelength, filtering is achieved. Tuning of the transmission peaks is done by turning the plate around the rotation axis as depicted in Fig. 2.5. This changes the angle

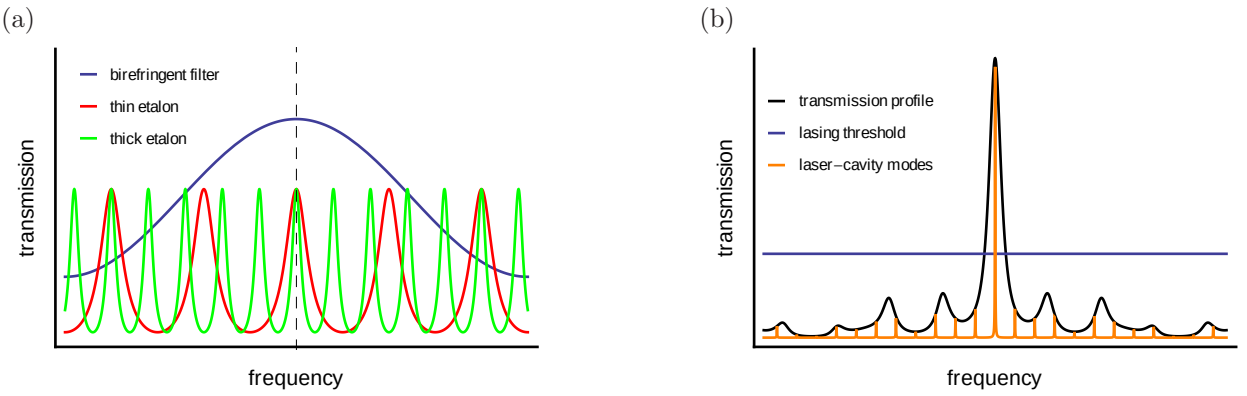

Figure 2.4: Transmission peaks of a dye laser resonator. (a) Schematic illustration of the transmission curves of birefringent filter, thick etalon and thin etalon. The curves are drawn out of scale to show the selection of a single frequency (dashed line). (b) Combined transmission curve. To get the combined transmission curve, the transmission curves of all the three elements have to be multiplied. Only one laser cavity mode is above lasing threshold due to the losses generated by the combined transmission curve.

β without changing the angle of incidence.
Using three birefringent plates with integer thickness ratios in series, the transmission peak width of the filter can be chosen independently of the FSR. Our three-stage filter has a FSR in the order of THz and has a broad transmission peak width compared to TNE and TKE.

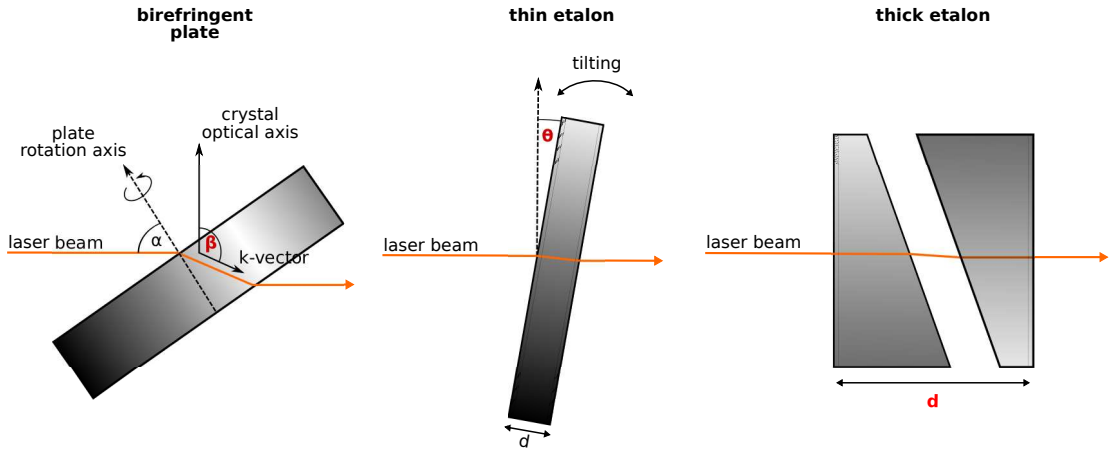

Figure 2.5: Schematics on the intracavity elements. The physical quantity, which is used to tune the transmission frequency, is the angle β for the birefringent plate (and filter), the angle θ for the thin etalon and the distance d for the thick etalon.

Thin and thick etalon

Thin and thick etalon are illustrated schematically in Fig. 2.5. These etalons work in exact the same way as the laser cavity or any other optical resonator; see Sec. 3.1. If the wavelength of the light matches the optical distance (nd) inside the plate, a standing wave builds up in

the optical element and the plate gets transmissive. The transmission peaks of an etalon are at wavelengths

$$\lambda_m = \frac{1}{m} 2nd\cos(\theta), \tag{2.2}$$

where m can be any integer number greater than zero and n is the refraction index of the glass. The angle of incidence is θ and d is the thickness of the plate. Tuning of the transmission curve is done in two ways. The thin etalon changes the angle of incidence θ by using a galvo motor, while the thick etalon, which is made up of two Littrow prisms, can change its distance d with a piezoelectric transducer (PZT) mounted to one of the prisms. The thin etalon has a FSR of about 200 GHz and is used for rough filtering in comparison to the thick etalon with a FSR of 10 GHz and narrower transmission peak width.

2.3 Dye-laser locking scheme

Thermal and mechanical noise introduce fluctuations in the length of the ring cavity. The frequency drift of an intracavity element results in a mode hop in the laser output, whereas length fluctuations of the ring cavity broadens the linewidth of the laser light. The birefringent filter and the thin etalon have a large enough transmission peak width to be manually tuned, but the distance of the thick etalon prisms and the length of the laser cavity have to be stabilized by feedback from a frequency reference. Generally speaking, a feedback-loop is used to keep constant a physical quantity, which in our case is the frequency of the laser light. For this purpose, the frequency of the light is compared to a stable frequency reference, which then gives the so-called error signal. The error signal is fed to a servo that transforms it in such a way that the frequency fluctuations are minimized, if the output of the servo is applied to an frequency-tuning element inside the laser cavity. In our setup we use analog Proportional-Integral-Derivative (PID) controllers. I will not go into detail explaining feedback theory and refer to literature [Tie99].
The locking scheme of the dye laser both before and after our modification is illustrated schematically in Fig. 2.6. We now discuss the different parts of the locking scheme in detail.

Thick etalon lock
As already mentioned, the distance of the two etalon prisms can be changed with a PZT. A small-amplitude sinusoidal voltage of 2 kHz frequency modulates the distance of the prisms, creating a slight amplitude modulation on the light at 2 kHz, which is detected by PD 1. The original 2 kHz signal is compared with the signal from PD 1 in a phase-sensitive detector (PSD). If the transmission maximum of the thick etalon is below the target frequency (transmission maxima of BF and TNE) in frequency space, the PZT-voltage increase leads to an increase of output power, resulting in a phase relation of 0° between the two signals in the PSD. Correspondingly, a transmission maximum above the desired wavelength ends up in a phase relation of 180°. Thus, for locking the TKE to the transmission maximum, the internal phase shifter of the PSD is set to 90°, creating an error signal which is integrated and fed back to the piezo.

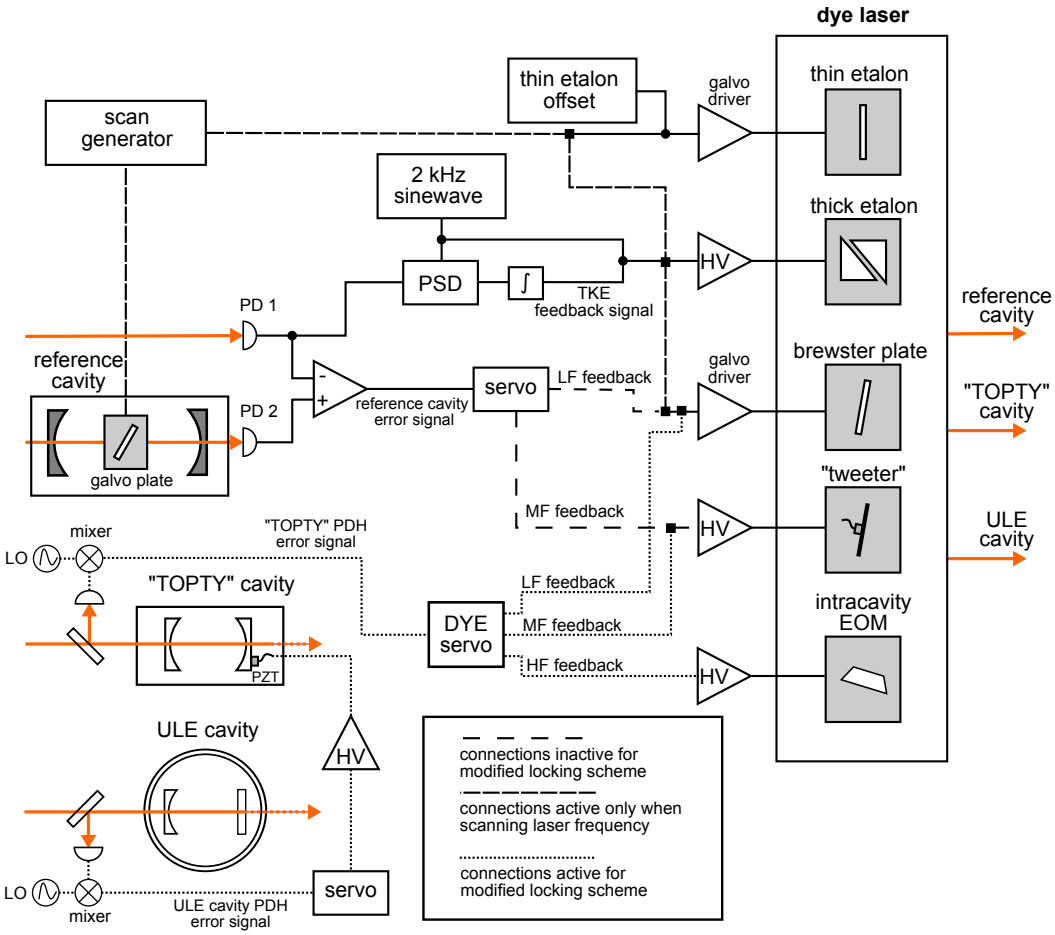

Figure 2.6: Feedback scheme of the dye laser. Both, the old locking setup and the modified locking setup are shown. The setup consists of 3 main parts. The thick etalon lock, which gets its error signal from PD 1, the original lock using the reference cavity and the modified lock, which gets the error signal from the "TOPTY" cavity and the ULE cavity. For narrowing the linewidth to lower values, the intracavity EOM has been added. Additionally, the mechanism to scan the laser frequency is shown.

Stabilization of the laser cavity length - linewidth reduction

Before the modification, the laser has been locked only to the reference cavity by a side of the fringe lock; see Fig. 2.6 and Fig. 2.7. In this configuration, the error signal is connected to a servo and split up into a mid frequency part (MF feedback) and a low frequency part (LF feedback). The low frequency component of the feedback signal is applied to the galvo driver of the Brewster plate, which has a frequency response of several 100 Hz and is able to correct the laser frequency by 15 GHz; see Tab. 2.1. The high frequency part is applied to the piezo of the "tweeter" mirror. This piezo has a frequency response of several kHz, and has a frequency correction range of 1 GHz. Here, the piezo is the element with the largest frequency response, which limits the servo bandwidth to several kHz and thus, is not fast enough to reduce the linewidth below 1 MHz. Further, the long-term drift of about 100 MHz/h of the reference cavity is not sufficient for operating the MOT.

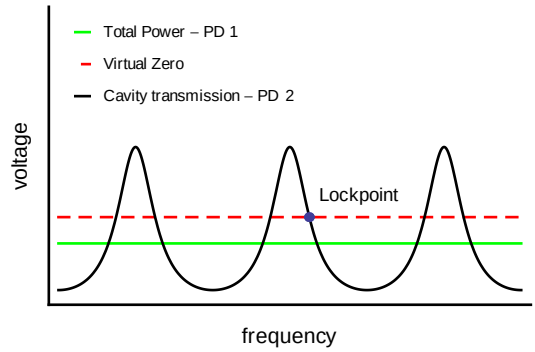

Figure 2.7: Error signal for the side-fringe locking technique. The reference cavity transmission is detected with PD 2. The error signal is generated by subtracting this signal by the signal on PD 1, which measures the total laser power. This creates a virtual zero at the side of a fringe at approximately ²/₃ below the maximum . The advantage of subtracting the total laser power is that the error signal gets insensitive to intensity fluctuations.

Therefore, we changed the locking scheme. To cancel out the faster frequency fluctuations, an intracavity electro-optical modulator[3] (EOM) with a frequency response up to 100 MHz, is introduced into the laser cavity. This EOM has a half-wave voltage of 1000 V. In combination with a laser cavity FSR of about 150 MHz this results in a frequency correction range of 75 kHz/V. In the new feedback scheme, the laser is pre-locked to a scanning Fabry-Perot cavity[4] ("TOPTY") by using the Pound-Drever-Hall locking technique; see Sec. 4.2. The PDH error signal from the "TOPTY" cavity is fed to the DYE servo, which splits up the feedback signal into a low frequency part (LF feedback), a mid frequency part (MF feedback) and a high frequency part (HF feedback). The parts are applied to the galvo driver of the Brewster plate, the "tweeter" piezo and the electrodes of the EOM, respectively. The electronic circuit for the DYE servo is found in App. B.5. For the feedback onto the EOM, a home-made high-voltage (HV) amplifier is used. This amplifier has a 3 dB bandwidth of about 800 kHz and a large-signal gain of about 25.

Table 2.1: Properties of the three elements which tune the laser frequency. The correction range is the maximum frequency change an element is able to correct.

element	frequency response	correction range
Brewster plate	several 100 Hz	15 GHz
"tweeter" piezo	several kHz	1 GHz
intracavity EOM	100 MHz	75 kHz/V

The "TOPTY" cavity itself is not stable for a long term. For this purpose, I built the ULE cavity, which has a long-term stability in the order of Hz/s; see Chap. 3. The error

[3] Linos PM25
[4] Toptica FPI-100-0500-1

signal from the ULE cavity is also generated with the PDH locking technique. This error signal is applied to a simple PID controller followed by an HV amplifier and fed to the piezo controlling the length of the "TOPTY" cavity. In this way, the long-term stability of the ULE cavity is transferred to the "TOPTY" cavity and the frequency of the laser light.

Scanning of the laser frequency

The scan generator changes the laser frequency by scanning the Brewster plate inside the reference cavity. By scanning slowly and feeding the scanning voltage forward to most of the intracavity elements, the laser stays locked during the process. A scanning range of 30 GHz is achieved.

Chapter 3

ULE cavity

In ultracold atom experiments, sophisticated lasers systems are used, for instance to trap and cool atomic clouds. Often these kind of experimental techniques require a high frequency stability of the lasers. Therefore, they have to be stabilized using frequency references.
A typical stabilization scheme is to lock the laser to an atomic reference for long-term stability and to stabilize it to a mechanically stable cavity for suppression of frequency fluctuations on short timescale. Such a scheme is not feasible in cases where atomic references are not available at the desired wavelength or it is too involved to implement. In addition, for narrow-line atomic transitions, with linewidths below several kHz, weak absorption and broadening effects in atomic references may be a limiting factor.
Since we want to address narrow-line transitions in our experiment, I have built an ultra low expansion (ULE) cavity, serving as a long- and short-term frequency reference. In the next Sections, the theoretical description of our cavity is discussed, followed by a description of the cavity design and the vacuum chamber enclosing the cavity.

3.1 Theoretical description

We here consider a lossless cavity consisting of two identical plane mirrors. The steady-state solution of cavity modes is known in literature [Dem05] and I here briefly summarize the main features of a cavity.
An overview of the working principle of the cavity is illustrated in Fig. 3.1. In deriving the steady state solution of the cavity-problem, it is sufficient to describe the incident light by a monochromatic wave $E_{\text{in}} = E_0 e^{i\omega t}$. The light is sent through two cavity mirrors at distance L, having reflection coefficient r and transmission coefficient t. In the case of negligible absorption processes in the mirrors, the transmission and reflection coefficients are connected by the following simple relation

$$r^2 + t^2 = 1. \tag{3.1}$$

All the partially reflected waves have to be summed up, to get an expression for the reflected light field. Each reflection shifts the phase of the light field by π. In addition one has to take the phase shift Φ into account, which is accumulated due to propagation of the wave

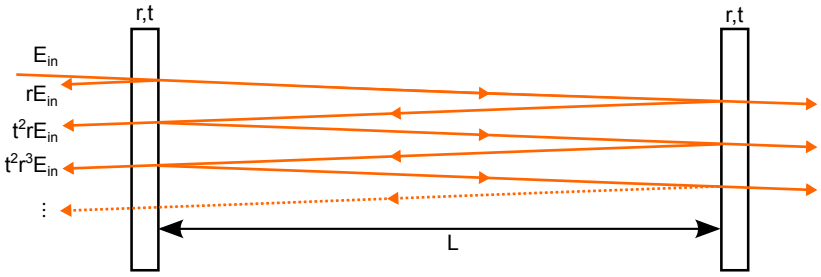

Figure 3.1: Scheme of a symmetric lossless cavity. The cavity consists of two mirrors with reflection coefficient r and transmission coefficient t. The transmitted and reflected light field are generated by multi-beam interference. For a better illustration, the angle of the incident beam is drawn $\neq 90\,^\circ$.

during every round-trip,

$$\Phi = \omega \frac{2L}{c}, \tag{3.2}$$

where ω is the frequency of the light field and c the speed of light in vacuum. The total reflected light field E_{ref} is then given in the limit of infinite partially reflected waves.

$$\begin{aligned} E_{\text{ref}} &= E_{\text{in}} \left(-r + t^2 r e^{i\Phi} + t^2 r^3 e^{i2\phi} + ...\right) \\ &= E_{\text{in}} r \frac{e^{i\Phi} - 1}{1 - r^2 e^{i\Phi}}. \end{aligned} \tag{3.3}$$

From expression (3.3), the total reflected light intensity I_r is derived by taking the absolute square. We get the transmitted intensity I_t with the same approach, by adding up the transmitted partial waves and taking the absolute square. Finally, one obtains

$$I_r = I_{\text{in}} \frac{4R \sin^2(\Phi/2)}{T^2 + 4R \sin^2(\Phi/2)}, \tag{3.4}$$

$$I_t = I_{\text{in}} \frac{T^2}{T^2 + 4R \sin^2(\Phi/2)}, \tag{3.5}$$

where $I_{\text{in}}^2 = \frac{c\epsilon_0}{2} E_{\text{in}}^2$, $R = r^2$ and $T = t^2$ are the ingoing intensity, the reflectance and transmission of the mirrors, respectively. The transmission function $I_t(\omega)$ has two main properties as illustrated in Fig. 3.2. First, the function is periodic. The periodicity is given by the frequency distance between two adjacent transmission peaks and is called free spectral range

$$\text{FSR} = \frac{c}{2L}. \tag{3.6}$$

For instance, a cavity length of $L = 15\,\text{cm}$, results in a FSR of about 1 GHz.
The second important parameter is the full width at half maximum FWHM or also called linewidth $\Delta\nu$ of the transmission peaks. We are only interested in cases, where the mirrors are highly reflective ($R > 0.5$) and thus, the transmission peaks are very sharp. The linewidth is an important parameter, because it is directly related to performance of the Pound-Drever-Hall lock; see Sec. 4.2. A simple expression for the FWHM of the cavity is found by defining

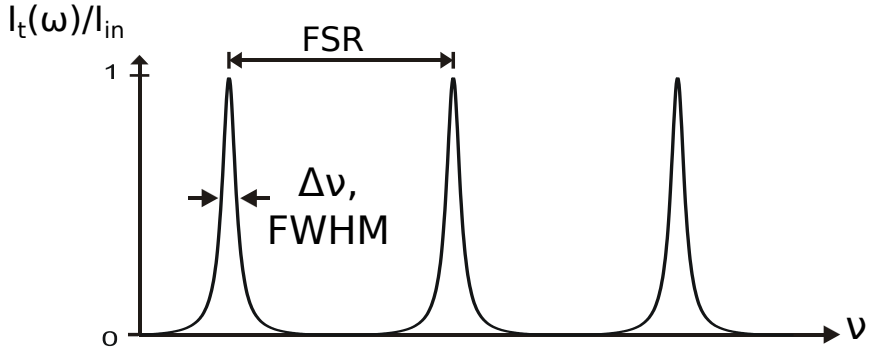

Figure 3.2: Transmission of a cavity as a function of the frequency. The periodicity of the transmission function is given by the FSR. The measure for the quality of the resonator, the FWHM linewidth $\Delta\nu$ of a cavity mode is marked.

another parameter, the finesse $\mathcal{F}$. The finesse is a measure for the reflectance of the mirrors, the equation

$$\mathcal{F} \approx \frac{\pi\sqrt{R}}{1-R} \tag{3.7}$$

is used for $R > 0.5$. Examples for various finesses specified for our cavity can be found in Tab. 3.1. With the finesse defined, a simple expression for the linewidth of the cavity can be found,

$$\Delta\nu = \frac{\mathrm{FSR}}{\mathcal{F}}. \tag{3.8}$$

The linewidth of the cavity, can be measured indirectly via the average photon storage time τ. This is the characteristic time for the exponential decay of the transmitted light intensity, when the light incident on the cavity is suddenly switched off.

$$\tau = \frac{1}{2\pi\Delta\nu}. \tag{3.9}$$

In our derivation of the cavity transmission function, the spatial profile of the intensity distribution has not be taken into account. This profile can be described by a superposition of so called Hermite functions called $\mathrm{TEM}_{\mathrm{nm}}$ modes [Dem03], where n and m are positive integers. Depending on the geometry of the cavity, length and mirror curvatures, the TEM modes have different transmission frequencies. The locking performance degrades, if other TEM modes lie close to the TEM_{00} modes in frequency space.
We use a cavity configuration, where one mirror is plane and one mirror has curvature ρ. The transmission frequencies of the different TEM_{nm} modes in the resonator are then given by

$$\delta\nu = (n+m+1)\frac{\mathrm{FSR}}{\pi\cos\left(\sqrt{1-\frac{L}{\rho}}\right)}. \tag{3.10}$$

For example, with a cavity length of 15 cm and a mirror curvature of $\rho = 400$ mm, evaluation of Eq. (3.10) gives a frequency distance of 210 MHz between adjacent cavity modes. In this case, only cavity modes with $n + m > 4$ could lie near the TEM_{00} mode. These modes

can easily be suppressed by a good cavity coupling. For a good coupling the laser beam propagation axis has to match exactly the cavity axis. Further the radius of curvature of the phase front has to be matched with the radius of curvature of the mirrors.
This is achieved by focusing a laser beam, which already has a good Gaussian shape, into the cavity. For our cavity geometry, the mode matching condition corresponds to a beam waist of

$$w = \sqrt{\left(\frac{L\lambda}{\pi}\sqrt{\frac{r-L}{L}}\right)}. \tag{3.11}$$

Here, λ is the wavelength of the light that is resonant to the cavity.

3.2 Cavity design considerations

Our cavity mirrors have been designed for several wavelengths of interest for the erbium project. The full chart of the reflectance of the mirrors depending on the wavelength is shown in Fig. 3.3. The cavity has different finesses for the different wavelengths optimized for a good locking performance, and because of Eq. (3.11) also the mode matching condition is wavelength dependent. Specifications of these quantities can be found in Tab. 3.1.

Within the scope of this thesis, we want to lock only the 583-nm light to the cavity. The locking setup has to be capable of changing immediately the lock between different isotopes. For tuning the transmission frequency we use two acousto optical modulators with limited tuning capabilities. Therefore, I chose the cavity to have a length of 15 cm, which gives a free spectral range of 1 GHz, which roughly matches the isotope shift of the erbium bosonic isotopes.

par.	value
L	15 cm
FSR	1 GHz
$\delta\nu$	210 MHz
ρ	400 mm

λ (nm)	R (%)	$\mathcal{F}$	$\Delta\nu$ (kHz)	(w µm)
583 (spec.)	99.91	3500	286	190
583 (meas.)	99.83	1865	536	190
631	99.95	6500	154	200
841	99.96	8000	125	230

Table 3.1: (left): Cavity parameters resulting from the geometry. For evaluation of $\delta\nu$ Eq. (3.10) is used. The FSR has been measured; see Sec. 5.1. (right): Specifications for different wavelengths resonant to erbium. For calculation of the finesse $\mathcal{F}$, the linewidth $\Delta\nu$ and the mode-matching waist w, Equations (3.8, 3.11) are used. The finesse at 583 nm has a value of 1865 (see Sec. 5.2 for details).

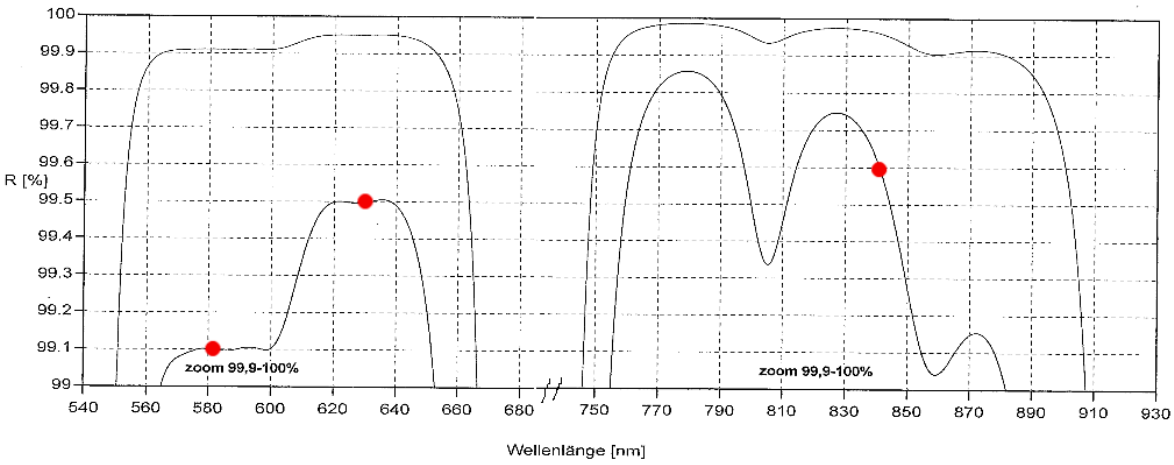

Figure 3.3: Chart of the reflectivity versus wavelength for our mirror coating. Below the upper reflectivity curve a zoom into the region between 99.90 and 100 % is shown. The mirrors are highly reflective in a range of $560 - 650\,\text{nm}$ and $750 - 890\,\text{nm}$. The red points mark the wavelength of the Er transitions.

Frequency stability requirements

Absolute frequency stability of a cavity is directly related to the stability of its length and the fluctuations of the refraction index of the medium between the cavity mirrors. Therefore, one has to minimize temperature changes that influence the length of the spacer as well as changes in the refraction index, pressure changes and vibrations. The narrowest transition in Er lockable to our cavity is the 841-nm transition, with a linewidth of 8 kHz.
This means, that the cavity resonance should not drift by more than 8 kHz in a typical experimental timescale of several hours. The frequency change Δf of the cavity is directly connected to the changes of the optical length nL of the cavity. Therefore, the following criterion has to be fulfilled.

$$\begin{aligned} \Delta f &< 8\,\text{kHz} \rightarrow \\ \frac{\Delta f}{f} &= \frac{\Delta L}{L} + \frac{\Delta n}{n} < O(10^{-11}). \end{aligned} \tag{3.12}$$

Here, Δn is the change in the refraction index of the air between the cavity mirrors.
Using the equation for an ideal gas, relative changes in the refraction index can be related to the temperature T and to the pressure p of the gas via the Clausius-Mosotti equation [Jac06], which gives the relation

$$\begin{aligned} (n-1) &\propto \frac{p}{T} \Rightarrow \\ \frac{\Delta n}{n} &= \frac{n-1}{n}\sqrt{\left(\frac{\Delta p}{p}\right)^2 + \left(\frac{\Delta T}{T}\right)^2}. \end{aligned} \tag{3.13}$$

At standard lab conditions, the refraction index is about $(1 + 10^{-4})$. This means that the temperature T and the pressure p of a gas should have relative fluctuations below 10^{-7}.

By placing the cavity in a vacuum chamber (see Fig. 3.4), and pumping the chamber off to a pressure of about 5×10^{-8} mbar, pressure fluctuations and temperature fluctuations are suppressed to an acceptable amount.
Further, the length of the cavity has to be insensitive to temperature fluctuations. This is achieved by optically contacting the mirrors to a spacer made of ultra low expansion glass[1] (ULE). The optical contacting is a glass bonding technique. Two highly cleaned glass surfaces with a flatness in the order of tens of nanometer are connected by overlapping and putting small pressure on them. The two surfaces stick together due to the Van der Vaals force. We did the optically contacting by ourselves in a clean room; see App. A.2. The material ULE is suited best for applications where low thermal drifts are required, because it has a low coefficient of thermal expansion (CTE) in the order of 10^{-8}/K around room temperature. A characteristic feature of ULE is that it is designed such, that the CTE has a zero-crossing near room temperature. This temperature is called zero-expansion temperature T_C, which is specific of every cavity assembly and has to be experimentally determined. If the cavity temperature is stabilized near T_C, only small frequency drifts of the cavity of around 0.1 Hz/s remain due to the degeneration of the crystal structure of the ULE [Leg10].
Another noise source that contributes to length changes of the cavity is mechanical deformations of the spacer due to vibrations. Especially, vibrations in the frequency range of $1 - 10$ Hz, which are present in every building, can not be damped effectively by an optical table. An estimation for our cavity can be made using [Che06] and [CVI09]. For our spacer geometry (see Fig. 3.5), we estimate the vibrational sensitivity to be about 200 kHz/m s^{-2} along the vertical axis. Further, we estimate the maximum acceleration acting on our cavity vertically to about 3 mm/s^2. This estimation gives a frequency change of 600 Hz due to vibrations, which is not a limiting factor for us.

3.3 Mechanical setup

Figure 3.4 shows a 3D drawing of the complete assembly. A cylindrical vacuum chamber with a diameter of 250 mm and a height of about 220 mm houses the cavity. The chamber has two CF40[2] viewports[3] for optical access. An additional flange is used to connect a 25 pin Sub-D electric feedthrough, which is needed to supply temperature sensors and Peltier elements to cool the inside of the vacuum chamber. To evacuate and pre-evacuate the chamber, an ion-getter pump and an edge-valve to connect a turbopump are mounted, respectively. To protect the spacer, the vacuum chamber is not baked. The ion-getter pump has a pumping speed of 20 L/s, we reached a pressure of 5×10^{-8} mbar several weeks after closing the vacuum chamber. This pressure is low enough for our purposes and also guarantees a long lifetime of the ion pump, as it is continuously powered. The vacuum chamber is mounted on an aluminum baseplate to guarantee a good heat release from the bottom CF250 flange of the

[1] ULE, Corning Code 7972

[2] CF (ConFlat) flanges have knife-edges cutting into a gasket made of copper (or other soft metals), when two flanges are pressed together. This kind of sealing is used for ultra high vacuum (UHV). For example, CF40 (more precisely CF DN40) means that inner diameter of the flange is 40 mm.

[3] VACOM - silica viewports with a broadband anti-reflection coating at 560-780 nm.

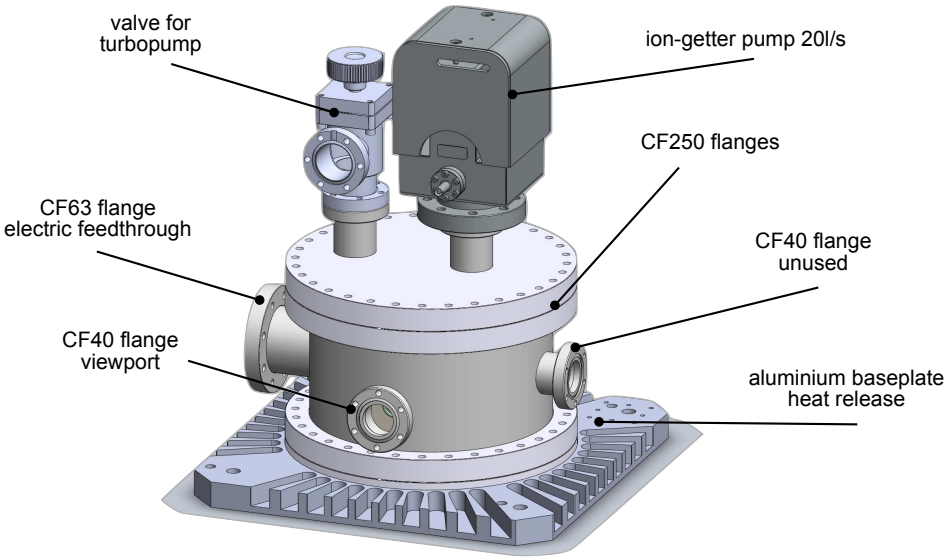

Figure 3.4: 3D drawing of the vacuum chamber. All the parts for the vacuum chamber are made of steel and connected by CF flanges. Pumping is done by a 20 L/s ion-getter pump after pre-pumping the chamber with a turbopump connected to the edge-valve. The CF63 flange is connected to a 25 pin Sub-D electric feedthrough to connect Peltier elements and temperature sensors. The steel CF250 flange on the bottom is used as a heat sink for the Peltier units. For heat release from this flange and for mounting the chamber onto the optical table, the flange is screwed to a baseplate made of aluminum. For optical access to the cavity two CF40 viewports are used (one is not seen).

chamber the Peltiers are glued to.
Figure 3.5 shows a sectional view through the vacuum chamber. Our cylindrical cavity sits on a V-shaped block, where it is supported on four small Viton[4] cylinders. These cylinders are glued onto the V-block with vacuum epoxy[5]. Along the cavity axis, these suspension points are at the so called Airy distance $AD = 0.578L$. If the cavity is suspended at these points, the end-facets of the spacer stay parallel during cavity deformation and at the same time the vibrational sensitivity is minimized for this kind of 4-point suspension from below, to about 200 kHz/m s^{-2}. The central bore drilled through the center of the spacer guarantees passage for the laser beam. For evacuation of the inside another small bore is drilled vertically. For a good temperature isolation, the cavity is surrounded by two cuboidal boxes made of aluminum, the inner and the outer shield. The inner shield is a passive heat shield working as a temperature low-pass filter, and is separated from the outer heat shield by five Teflon[6] spacers. The isolation between the shields is very high, I measured a time constant of about 21 hours, and therefore, it takes several days until the temperature of the inner shield has thermalized completely; see Sec. 5.3. The temperature of the outer

[4]Viton is similar to rubber and has low outgassing rate in vacuum.
[5]EpoTek - 353ND optical adhesive
[6]Teflon has a low thermal conductivity and low outgassing rate in vacuum.

heat shield is controlled by four Peltier elements, which support the outer shield. The cold sides of the Peltier elements are glued with silver loaded epoxy[7] onto the bottom plate of the outer shield, whereas the hot sides are glued to the bottom CF250 flange of the vacuum chamber. Heat from this flange is released by the aluminum baseplate mounted to it. For the temperature regulation and monitoring of the temperature inside the chamber at different places, we use six temperature sensors glued with vacuum epoxy at different positions inside the chamber; see App. A.2.
Further, two AR-coated glass plates prevent the thermal radiation to reach the cavity through the bores inside the walls of the heat shields along the cavity axis. These glass plates are glued onto the outer shield slightly tilted, about 5 °, from the vertical axis to prevent interference effects. Due to the same reason, also the AR-coated viewports have a tilt from the vertical axis. Inside the cavity, Capton-coated wires are used, which are all soldered onto a 25 pin in vacuum connector.

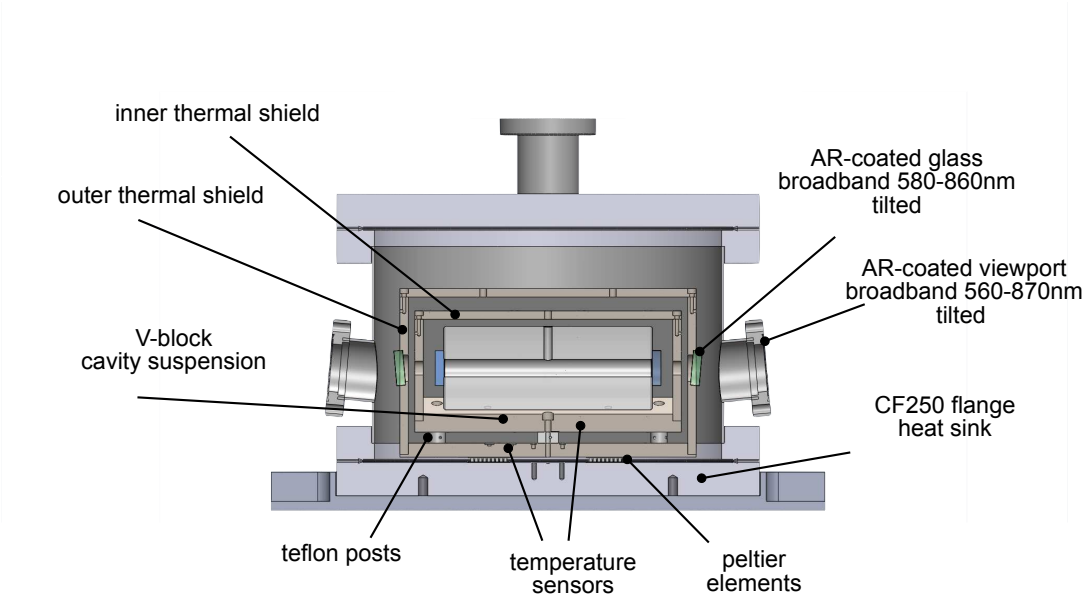

Figure 3.5: Sectional view through the center of the cavity. The cavity is suspended by four small Viton cylinders glued onto the V-block (two of the cylinders are seen). The cavity is surround by two thermal shields, which are separated by five Teflon spacers. The outer shield is temperature controlled by four Peltier elements. For further shielding of thermal radiation, two tilted AR-coated glass plates are glued onto the outer shield. The viewports for optical access are also tilted from the vertical axis by a small angle.

[7]RS-Components - Silver loaded epoxy

3.4 Temperature control

We cool the cavity down to the measured zero-expansion temperature of −5.65 °C; see Sec. 5.3. The cooling is done by using four Peltier elements[8] placed inside the vacuum chamber. For keeping the cavity at this temperature, the Peltier elements need a total electric power of about 13 W. The Peltier coolers control the temperature of the outer shield, which surrounds the inner heat shield for suppression of fast temperature fluctuations.
For the measurement of the temperature, three negative temperature coefficient (NTC) sensors with a nominal resistance of 10 kΩ and three PT1000 (1000Ω) temperature sensors are used. The schematics of the complete setup to control and monitor the temperature of the cavity is depicted in Fig. 3.6. The electronics for the temperature control loop are placed

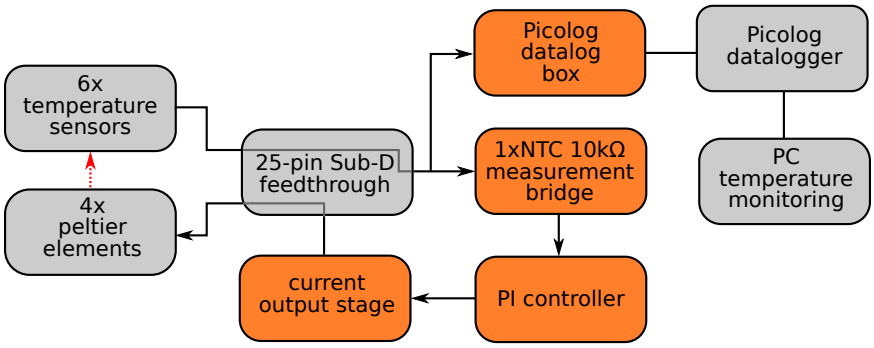

Figure 3.6: Scheme for controlling and logging the temperature of the cavity. The temperature control loop is split from the logging setup after the feedthrough. The cable-pair carrying the signal of one NTC is connected to the measurement bridge, whereas the other cables that are soldiered to the other five sensors are connected to the Picolog datalog box. The orange boxes represent electronic boxes made by myself.

inside three different boxes. The measurement bridge creating the error signal, the PI controller generating the feedback signal and the current output stage, which amplifies the low power feedback signal. The electronic circuits for these three boxes are found in App. B. The resistances of the four of the other five temperature sensors are measured inside the Picolog datalog box by four voltage dividers, which are soldered to a pre-build PCB board[9]. The electronic circuit for this box can also be found in App. B. The voltage signals proportional to the resistance of the sensors are then transformed into digital signals inside the Picolog data logger[10]. The Picolog data logger is connected to a computer, where the digital signals are converted into temperature and monitored[11]; see App. A.3.

[8] Laird Technologies - ThermaTEC HT4,7,F2,3030
[9] This pre-build PCB board is shipped together with the Pico data logger.
[10] Picolog Datalogger ADC-24bit
[11] Picolog Recorder

Chapter 4

Experimental setup

The preparation of the MOT light includes control over the frequency, the linewidth and the intensity of the laser light. For frequency and linewidth control, the dye laser is stabilized to a scanning Fabry-Perot cavity and to a ULE cavity via the Pound-Drever-Hall (PDH) method.
In the first Section of this Chapter, I will describe the optical setup for the light at 583 nm. In the second Section, I will present details about our realization of the PDH setup.

4.1 Optical setup

Figure 4.1 gives a global overview of the optical setup used to generate the magneto-optical cooling light. The setup is divided into several main sections, which serve to different specific scopes. In general, we prepare the MOT light on the optical table and we transport the light via optical fibers to the different sections, which are mainly placed on single breadboards (round-edged boxes). The sections include for instance the optical setups for locking, for spectroscopy, for wavelength detection (fiber to the wavemeter), and for distributing the light into the different MOT beams.
Here, we list and briefly describe the main sections of the full optical setup:

Wavelength detection
To monitor the absolute frequency of the laser light with an accuracy of several MHz, we send a part of the light to a wavemeter. The use of a wavemeter significantly facilitates the locking of the laser to the correct ULE cavity mode and the adjustment of the dye laser wavelength.

Pre-lock section
In the pre-lock section, we prepare the light with a PDH locking setup and send it to a mid-finesse cavity for narrowing the linewidth of the dye laser.

MOT light preparation section
Here, we use an acousto-optical modulator to stabilize the intensity of the MOT light on the MOT distribution board and to fine-tune the frequency of the light for the MOT.

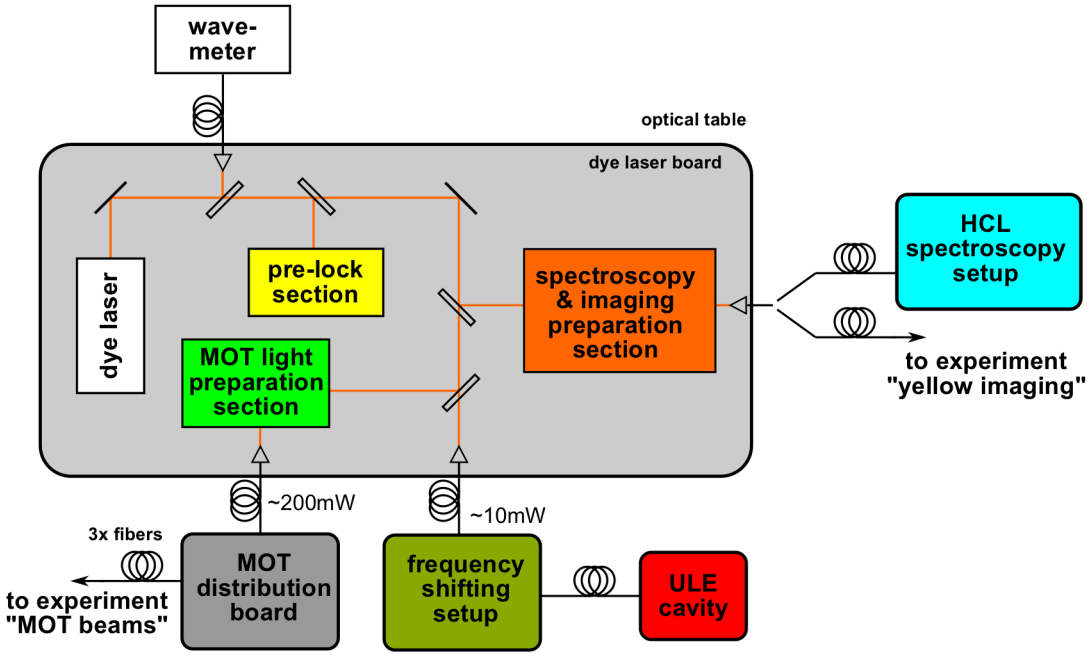

Figure 4.1: General concept of the optical setup for the 583- nm light. The setup is divided into several parts marked by colored boxes. Round-edged boxes mark parts of the optical setup, which are placed on their own breadboard. The different breadboards are connected via fibers.

MOT distribution board

For generating the beams for the MOT, we split the light into three paths. The light is then coupled into three fibers, which are connected to fiber couplers on the main experimental table. We use a standard six-beam 3D-MOT with retro-reflected beams.

Spectroscopy and imaging preparation section

We use an AOM to shift the frequency of the light to the desired erbium atomic transition. Using this light, we perform spectroscopic measurements either by using a hollow cathode lamp (HCL) or by imaging the atoms in the MOT chamber, which to referred as “yellow imaging”.

HCL spectroscopy setup

We perform modulation transfer spectroscopy on erbium in a hollow cathode lamp. The spectroscopic measurements are used to optimize the locking setup.

Frequency shifting setup

We use the frequency shifting setup to tune the frequency of the laser light to an arbitrary value while the laser is locked to the ULE cavity. For this, we use two AOMs to shift the laser frequency by amounts smaller than the FSR of the ULE cavity (about 1 GHz).

ULE cavity setup
This setup consists of the ULE cavity, the optics for coupling to the cavity and for PDH-locking.

4.1.1 Optical setup on the dye laser board

Figure 4.2 shows the optical setup on the dye laser board. About 1 mW of light emitted

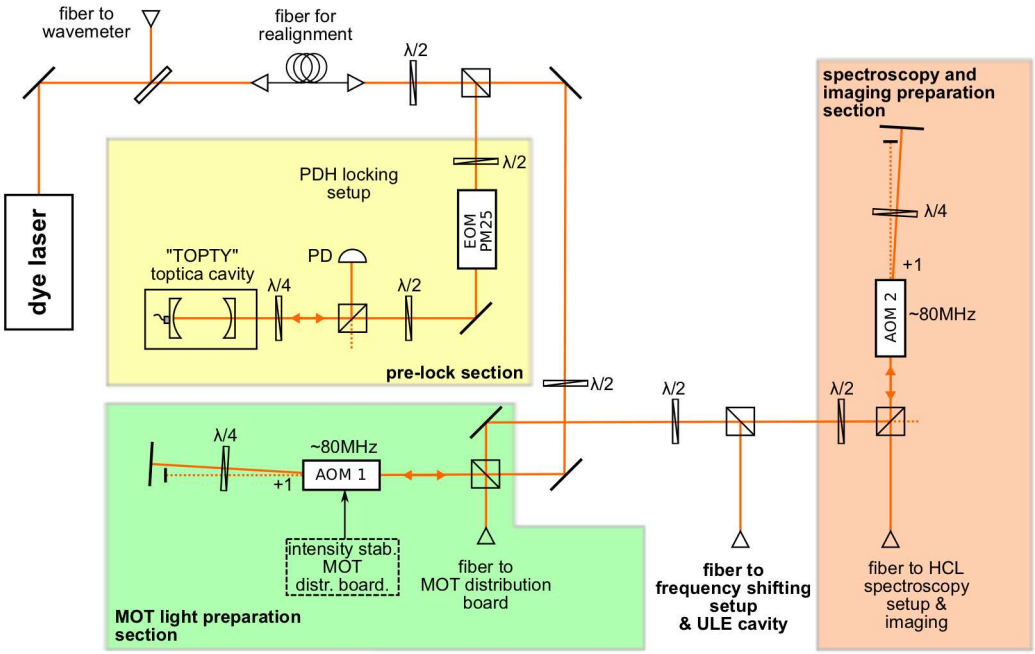

Figure 4.2: Scheme of the optical setup for the 583-nm light on the dye laser board. The setup is divided into the pre-lock, MOT light preparation and spectroscopy and imaging preparation section. For simplicity, lenses are not shown.

from the dye laser is coupled to a single-mode fiber[1] which is connected to a wavemeter[2] for monitoring the frequency of the light. Most of the laser-field intensity is coupled to a short fiber[3]. This fiber is used for alignment purposes since the angle and position of the beam emitted from the laser changes if the internal laser cavity is realigned. After this short fiber, the light is split into several paths by using polarizing beamsplitters (PBS) and half-wave ($\lambda/2$) plates.

Pre-lock section
In the pre-lock section, the light is sent to a Fabry-Perot cavity[4] ("TOPTY"), which has

[1] Thorlabs HP-460
[2] HighFinesse WS/7
[3] Thorlabs PM-460
[4] Toptica FPI-100-0500-1

a finesse of about 1000 at 583 nm. One of the cavity mirrors is attached to a piezoelectric actuator (PZT), which is capable to scan the cavity over more than one free spectral range of 1.5 GHz. This cavity is used for narrowing the linewidth of the dye laser. The error signal is generated with the Pound-Drever-Hall locking technique[5]; see Sec. 4.2.

MOT light preparation section
To prepare the light for the MOT, the intensity is stabilized after the fiber connected to the MOT distribution board. For this purpose, we use the acousto-optical modulator 1 (AOM 1)[6]. The feedback signal for the intensity stabilization is created by a photodiode placed on the MOT distribution board and a proportional-integral-derivative (PID) controller. The feedback signal is applied to an analog attenuator inside the RF-amplifier which amplifies the signal driving the AOM. Further, we use the AOM to fine-tune the frequency of the light, e.g. for optimizations and frequency scans in the range of several MHz. The AOM has a center-frequency of 80 MHz and is set up in double-pass configuration. Currently we use the $+1^{\text{st}}$ order of the light.

Spectroscopy and imaging section
In the spectroscopy and imaging preparation section, we shift the frequency of the light to the desired value needed for spectroscopy or imaging of erbium atoms. For this, we use AOM 2[6] in double-pass configuration.

4.1.2 Frequency-shifting setup

To tune the dye laser to any desired frequency while it is locked to the ULE cavity, we put optical elements into the beam path before the cavity. For this, we use a combination of two AOMs[7]. We use the AOMs either in single-pass or double-pass configuration [Don05]. As shown in Fig. 4.3, the double-pass configuration includes a lens with f=75 mm to preserve the alignment, a quarter-wave plate and a PBS to separate the incoming from the reflected light. Further, AOM S1 is used to stabilize the light intensity for the ULE cavity; see Fig. 4.6. After passing the two AOMs, the light is coupled to a fiber[8] connected to the ULE cavity breadboard.

To get an estimation of the frequency tuning range of the two AOMs, we measured the transmission efficiencies of AOM S1 in double-pass configuration for several frequencies. We changed the driving frequency of the AOM and re-optimized the transmission after the double-pass for the first order diffraction, which gives a frequency shift of two times the driving frequency. Figure 4.4 shows the double-pass efficiency as a function of the frequency shift. We see an about 260-MHz broad profile with a peak efficiency of about 0.8 at 330 MHz. As we have enough light for the frequency shifting setup available, both AOMs can be used with a low diffraction efficiency of about 10% in double-pass configuration. Therefore, we can shift the frequency in a range of about $260 - 520$ MHz with one AOM in double-pass

[5] To create the sidebands on the light, an electro optical modulator (Linos PM25) with high transmission is used.
[6] AOM 1 and AOM 2 are Brimrose Model TEF80
[7] Crystal Technology, Inc. - AOMO 3200-125 (200 MHz)
[8] Thorlabs - PM-460

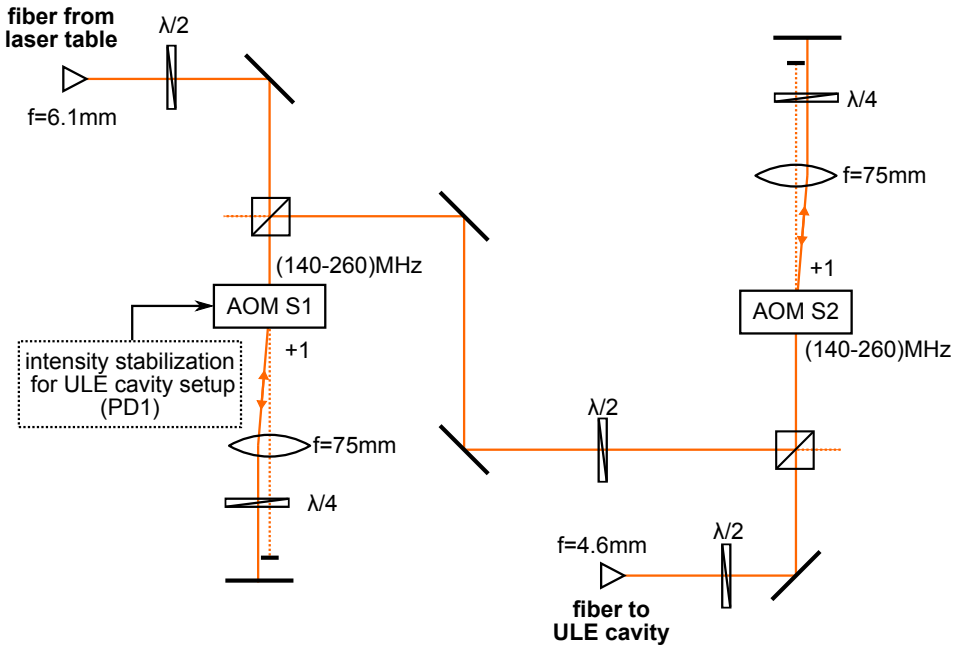

Figure 4.3: Optical setup for tuning the frequency of the laser relative to the transmission frequency of the ULE cavity. Here, the setup is shown for the two AOMs in double-pass configuration using the $+1^{\text{st}}$ order diffraction, also denoted as DP+DP+.

and about $130 - 260\,\text{MHz}$ in single-pass.

To continuously tune the dye laser-frequency, while the laser is locked to the ULE cavity, we have to bridge the FSR of the ULE cavity, which is about 1 GHz. For this, we combine the two AOMs in three different configurations; see Tab. 4.1.

Table 4.1: Frequency-shifted ranges for three combinations of the two AOMs S1 and S2. Double-pass is denoted as DP, single-pass as SP. Using the plus 1^{st} order is denoted as '+', minus 1^{st} order as '-'. Using these combinations together with the periodicity of our FSR of 1 GHz provides continuous tuning of the locked laser.

AOM combination	shifted frequency range (MHz)
DP+DP+	+520 to +1040
DP-DP-	-1040 to -520
DP+SP+	+390 to +780

If we want to change the lock to a different erbium isotope, we need to simply change the driving frequencies for the two AOMs. To calculate these frequency changes, we have to consider the following relevant frequencies:

- The transition frequency of the target Er isotope, which is denoted as ν_{atom}.

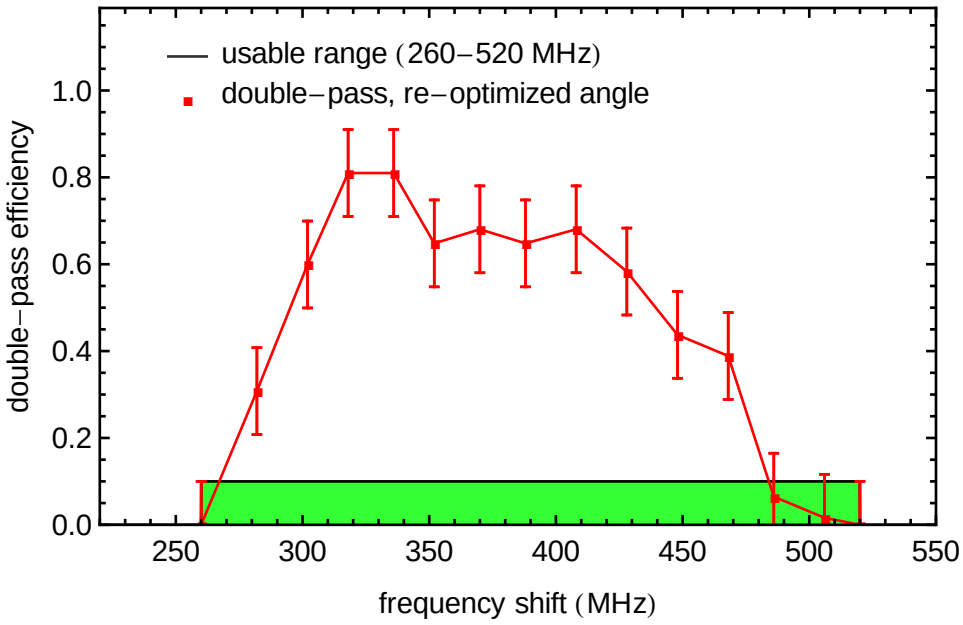

Figure 4.4: Measurement of the transmission efficiency through the double-pass system for different frequency shifts. For each datapoint, we re-optimized the adjustment of the double-pass setup. Further, the frequency range for efficiencies higher than 10% is shown.

- The transition frequency ν_{cav} of a TEM_{00} mode of the ULE cavity, which is a multiple of the free spectral range.
- All frequency-shifting elements inside the beam path between the ULE cavity and the MOT chamber are important, which are three AOMs; AOM 1 (in Fig. 4.2), AOM S1 and AOM S2. We denote the corresponding frequency shifts as ν_1, ν_{S1} and ν_{S2} respectively.

The following condition has to be fulfilled for resonant locking

$$\nu_{\mathrm{atom}} = \nu_{\mathrm{cav}} + \underbrace{(\nu_1 - \nu_{\mathrm{S1}} - \nu_{\mathrm{S2}})}_{\Delta\nu_{\mathrm{shift}}}. \tag{4.1}$$

An overview of how the different frequencies are connected is shown in Fig. 4.5. We measured ν_{atom} of ^{166}Er relative to ν_{cav} by spectroscopic means. The corresponding shift is

$$\Delta\nu_{\mathrm{shift}} = -592.72(1)\,\mathrm{MHz}. \tag{4.2}$$

This value has been measured on the 21.11.2011 and changes about 2 MHz per month due to a drift of the ULE cavity.

4.1.3 Optical setup for the ULE cavity

Figure 4.6 shows the optical setup for the ULE cavity. Light coming from the frequency-shifting setup is collimated with a $f = 6.1$ mm fiber coupler to a beam width of about 1 mm.

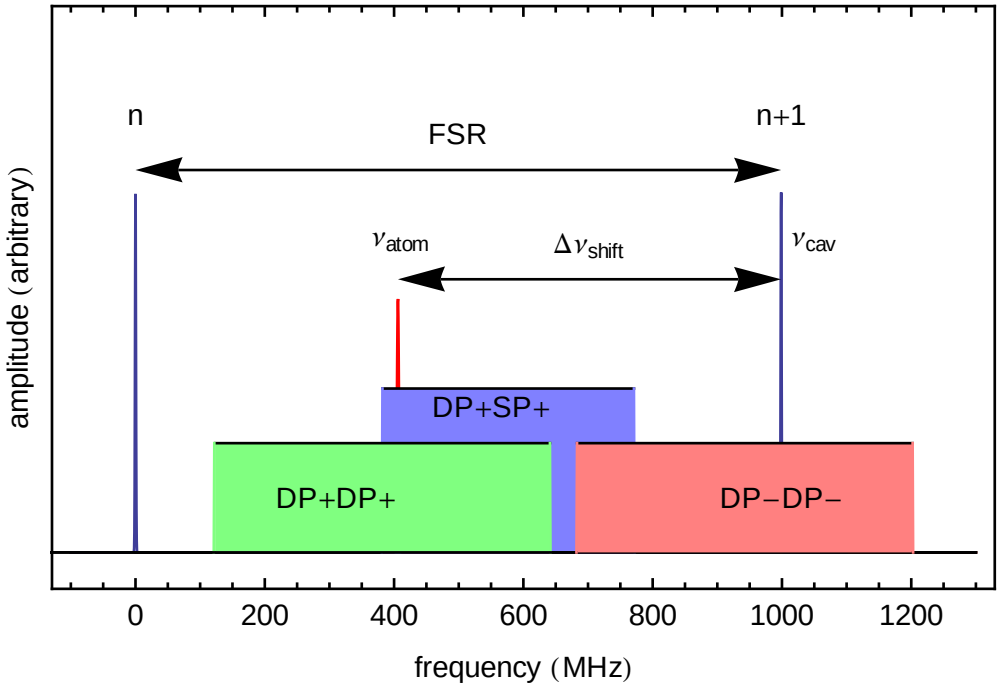

Figure 4.5: Position of the different resonances in frequency space. The plot shows an atomic resonance of Er, the nearby cavity resonances and the regions which are accessible due to a shift of the three AOMs 1, S1 and S2. In this example AOM 1 shifts the frequency by 162 MHz. The regions DP+DP+ and DP+SP+ are shifted relative to the mode 'n+1', whereas the region DP-DP- is shifted relative to the mode 'n' to illustrate the capability of continuous tuning.

The intensity of the light is stabilized after the reflection of the first PBS. The intensity stabilization setup stabilizes the light entering into the cavity at a level of about 100 µW. The error signal for locking the dye laser to the cavity is generated by a PDH setup; see Sec. 4.2. The light is sent through an EOM[9] for sidebands generation. To match the polarization axis of the light with the crystal axis of the EOM, a half-wave plate before the EOM is used. A good matching is necessary to minimize polarization fluctuations produced by the EOM crystal. After the EOM, a lens with a focal length of 500 mm is used to focus the collimated beam to a beam having a waist of about 200 µm at the position of the plane cavity mirror. Two mirrors before the cavity are used to couple the light with the correct angle and direction. The curved mirror is made of fused silica, and therefore, the substrate has a refraction index of about $n = 1.5$. This mirror has a radius of curvature ρ of 400 mm and thus, is working as a plano-concave lens with a focal length of $f = -800$ mm. We found a distance of about 35 mm between the 500 mm lens and the curved cavity mirror to give a good cavity coupling.

[9]Linos PM-CBB

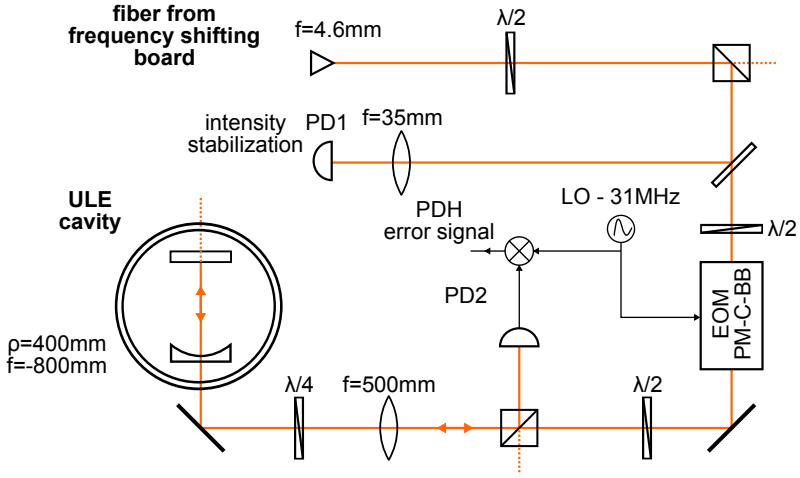

Figure 4.6: Optical setup for coupling the light to the cavity and generating the PDH error signal for locking. Further, a PD is used to stabilize the light after the first PBS.

4.1.4 Spectroscopy setup

To find the exact transition frequencies of the 583-nm line for the different isotopes of erbium, we perform spectroscopic measurements on erbium. A vapor of Er atoms is generated via

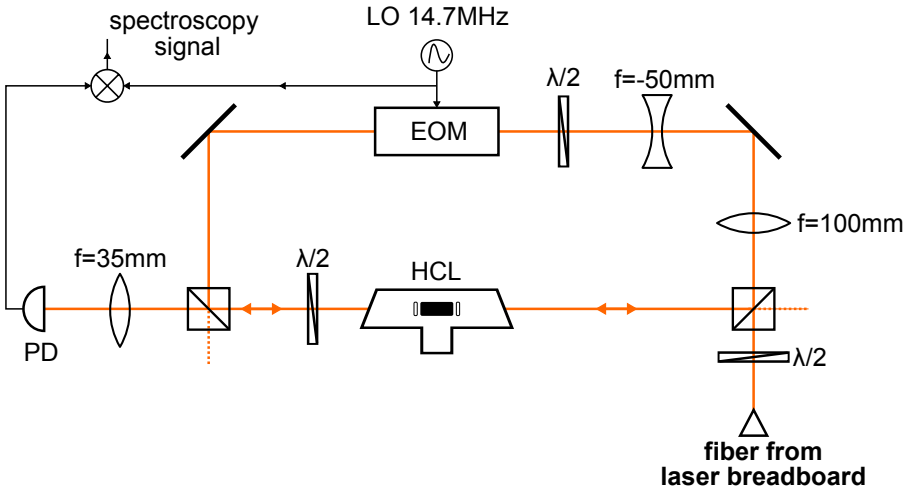

Figure 4.7: Scheme of the optical setup for the modulation-transfer spectroscopy. The probe- and phase-modulated pump beam are overlapped inside the hallow cathode lamp (HCL). By phase-sensitive detection of the probe beam signal, a spectroscopy signal is obtained.

a discharge process in a hollow cathode lamp (HCL). Due to the high melting point of Er, normal vapor cells are not available. The hollow cathode lamp is a glass-tube with an Er coated cathode inside. The tube is filled with argon serving as a buffer gas at a pressure of about 4 mbar. By applying high voltage to the electrodes Ar atoms are ionized, and are then accelerated towards the cathodes sputtering off Er atoms. To obtain a signal, we use modulation transfer spectroscopy [Raj80, McC08]. This technique is based on pump-probe

schemes to reach sub-Doppler resolution. The spectroscopic setup is schematically illustrated in Fig. 4.7.

The light coming from the laser breadboard via a fiber is split up by a PBS into pump- and probe beam in transmission and reflection, respectively. The beam diameter of the pump beam is scaled down by a telescope, to match the aperture of the EOM. The EOM is driven by a local oscillator (LO) at about 14.7 MHz imprinting sidebands onto the pump beam. The pump beam is then overlapped with the probe beam inside the HCL. If the frequency of the light is resonant to an atomic transition of Er, the sidebands are transferred via four-wave mixing onto the probe beam. By mixing the signal of the photodiode detecting the probe beam with the local oscillator, we obtain the spectroscopy signal. This signal is dispersive-like, as shown in Fig. 4.8. Three transitions of the bosonic and five transitions of the fermionic isotope can be identified. The signal has a flat, nonzero baseline, and is very sensitive to the alignment of the probe and pump beam due to interference effects. This gives rise to frequency uncertainties in the order of MHz. Therefore, with the present setup the signal can not be used for locking the dye laser.

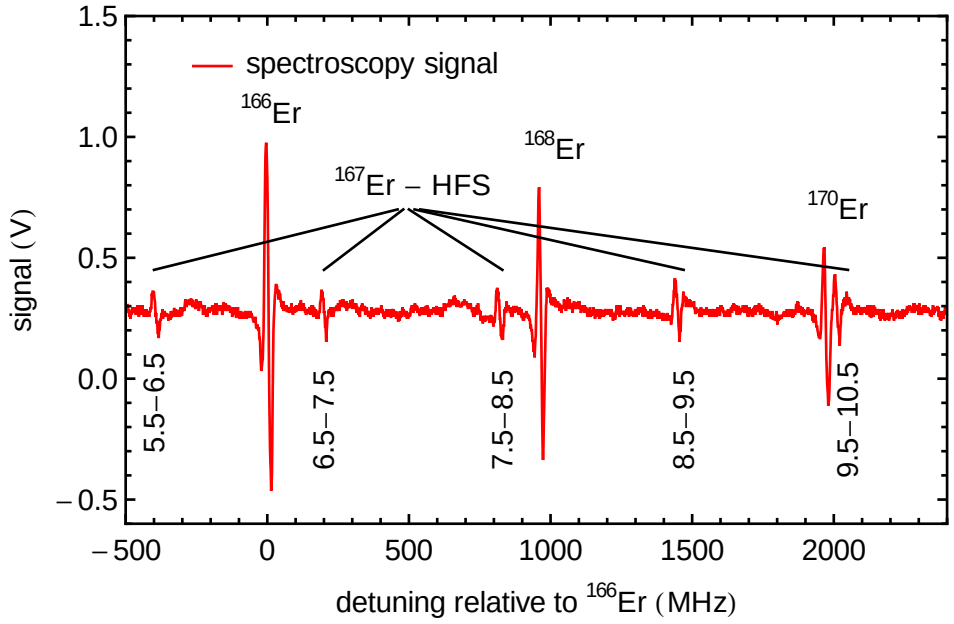

Figure 4.8: Signal of the modulation transfer spectroscopy. Three transitions of the bosonic species and five hyperfine transitions of the fermionic isotope have been identified. The hyperfine transitions are denoted by $F \rightarrow F'$. A theoretical calculation of the hyperfine states is found in App. C.

4.2 Pound-Drever-Hall locking

Stabilization of the laser frequency (locking) is performed with a servo loop, which involves techniques to generate an error signal. The error signal is then transformed into a feedback signal with a servo. The feedback signal is applied to an element capable of changing the frequency of the laser. An introduction into the theory of a commonly used servo, the Proportional-Integral-Device (PID) is given in Ref. [Tie99].

The PDH locking scheme is widely used to lock a laser to a cavity. Its advantage is that the locking range can be chosen independently of the steepness of the zero-crossing. Further, the detection mechanism using the reflection from a cavity is sensitive to the phase of the involved light field providing locking-bandwidths in the order of several MHz.
A PDH error signal is created by phase modulating a laser beam, which imprints sidebands at the modulation frequency, sending it to a cavity and detecting the reflection from the cavity. The reflection is separated by the incoming beam via a polarizing beamsplitter and a quarter-wave plate; see Fig. 4.9. The sidebands on the signal create a beat signal with the carrier. The phase of these signals depends on the detuning of the carrier from resonance and by detecting this phase with a LO, the error signal is obtained, which can be used for feedback onto a laser. In the following the error signal for the ULE cavity is discussed. The theoretical background for the PDH locking technique is found in App. A.

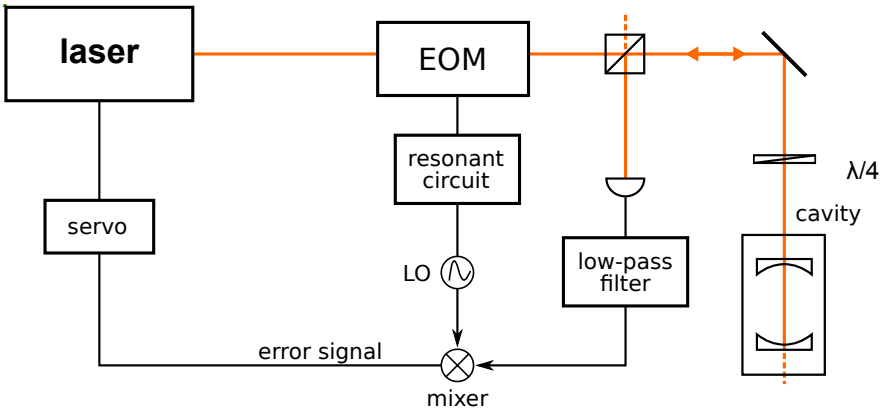

Figure 4.9: PDH locking setup. The EOM creates sidebands on the light, which is then reflected from the cavity and detected by the photodiode. The error signal is created by filtering the detected signal with a low-pass filter, which has a cutoff frequency above the local oscillator frequency, and mixing it with the LO. A servo generates the feedback signal. Often a resonant circuit is used to amplify the voltage over the EOM.

4.2.1 PDH error signal of the ULE cavity

An overview of the most important parameters for our PDH error signal can be found in Tab. 4.2. For creating our error signal we use an EOM[10]. The facets of this crystal are cut at

[10]Linos - PM-C-BB

Brewster's angle and therefore, residual amplitude modulation (RAM) is minimized, whereas the transmission is maximized. RAM creates an offset of the error signal after the mixer and therefore, has to be reduced to a low level for a good locking performance. Using a LO running at 31 MHz and a resonant circuit to amplify the voltage drop over the EOM (see Fig. B.2), we get sidebands having about 25% of the carrier height ($Ps/Pc \approx 0.25$), which corresponds to a modulation index of roughly 0.9. This value is only about 5% below the optimum value achievable for the slope of the error signal. As a low-pass filter we use a filter with a cutoff frequency at 60 MHz. The beam intensity incident on the cavity is 100 µW. We get an error signal that has a peak-to-peak amplitude of about 1.8 V and a slope of about 4 mV/kHz; see Fig. 4.10.

Table 4.2: Parameters connected to the PDH error signal.

LO frequency	31 MHz
Ps/Pc	0.25
modulation index	0.9
peak-to-peak amplitude	1.8 V
slope	4 mV/kHz
intensity incident on cavity	100 µW

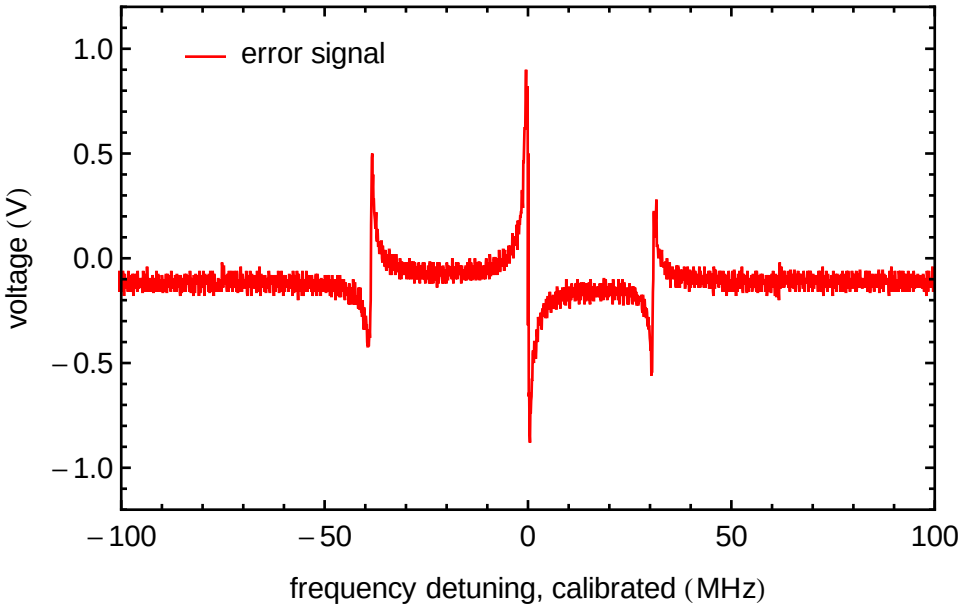

Figure 4.10: PDH error signal for the ULE cavity. The sidebands are at ±31 MHz, which is the EOM modulation frequency. The distance between the two largest extrema in frequency space is corresponding to the linewidth of the cavity. The baseline of the signal is not at zero, because of a standard offset of the photodiode electronics.

Chapter 5

Measurements

In this Chapter, we present measurements related to the ULE cavity and the linewidth of the yellow light. We measure important parameters like the free spectral range, finesse, and zero-expansion temperature of the ULE cavity. Finally, we investigate the long-term stability of the ULE cavity and the linewidth of the locked laser.

5.1 Free spectral range

To determine the FSR of the ULE cavity, we make use of two adjacent cavity TEM_{00} modes and the ^{166}Er atomic resonance at 583 nm. We lock the dye laser to each cavity mode separately and measure the corresponding frequency shift to the ^{166}Er atomic resonance; see Fig. 5.1(b). To resolve the atomic resonance, we image the atomic cloud in the MOT chamber and we scan the frequency of the yellow light with AOM 2 (see Fig. 4.1 - "yellow imaging").

The cavity modes are separated by one FSR and their transmission frequencies are denoted as $\nu_{\mathrm{cav,n}} = n \cdot \mathrm{FSR}$ and $\nu_{\mathrm{cav,n+1}} = (n+1) \cdot \mathrm{FSR}$. The frequency shifts $\Delta\nu_{\mathrm{s},1}$ and $\Delta\nu_{\mathrm{s},2}$ are a result of the combination of the frequency shifts performed by AOM 2, AOM S1 and AOM S2; see Figures 4.2 and 4.3. According to Eq. (4.1), the FSR is then given by

$$\begin{aligned} \Delta\nu_{\mathrm{s},1} &= \nu_{\mathrm{AOM2},1} - \nu_{\mathrm{AOMS1},1} - \nu_{\mathrm{AOMS2},1}, \\ \Delta\nu_{\mathrm{s},2} &= \nu_{\mathrm{AOM2},2} - \nu_{\mathrm{AOMS1},2} - \nu_{\mathrm{AOMS2},2}, \\ \mathrm{FSR} &= \Delta\nu_{\mathrm{s},1} - \Delta\nu_{\mathrm{s},2}. \end{aligned} \tag{5.1}$$

In order to get an accurate value for the FSR, we have to determine the peak position of the atomic resonance very precisely; see Fig. 5.1(a). For this spectroscopic measurement we already used our MOT, which we achieved during writing of this thesis. For a closer discussion on our Er MOT at 583 nm, see Chap. 6 and Ref. [Fri12]. The atomic spectroscopy measurement will be explained in more detail below.
The frequency shifts for AOM S1, AOM S2 and AOM 2 which are used to calculate the FSR are shown in Tab. 5.1. From these values, we calculate the FSR and the length of the cavity

Table 5.1: Frequency shifts of the AOMs for both measurement settings.

	frequencies for $i = 2$ (MHz)	frequencies for $i = 1$ (MHz)
$\nu_{\mathrm{AOM2,i}}$	162.618(10)	162.640(12)
$\nu_{\mathrm{AOMS1,i}}$	400.010	280.008
$\nu_{\mathrm{AOMS2,i}}$	355.328(10)	-523.338(6)
$\Delta\nu_{\mathrm{s,i}}$	-592.720(14)	405.970(14)

by using Eq. (3.6),

$$\mathrm{FSR} = 998.69(2)\,\mathrm{MHz}, \tag{5.2}$$

$$L = 15.0093(2)\,\mathrm{cm}. \tag{5.3}$$

The length is within the specifications given by the manufacturer of the spacer of the cavity.

Atomic spectroscopy on ^{166}Er at 583 nm - "yellow imaging"
For the measurement of FSR of the cavity, we need first to accurately determine the atomic transition frequency of ^{166}Er corresponding to the 583-nm line. We measure the atomic transition by performing absorption imaging on an atomic cloud released from the MOT with the yellow light. The probing light has an intensity of about $I \approx 36\,\mu\mathrm{W/cm}$, which is about 1/4 of the saturation intensity of the transition. The temperature of the atomic cloud has been measured by time of flight experiments [Pet02]. We found a temperature of $T \approx 20\,\mu\mathrm{K}$. For each data point a new sample is used, we scan the laser frequency with AOM 2 and image the cloud with a CCD camera.
The result of the measurement is shown in Fig. 5.1(a).

The scale of the y-axis is already converted to the number of atoms in the cloud.
We fit the data with a Voigt profile[1], because we expect both Gaussian and Lorentzian contribution to the lineshape. In the following, we discuss the lineshape as we expect it from theoretical considerations. In our case, the line is broadened by

- natural broadening, which has a Lorentzian shape with a FWHM $\Delta\nu_{\mathrm{nat}} = 190\,\mathrm{kHz}$.
- power broadening resulting from the intensity of the probing light. In first order power broadening changes the FWHM of the Lorentzian lineshape by a factor of $\sqrt{1 + I/I_s} \approx 1.12$. This changes the FWHM to about 210 kHz.
- thermal Doppler broadening, which results from the finite temperature of the sample. Thermal Doppler broadening gives a Gaussian lineshape with a FWHM calculated by $\Delta\nu_{\mathrm{Doppler}} = \sqrt{\frac{8kTln(2)}{mc^2}}\nu_{583}$, where m is the mass of an erbium atom and ν_{583} the transition frequency of the 583-nm transition. With a temperature of $20\,\mu\mathrm{K}$ we get Doppler broadening of $\Delta\nu_{\mathrm{Doppler}} = 127\,\mathrm{kHz}$.

[1] A Voigt profile is the convolution of a Lorentzian with a Gaussian profile.

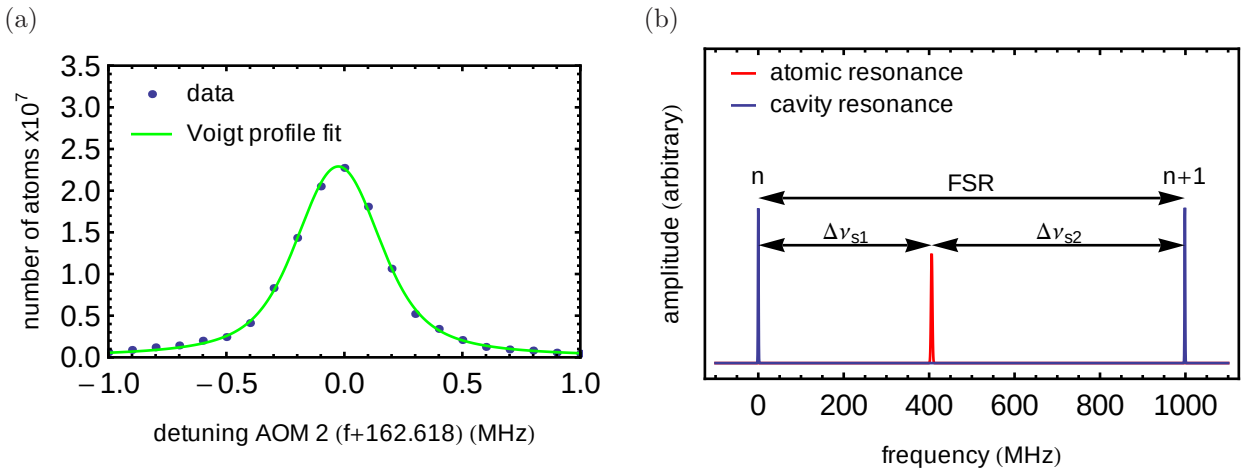

Figure 5.1: Measurement of the free spectral range. (a) Spectroscopy of the atomic clouds released by the MOT. The number of atoms detected by the 583-nm imaging light vs. the frequency shift performed by AOM 2 is plotted. The center of the peak is determined by fitting a Voigt profile. For the spectroscopy, we have a maximum expansion time of $tof = 25\,\mathrm{ms}$, $I/I_s = 0.25$, and $T = 20\,\mu\mathrm{K}$. (b) Schematics on the measurement of the FSR.

- the finite linewidth of the yellow light. The lineshape of a dye laser usually has Lorentzian shape. In our case, we measured the linewidth of our laser over a timescale of 10 ms and assume a Gaussian shape; see Sec. 5.5. The corresponding linewidth is $\Delta\nu_{\mathrm{laser}} = 45.0(1)\,\mathrm{kHz}$

- other broadenings, e.g. caused by the inhomogeneous magnetic field in the MOT chamber. During the spectroscopy measurement, the magnetic field produced by the Zeeman slower is still on and shifts the transition frequency of the magnetic substates dependent on the position in space. This can create an asymmetric type of broadening of unknown strength.

Therefore, we expect a spectral line with a Gaussian contribution of about 140 kHz and a Lorentzian contribution of about 210 kHz, with an additional unknown broadening due to the inhomogeneous magnetic field.
From the fit we extract the following values:

$$\Delta\nu_{\mathrm{Gaussian}} = 310(20)\,\mathrm{kHz}, \tag{5.4}$$
$$\Delta\nu_{\mathrm{Lorentzian}} = 140(20)\,\mathrm{kHz}. \tag{5.5}$$

The Lorentzian contribution is smaller than we expected, whereas the Gaussian contribution is about 100 % higher than we expected. This discrepancy could be to the inhomogeneous magnetic field, but further investigations are needed.

5.2 Finesse

In general, the finesse of a cavity is measured by scanning a laser over a cavity resonance and by that determining the linewidth of the cavity mode. This kind of measurement is only possible if the linewidth of the laser is much smaller than the linewidth of the cavity mode.

In our case, the linewidth of the 583-nm laser is in the order of linewidth of the ULE cavity and therefore, we use another technique to measure the finesse, the so-called ring-down measurement [Dem03]. Here, we measure the decay time of the light stored in the cavity. For this purpose, we first tune the laser to the cavity resonance for maximum transmission, which is done by locking the dye laser to the cavity. Then we use a radio-frequency (RF) switch connected to the RF-amplifier of AOM S2 (see Fig. 4.3) to suddenly switch off the intensity of the light coupled to the ULE cavity. The light transmitted through the cavity follows an exponential-like decay, which is measured by a photodiode.
Another important point is, that the speed of switching the intensity has to be shorter than the timescale corresponding to the bandwidth of the servo loop for the laser-frequency stabilization, because a frequency change during the measurement leads to interference effects. Our ULE cavity is only used for the slow part of the frequency stabilization, which has a bandwidth in the order of kHz. Therefore, we assume no influence on the stabilization.

The cavity ringdown is a process described by the following first order differential equation

$$\dot{y}(t) = \frac{1}{\tau}\left(-y(t) + u(t)\right). \tag{5.6}$$

In this equation $y(t)$ is the output intensity of the cavity, $u(t)$ is the input intensity and τ is the decay constant of the cavity. If the AOM switches off the intensity with infinite speed, $u(t)$ can be described by an step function $u(t) = \sigma(-(t - t0))$, where $t0$ is the switch-off time. This gives the well-known solution with an exponential decay with a characteristic time τ. In our case we use a Gaussian error function for the input function, which models our AOM switching process; see Fig. 5.2.

$$u(t) = \frac{a-b}{2}\left(1 + erf\left(-\frac{t-t0}{a4}\right)\right) + b. \tag{5.7}$$

Here, a and b are the values for the upper limit and the lower limit of the switching curve.

To be sure that the switching process has negligible influence on the exponential form of our decay curve, I compared the fit of a true exponential decay to a calculated solution of the numerical differential equation for the same decay time τ. This means that in Eq. (5.7), we have τ and $a4$ fixed, and adapt a, b and τ_0 manually to our data; see Fig. 5.3. We see, that there is a small influence of the switching process in the first 100 ns, but there is a negligible difference to a true exponential decay after the 100 ns. The decay time we get from the fit is

$$\tau = 297(1)\,\text{ns}. \tag{5.8}$$

We calculate the finesse and cavity linewidth by using the decay time, the measured FSR, and Equations (3.8) and (3.9).

$$\begin{aligned} \mathcal{F} &= 1865(6). \\ \Delta\nu &= 536(2)\,\text{kHz}. \end{aligned}$$

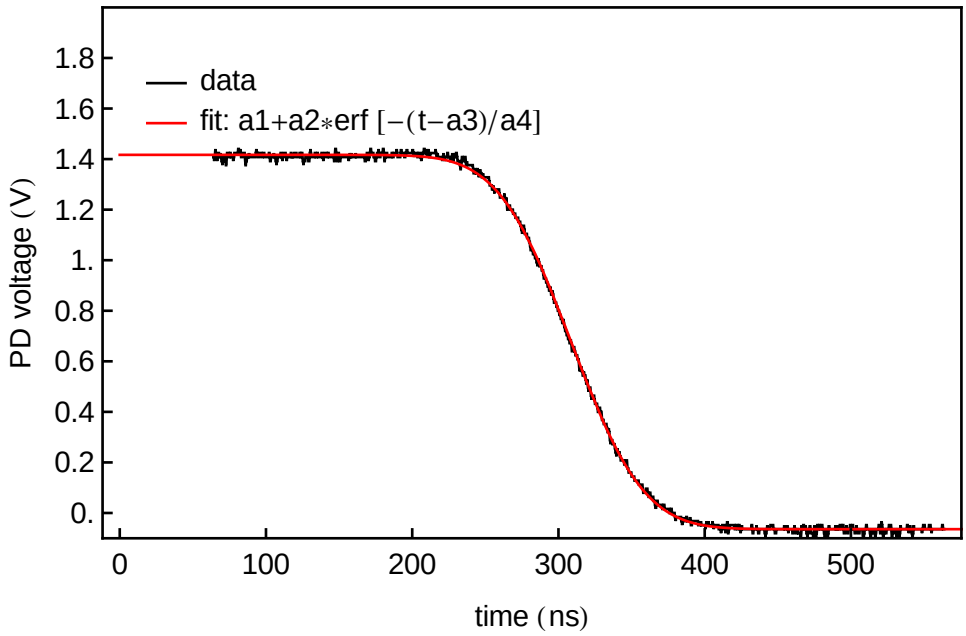

Figure 5.2: Switching curve of the AOM. For estimating the influence of the AOM response on the ringdown, we fit an errorfunction to this data to model the switching process numerically by a single parameter, which is $a4 = 55.3(1)$ ns. The other parameters $a1, a2, a3$ are used for adjusting the scaling, translation and offset of our data.

The finesse is not within specifications of the finesse calculated from the reflectivity specified by the company[2], which is 3500. There may be unexpected absorption losses due to dust or imperfect cavity coupling. However, the finesse is high enough for locking of the dye laser.

5.3 Zero-expansion temperature of the ULE cavity assembly

One of the advantages of using a spacer made of ultra low expansion glass is that the coefficient of the thermal expansion (CTE) has a zero-crossing around 20 °C, called zero-expansion temperature (T_C). If the temperature of the cavity is stabilized near this temperature, its length becomes insensitive to temperature fluctuations, which results in a low thermal drift of the cavity mode in the order of Hz/s.
We use a 15 cm long ULE spacer with fused silica mirrors optically contacted to it. The CTE of ULE is specified to below 3×10^{-8}/K and fused silica has a CTE around 500×10^{-8}/K. Due to the mismatch of the CTEs, the zero expansion temperature of the whole cavity assembly shifts to lower temperatures with respect to the T_C of the ULE itself. The rigidity of the optical contacted connections between mirrors and ULE spacer leads to a bending of the mirrors along the cavity axis. This bending causes a shift of the zero-expansion temperature of about −12°C for our cavity geometry, according to Ref. [Leg10].

[2] LayerTec

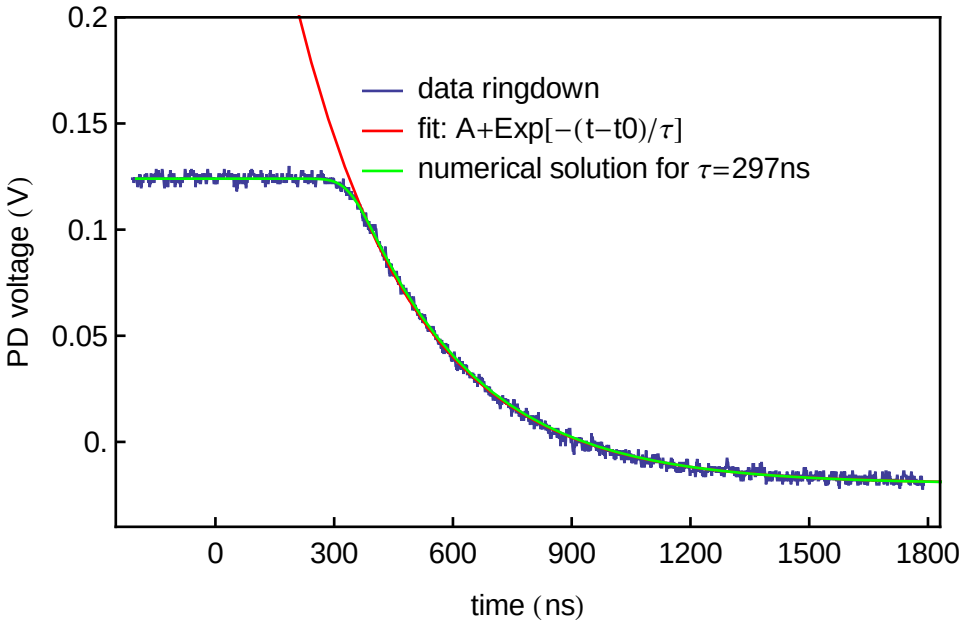

Figure 5.3: Cavity ringdown. We fit an exponential decay to the data, which gives a time constant of $\tau = 297(1)$. For validation of the assumption of a infinitely fast switching-off process, we compare the calculated solution for $\tau = 297(1)$ to our data.

We determine the zero-expansion temperature by changing the temperature of the cavity and measuring the resulting length change. The length change is connected to the thermal expansion properties of the ULE cavity. Near the zero-expansion temperature, thermal expansion has a strongly linear behavior [Leg10]. Therefore, we use a simple model where we describe the instantaneous CTE, $\alpha(T)$, around T_C by

$$\alpha(T) = a(T - T_C), \tag{5.9}$$

where a is the linear coefficient of thermal expansion. For ULE cavities, a has typically a value around $2 \times 10^{-9}/\mathrm{K}^2$.

Small temperature shifts lead to a small length changes, which is described by the following equation

$$\mathrm{d}L = L\alpha(T)\mathrm{d}T. \tag{5.10}$$

The relative change in frequency is directly connected to the relative change of the length and can be expressed as

$$\frac{\Delta\nu}{\nu} = \frac{\Delta L}{L} = \frac{a}{2}(T - T_C)^2 + C_0, \tag{5.11}$$

where C_0 is an integration constant which contains the term $(\frac{-a}{2T_c})^2$. To measure T_C, we changed the temperature of the cavity and we monitored the resulting frequency shift of a cavity mode with respect to the modulation transfer spectroscopy signal of the 583-nm transition in ^{166}Er; see Sec. 4.1.2.

Figure 5.4 shows the relative frequency shift as a function of the set temperature of the inner shield. We first changed the set temperature from about 0 °C to 6 °C and then to about

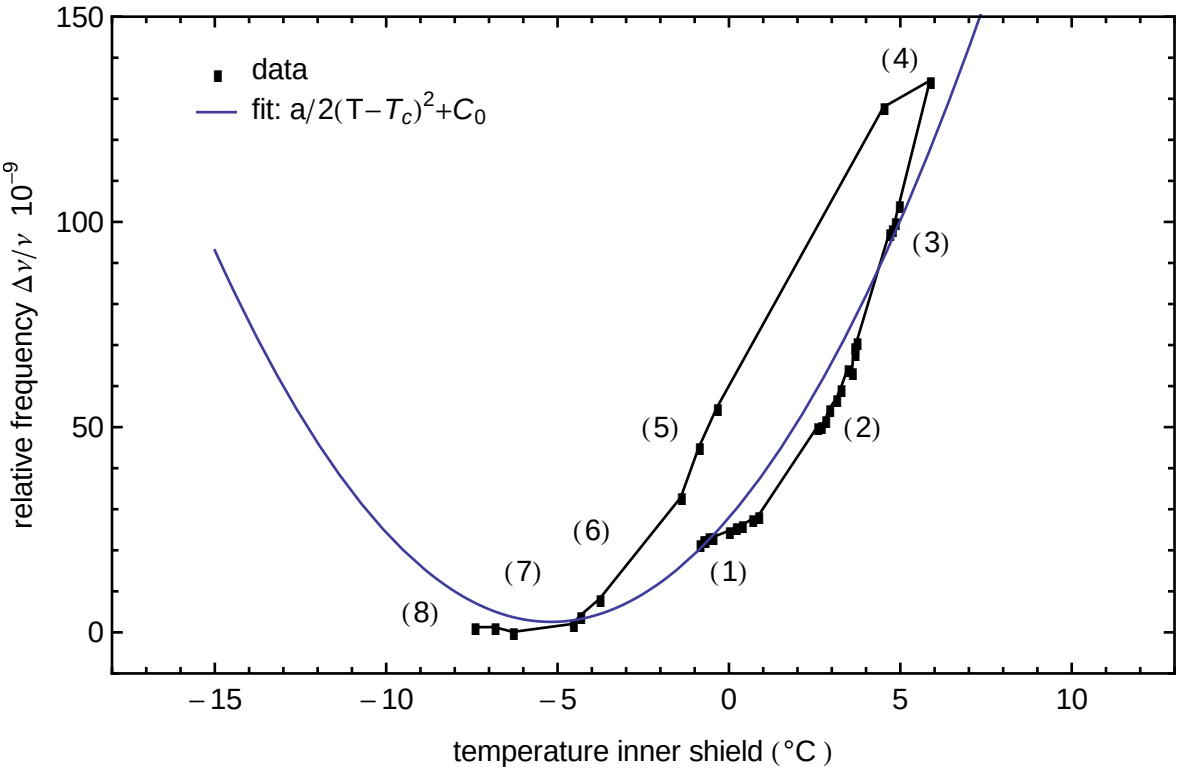

Figure 5.4: Plot of the relative frequency drift of the cavity versus the temperature of the inner shield. The measurement took 8 days, the time when the datapoints were taken are marked by "#" (in days). One can clearly see a hysteresis behavior, due to the time-delay in thermalization of the cavity. We fit a curve only taking the linear coefficient of thermal expansion into account, to get a rough estimation of the zero-expansion temperature of our cavity assembly.

−8 °C. The overall measurement took 8 days, as indicated in brackets. For the temperature measurement we had to use a PT1000 sensor attached to the inner heat shield, since a direct measurement of the cavity temperature is not possible. The data clearly shows hysteresis behavior, which is caused by a fast change in temperature of the inner heat shield during the measurement. The temperature of the cavity was not able to follow instantaneously the change in temperature.

Equation (5.11) is not able to fully capture the observed behavior and leads to an estimation of T_C with a 800 mK error, which is far above the required precision level; see solid line in Fig. 5.4. The reason for this mismatch can be attributed to the fact that the model accounts for the actual temperature of the cavity while we consider the temperature of the inner shield. To overcome this problem, we need to set a more developed model which accounts for this difference.

Estimation of the cavity temperature

Here, we introduce a model based on thermal radiation heat transfer processes between two gray diffuse surfaces to estimate the temperature of the cavity as a function of the tem-

perature of the inner shield, following Ref. [Sie02]. Here, the term "gray" indicates that the radiation emitted by the surface of the material is described by a parameter called emissivity ϵ, which can have a value between one and zero. The model considers diffuse surfaces. This means that the radiation incident on a spot of the surface is reflected into all directions, according to the Lambertian law.
Let us assume a radiation exchange between two concentric diffuse-gray spheres with uniform temperature, see Fig. 5.5(b). The relevant parameters describing the problem are the so-called net energy loss Q_k from a surface k having area A_k. This net energy loss is composed of the outgoing thermal radiation per unit area (flux) $q_{o,k}$ and ingoing flux $q_{i,k}$. Other important parameters describing the radiation process are the emissivity ϵ_k and the temperature T_k of the surface. To solve the problem, we set up the following relations.

(a)

parameter	value
A_{iS}	$0.062\,\mathrm{m}^2$
A_{cav}	$0.034\,\mathrm{m}^2$
ϵ_{iS}	0.07
ϵ_{cav}	0.92
m_{cav}	0.9 kg
c_{cav}	$767\,\mathrm{J\,kg^{-1}\,K^{-1}}$

(b)

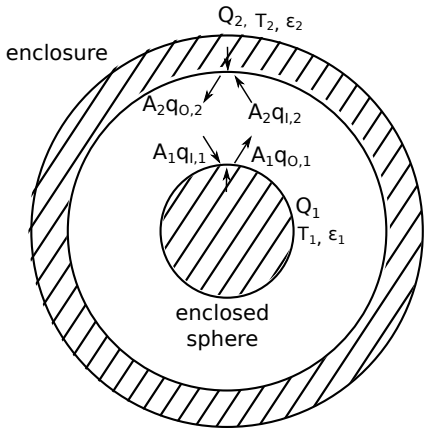

Figure 5.5: (a) Parameters used in the model for estimating the temperature of the cavity. The values for the area and volume of the spacer have been measured with a computer-aided design (CAD) software. The values for the emissivity for aluminum for the inner shield and roughened glass for the cavity are taken from Ref. [Ome03]. The value for the density of ULE is taken from [Cor08]. (b) Radiation heat transfer between two concentric gray and diffuse spheres. The parameters relevant are the temperatures T_k, the surfaces A_k, the emissivities of the involved materials and the radiative heat losses Q_k. These losses are composed of incoming and outgoing thermal radiation.

$$Q_k = (q_{o,k} - q_{i,k})A_k. \tag{5.12}$$

$$q_{o,k} = \epsilon_k \sigma T_k^4 + \underbrace{\rho_k}_{1-\epsilon_k} q_{i,k}. \tag{5.13}$$

The first equation is describing the energy balance. The second equation states, that the emitted flux is dependent on the temperature of the surface following the Stefan Boltzmann law of radiation including the reflected ingoing flux modified by the reflectivity ρ_k. The reflectivity is connected to the emissivity by $\rho_k = 1 - \epsilon_k$. Another relation is needed to solve the problem. Equation (5.14) is related to the geometrical arrangement of the two surfaces. For example, the outgoing flux from surface 1 completely reaches surface 2, whereas a part

of the flux emitted from surface 2 is also reabsorbed by itself. This geometrical arrangement of two surfaces is described by the so-called configuration factor F_{j-k}, which is the portion of flux emitted from the surface j reaching the surface k. Therefore, the relation

$$q_{i,k} = \sum_{j=1}^{2} F_{j-k} q_{o,k} \tag{5.14}$$

holds. In our case the configuration factors are $F_{1-2} = 1$, $F_{2-1} = A_1/A_2$ and $F_{2-2} = 1 - A_1/A_2$. If we combine the three Equations (5.12 - 5.14), we can reduce the problem to one equation, which connects the physical quantities relevant to our problem.

$$Q_1 = \frac{A_1 \sigma (T_1^4 - T_2^4)}{1/\epsilon_1 + (A_1/A_2)(1/\epsilon_2 - 1)}. \tag{5.15}$$

We extend the problem of the enclosed sphere to our more complicated geometry by taking the following assumptions into account:

- The inner shield is identified as the enclosure and the cavity is identified as the enclosed sphere.
- The geometrical arrangement between the cavity and the inner shield is not the one of two spheres. To compensate the change in configuration factors and other inaccurate assumptions of our model, we correct the whole equation by a free parameter α, which accounts for the model corrections.
- The net change of heat $Q_1 = \dot{Q}_{\mathrm{cav}}$ of the cavity spacer and mirrors is instantly transformed into a change in temperature according to the equation $\dot{Q}_{\mathrm{cav}} = \dot{T}_{\mathrm{ULE}} c_{\mathrm{cav}} m_{\mathrm{cav}}$. Here, c_{cav} is the specific heat of ULE and m_{cav} is the mass of our cavity.

Within these assumptions, we derive the differential equation (5.16), which gives a direct relation between the measured temperature at the inner shield $T_{\mathrm{iS}}(t)$ and the cavity temperature $T_{\mathrm{ULE}}(t)$.

$$\dot{T}_{\mathrm{ULE}}(t) = \frac{\alpha}{c_{\mathrm{cav}} m_{\mathrm{cav}}} \frac{A_{\mathrm{cav}} \sigma (T_{\mathrm{ULE}}^4(t) - T_{\mathrm{iS}}^4(t))}{1/\epsilon_{\mathrm{cav}} + (A_{\mathrm{cav}}/A_{\mathrm{iS}})(1/\epsilon_{\mathrm{iS}} - 1)}. \tag{5.16}$$

The fixed parameters A_{cav}, A_{iS}, c_{cav}, m_{cav}, ϵ_{cav}, and ϵ_{iS} are calculated based on the specifications of the spacer and the inner shield (geometry and material) and are listed in Fig. 5.5(a).

For solving this differential equation, we measured the temperature of the inner shield $T_{\mathrm{iS}}(t)$ for the whole measurement period with a resolution of better than 1 data point every 5 s; see Fig. 5.6(a). At the beginning of the measurement, the set temperature of the outer shield was ramped to about 6 °C. We see an exponential relation between the temperature of the outer and the inner shield. The time constant extracted from the exponential fit describes the shielding quality and is about 21 hours. At the end of day five of the measurement period we ramped the cavity set temperature to values around −8 °C. We stopped the measurement at the end of day 8.

The only free parameter of the model is α, which we determine using a fitting procedure that is explained in the following:

- First we solve differential equation (5.16) for several specific values of α, e.g. from 1.20 to 1.30 with a step size of 0.01; see Fig. 5.6(b). As a starting condition, we assume that $T_{\mathrm{ULE}}(0) = T_{\mathrm{iS}}(0)$, because we let the cavity thermalize for more than one week before we started the measurement.

- As a solution we get the temperature of the cavity $T_{\mathrm{ULE},\alpha}(t)$ depending on the model correction parameter α. We further assume that for one specific value of α, the model is valid.

- To validate our model, we create a dataset, where the y-values correspond to the relative frequency shift of the cavity at a certain time t (what we measured). The x-values of the dataset correspond to the corrected values of the temperature, which is now the temperature of the cavity at a certain time t. If we plot such a dataset, it looks comparable to Fig. 5.4. For a specific value of α, the hysteresis behavior of the data disappears. We find the right value of α numerically by fitting the quadratic curve given by Eq. (5.11) to the datasets. The hysteresis behavior is minimized if the quadratic fit matches best. We determine the matching of the fit by a parameter called residual sum of squares (RSS)[3], which we minimize with respect to α; see Fig. 5.6(b). We find that the model suits best for $\alpha = 1.25$.

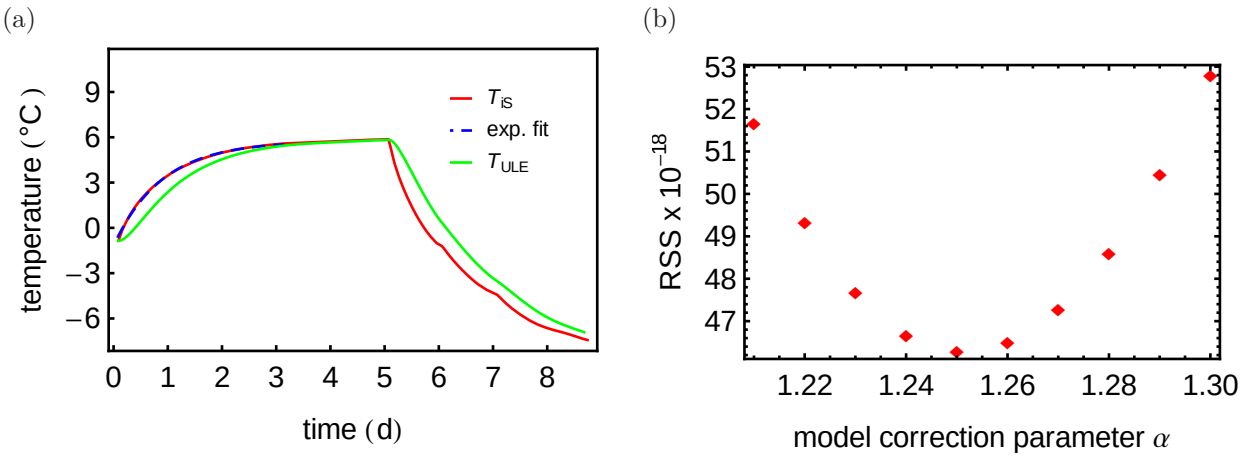

Figure 5.6: (a) Temperature of the inner shield T_{iS} during the measurement of the zero-expansion temperature. In this graph we also plot the temperature of the cavity, calculated by using the differential equation (5.16) for $\alpha = 1.25$. An exponential function is fit to the temperature curve of the inner shield to determine the time constant for the heat-exchange between inner and outer shield. (b) Plot of the model correction parameter versus the residual sum of squares (RSS), which measures the matching-quality of a quadratic fit to the corrected temperature data.

[3] $RSS = \sum_i (y_i - f(x_i))^2$, where y_i are the measured values and $f(x_i)$ are the predicted values from the fit.

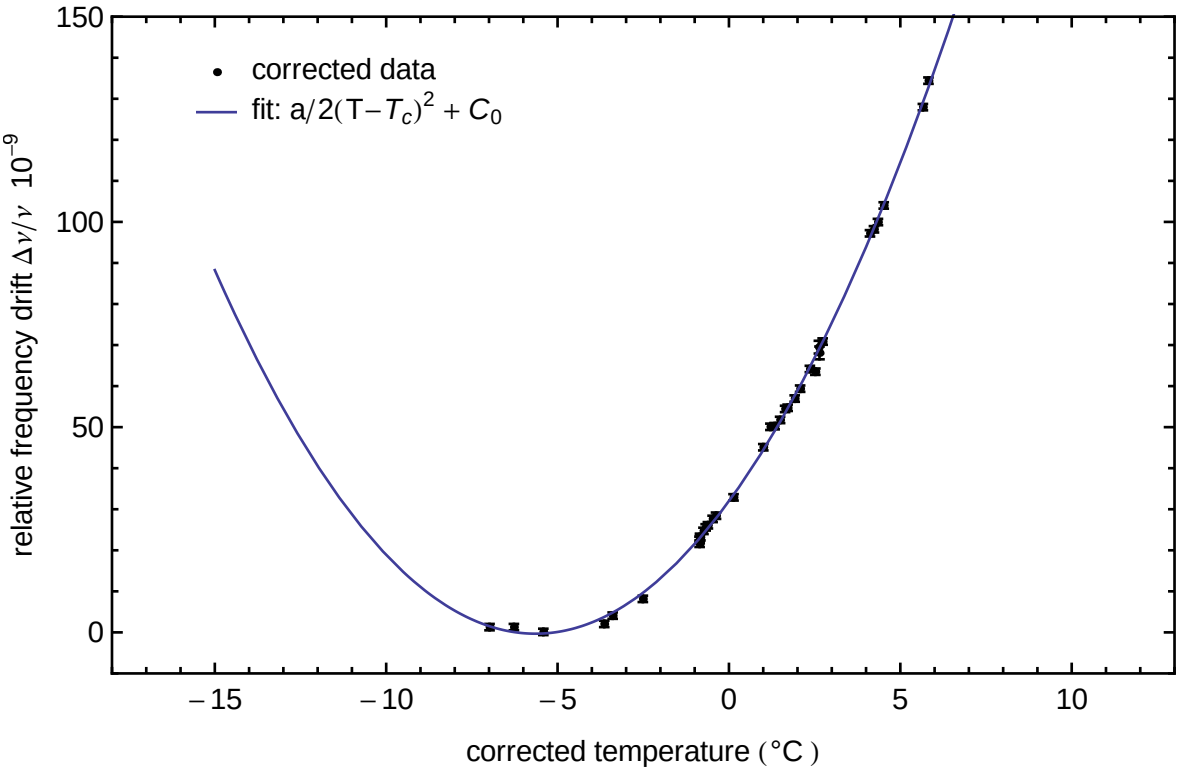

Figure 5.7: Plot of the relative frequency drift of the cavity versus the corrected temperature for the cavity. Now we clearly see a good agreement of the fit to our data within the error bars. With the corrected data, we are able to measure the zero-expansion temperature and the linear coefficient of thermal expansion accurately for our cavity assembly.

The data plotted as a function of the corrected temperature is shown in Fig. 5.7. We see a good agreement between the model and the data. From the fit we extract the following values for the zero-expansion temperature and the linear coefficient of thermal expansion.

$$a = 2.02(3) \times 10^{-9}/\mathrm{K}^2. \quad (5.17)$$

$$T_C = -5.65(9)\,^\circ\mathrm{C}. \quad (5.18)$$

The value for the linear coefficient of thermal expansion is similar to values found in literature [Leg10]. The zero-expansion temperature is significantly below room temperature. As we already noted at the beginning of this section, we experience a shift of the zero-expansion temperature of the cavity of about $-12\,^\circ$C with respect to the zero-expansion temperature of the ULE spacer due to the usage of fused silica mirrors. This means that the zero-expansion of the ULE spacer lies at about $6\,^\circ$C. Such a low value is not within the specifications given by the manufacturer of the ULE spacer, which usually lies at around $20\,^\circ$C. Anyhow, this problem is known in literature [Aln08] and we were prepared for this situation by using four Peltier units.

5.4 Long-term stability of the ULE cavity

Information about the long-term stability of our ULE cavity is important for our experiment. The sources of instability are temperature drifts, material aging [Aln08], or imperfections in the optical contacting as suggested in Ref. [Leg10].
Figure 5.8(a) shows the temperature of the outer and the inner shield over 10 days. We

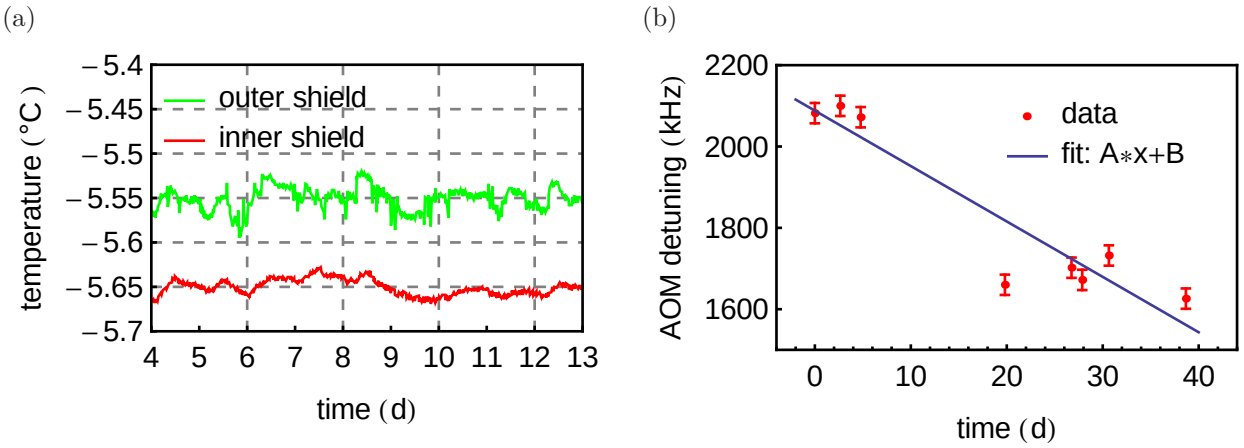

Figure 5.8: (a) Temperature of the inner shield and the outer shield measured over several days with two PT1000 sensors. The temperature difference between both shields is probably due to the error in manufacturing the sensors. (b) Temporal drift of the cavity over 40 days. The drift has been measured by comparing the locking setpoint relative to the ^{166}Er resonance measured with the "yellow imaging" setup.

take the fluctuations of the inner shield as a reference for the temperature excursion ΔT of the cavity itself for estimating an upper bound for frequency excursions due to temperature. We estimate ΔT to about 30 mK. By further assuming that we stabilized the temperature to 0.1°C within the zero-expansion temperature, we get a temperature sensitivity of about 100 Hz/mK. This results in a frequency excursion range of

$$\Delta\nu_{\text{temperature}} = 3\,\text{kHz}. \tag{5.19}$$

This value is low enough for our experiment, and we expect no large drifts due to temperature fluctuations.
We further measured the frequency drift of the cavity relative to the ^{166}Er atomic resonance via spectroscopy[4] on an erbium atomic cloud released from the MOT, over a timescale of about 40 days; see Fig. 5.8(b). We assume a linear drift and from the fit we extract a drift-rate of

$$\Delta\nu_{\text{drift}} = 0.16(2)\,\text{Hz/s}. \tag{5.20}$$

We see that the data are not fully matching the linear fit. We think that the problem is magnetic field fluctuations over a longer timescale as well as the magnetic field fluctuations

[4] same procedure as in Sec. 5.1. For determination of the peak position of the resonance Gaussian fits have been used.

during spectroscopy due to Eddy currents produced by the induced currents when switching off the MOT coils. Anyhow, it is improbable that the unknown magnetic field fluctuations compensate the real drift of the cavity, so this value should hold as an upper bound for the real cavity drift rate. Compared to literature values [Leg10], where the lowest temporal drift rate of several ULE cavities examined is about 0.1 Hz/s, our value is in the right order of magnitude and low enough for our requirements for the stability of the cavity.

5.5 Linewidth of the locked laser

The usual way to measure the linewidth of a laser is to beat it with another laser of the same wavelength and of similar or smaller linewidth. As we do not have another laser source at 583 nm available, we estimate the linewidth of the locked laser from the transmission signal of the ULE cavity.
Figure 5.9(a) shows the ULE cavity transmission signal over a timescale of 10 ms. The intensity noise of the transmission signal has components from three different noise sources.

- Laser intensity noise
- Laser frequency noise
- Photodiode noise

To estimate the photodiode noise, we measured the background voltage of the photodiode, which is $I_0 = -0.011(1)\,\mathrm{V}$. This means that fluctuations are in the order of 1 mV. Thus, we neglect the photodiode noise compared to the cavity transmission signal, which has about 10 times higher noise fluctuations.
We want to extract the laser frequency noise from the signal and convert it to a value in frequency space. If the light has zero intensity noise, the cavity transmission signal would be completely flat. Further, no fluctuations to higher voltages could be seen. A histogram of such a laser intensity noise-free signal would give a Gaussian-like distribution, which is cut at the center; see function "original f" in Fig. 5.9(b). To extract the pure frequency noise, we apply the following steps:

- The slowly varying component of the transmission signal is removed by subtracting the signal from its moving average having a averaging time of 0.4 ms; see Fig. 5.9. Here, we remove a large amount of pure laser intensity noise.
- The dataset for the corrected signal is used to create a histogram with a bin-size of 2 mV; see Fig. 5.9(b).
- There is still noise left, as we observe no pure distribution that is cut at the center. Therefore, we assume a function $g(x) \propto e^{-(\frac{x}{2\sigma_g})^2}$, which models the non-frequency noise source. This function modifies our original pure-frequency noise function $f(x) \propto \sigma_{\mathrm{step}}(x_0 - x)e^{-(\frac{x-x_0}{2\sigma_f})^2}$ by convolution, $f(x) * g(x)$. Here, σ_{step} is the step function.

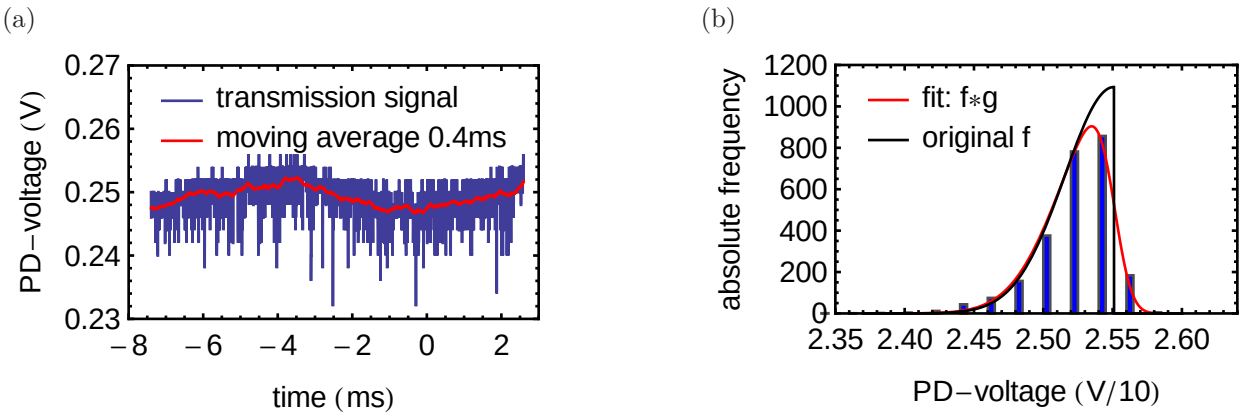

Figure 5.9: (a) Transmission signal of the cavity with the laser locked to it over a timescale of 10 ms. (b) Intensity noise spectrum of the transmission signal. A convolved curve $f*g$, where f is a "half-Gaussian" function describing laser frequency noise and g, which is Gaussian function describing non-laser other noise sources is fit to the data. Thereby we extract the original function f, which is also shown.

- We fit the convolved function $f(x) * g(x)$ to the data to extract the center x_0 of the function f.

From the fit we get $\sigma_g \approx 7\,\mathrm{mV}$, $\sigma_f \approx 36\,\mathrm{mV}$ and the parameter $x_0 = 0.2571\,\mathrm{V}$. This means that the contribution from pure laser frequency noise is about five times higher than the one given by the laser intensity noise and photodiode noise. The parameter x_0, which we will call the maximum intensity $I_{\max}$ in the following, is especially important, because with this parameter we are able to convert the voltage scale of the transmission signal into a frequency scale by using the ULE cavity transmission function; see Eq. (3.5). Rewriting this equation for our needs gives

$$I(\nu) = I_0 + \frac{I_{\max} - I_0}{1 + (\mathcal{F}\frac{2}{\pi})^2 \sin^2(2\pi\nu l/c)}, \quad -80\,\mathrm{kHz} < \nu \leq 0\,\mathrm{kHz}. \tag{5.21}$$

Here, $\mathcal{F} = 1865$ is the finesse of our cavity, $l = 0.15\,\mathrm{m}$ its length, and c the speed of light in vacuum. By converting the voltage axis with the inverse of the function above we get the following plot; see Fig. 5.10. We used the original data for the conversion except the last two bars from the right side of the histogram 5.9(b), which show a large discrepancy compared to the function f (black marked "half-Gaussian" profile). By fitting a Gaussian profile with a fixed center at 0 kHz, we estimate the upper bound of the laser linewidth to

$$\mathrm{FWHM}_{10\,\mathrm{ms}} = 45.0(5)\,\mathrm{kHz}. \tag{5.22}$$

This value is a factor of four smaller smaller than the natural linewidth of the 583-nm transition and therefore, fulfills our needs for the short-term stability of the dye laser.

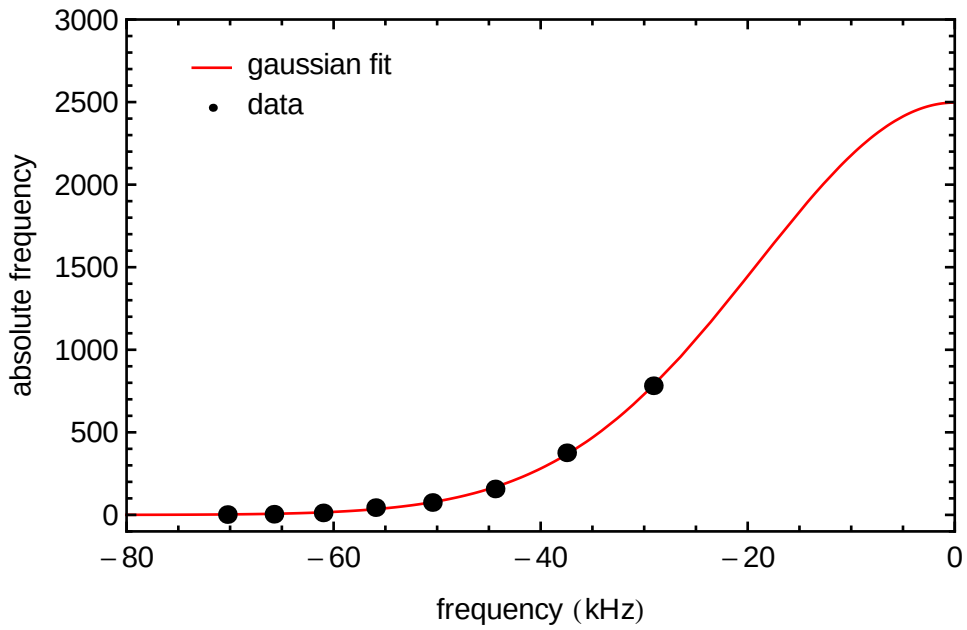

Figure 5.10: Frequency noise spectrum calculated by using the transmission function of the cavity. We fit a Gaussian profile to the data to estimate an upper bound for the laser linewidth.

Chapter 6

Conclusion and Outlook

The goal of my master thesis was to stabilize a dye laser such that it emits light at 583 nm with a linewidth below 190 kHz and that the laser has a stable locking performance for several hours meaning that the frequency drifts in the order of Hz/s.

For improving the long-term frequency stability, we locked the laser to an ultra low expansion cavity. The construction of the ULE cavity has been the main part of my work.

The ULE cavity consists of a spacer made of ultra low expansion glass with mirrors optically contacted to it. To gain a high degree of isolation from the environment, the cavity is surrounded by two thermal heat shields, placed inside a vacuum chamber with a pressure of about 10^{-8}mbar and cooled to the zero-expansion temperature. I further implemented a temperature stabilization and temperature monitoring.

Finally, all the measurements describing the performance of the locking setup have been carried out. We measured a FSR of 998.69(2) MHz, which is within specifications of the manufacturer. This value is also needed for changing the lockpoint to another isotope. The finesse has been measured by a cavity ringdown, the corresponding value is 1865(6). The determination of the zero-expansion temperature has been challenging due to the high thermal isolation of the heat shields and no possibility to measure the temperature of the cavity directly. Therefore, I introduced a theoretical model to account for the effect of a time delay in temperature between inner shield and cavity. We got an very accurate value of $T_c = -5.65(9)\,^{\circ}\mathrm{C}$. With knowledge of this value, we have been able to reduce the long-term drift of the cavity to an acceptable amount for our experiment. We observed a linear frequency drift of 0.16(2) Hz/s over a timescale of about one month. This value assures a high degree of frequency stability and therefore, the ULE cavity serves as a stable frequency reference.

The first result based on my work was the narrow-line MOT at 583 nm. The corresponding publication is given in App. D. In brief, the MOT is set up in a standard six-beam configuration. Our MOT beams have a diameter of about 30 mm to get a large capture volume. Typically, we use a laser intensity of 12 times the saturation intensity. With these parameters set, we achieve a MOT with a temperature as low as 15 µK and atom numbers up to 2×10^8. We further demonstrate a MOT for all the isotopes except the low abundant ^{162}Er; see Fig. 6.1. For the fermionic MOT, we use the $F = 19/2 \rightarrow F' = 21/2$ transition. We observe about 3×10^7 atoms, which is substantially below the atom numbers for the

bosonic isotopes. We think that this is due to the statistical weight of about 20% concerning the hyperfine states [Fri12].

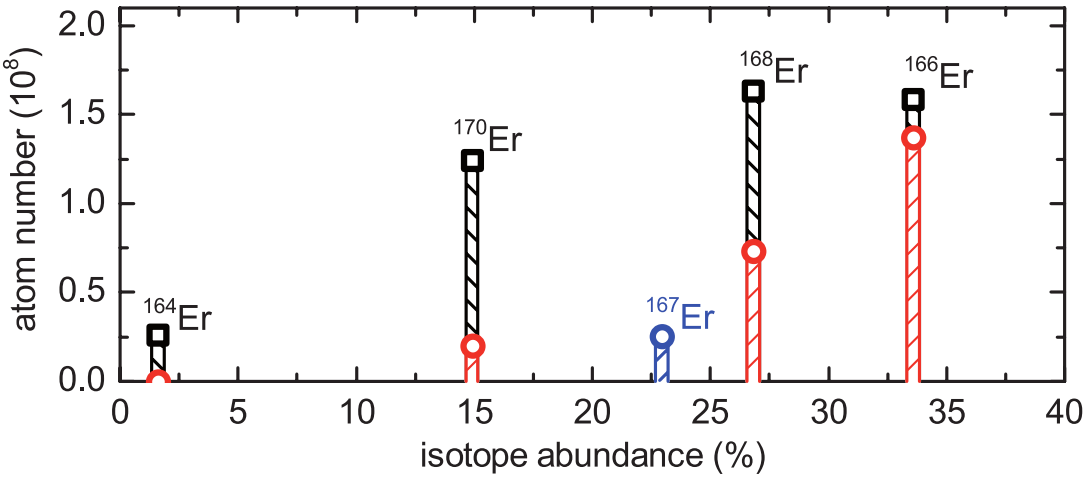

Figure 6.1: MOT behavior of different Er isotopes. Plotted is the atom number as a function of the natural abundance. Squares mark a MOT loading time of 20 s, circles a loading time of 5 s. Figure adapted from [Fri12].

Recently, we managed to load about 10^7 Er atoms from the MOT directly into a crossed dipole trap at 1064 nm. We then performed evaporative cooling and observed the first BEC for the ^{168}Er isotope [Aik12]. After 5 seconds of evaporative cooling, we achieve a BEC with $N = 8 \times 10^4$ atoms; see Fig. 6.2.

The next steps of our experiment will be the investigation of scattering properties and the production of a degenerate Fermi gas. Because of the more complex energy structure of the fermionic isotope, additional laser cooling stages can be needed. The ULE cavity developed during my master work can be used with even narrower transitions (e.g 841 nm), which can be used for cooling of the fermionic isotope.

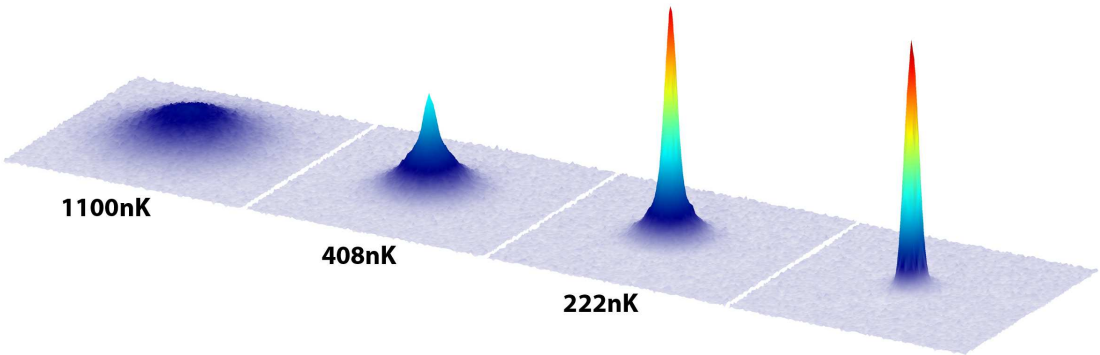

Figure 6.2: 3D density profiles of the Er cloud for different evaporation times show the BEC phase transition.

Appendix A

Cavity

A.1 Theoretical description of the PDH locking technique

In the following the PDH error signal is derived. Our discussion follows Ref. [Bla98]. The electric field of a monochromatic laser beam that is phase-modulated by an electro-optical modulator driven at frequency Ω, can be described by

$$E = E_0 e^{i(\omega t + \beta \sin \Omega t)}, \tag{A.1}$$

where β is the modulation index. The upper equation can be approximated for $\beta < 1$

$$E \approx E_0 \left(J_0(\beta) e^{i\omega t} + J_1(\beta) e^{i(\omega+\Omega)t} - J_1(\beta) e^{i(\omega-\Omega)t} \right), \tag{A.2}$$

where the $J_n(\beta)$ are Bessel functions. In first order, two sidebands at the sum and the difference frequency appear in addition to the carrier with their height depending on the modulation index. After phase modulation, the beam is sent to the cavity, where it is partially reflected and partially transmitted. The reflected component is the relevant one for the PDH locking scheme. The reflection coefficient $F(\omega)$ of the cavity depends on frequency and is given by the reflected monochromatic wave E_{ref} over the incident wave E_{in}; see Equations (3.2) and (3.3).

$$F(\omega) = \frac{E_{\text{ref}}}{E_{\text{in}}} = r \frac{e^{i\Phi(\omega)} - 1}{1 - r^2 e^{i\Phi(\omega)}}, \tag{A.3}$$

where r is the reflectivity of the cavity mirrors and $\Phi(\omega)$ the frequency dependent phase. To get an expression for the reflected phase modulated beam, the reflection coefficient has to be multiplied to the carrier and side-band signals. This gives

$$\begin{aligned} E_{\text{r}} &= E_0 (F(\omega) J_0(\beta) e^{i\omega t} \\ &+ F(\omega+\Omega) J_1(\beta) e^{i(\omega+\Omega)t} - F(\omega-\Omega) J_1(\beta) e^{i(\omega-\Omega)t}). \end{aligned} \tag{A.4}$$

A photodiode detects the power $P_r = \mid E_r \mid^2$ of the reflected wave, which leads to

$$\begin{aligned} P_r = 2\sqrt{P_c P_s} \quad \big(& \Re[F(\omega)F^*(\omega+\Omega) - F^*(\omega)F(\omega-\Omega)]\cos\Omega t \\ + & \Im[F(\omega)F^*(\omega+\Omega) - F^*(\omega)F(\omega-\Omega)]\sin\Omega t\big) \\ + & \text{(DC terms)} \\ + & \text{(}2\Omega\text{ terms)}, \end{aligned} \tag{A.5}$$

where $P_c = (J_0(\beta)E_0)^2$ is the power in the carrier and $P_s = (J_1(\beta)E_0)^2$ is the power in the sidebands. The terms oscillating at a frequency of 2Ω are filtered by low-pass filter. The DC part of this signal is negligible because by mixing the signal with a local oscillator (LO) at a frequency of Ω, only the signal proportional to the cosine or sine of Ω is detected, depending on the phase relation between LO and the signal. For a LO with 0° phase relative to the detected signal, the slope of the error signal has a maximum. This leads to

$$\epsilon = 2\sqrt{P_c P_s}\,\Im[F(\omega)F^*(\omega+\Omega) - F^*(\omega)F(\omega-\Omega)]. \tag{A.6}$$

The error signal with an optimized LO phase is illustrated in Fig. A.1. Assuming highly

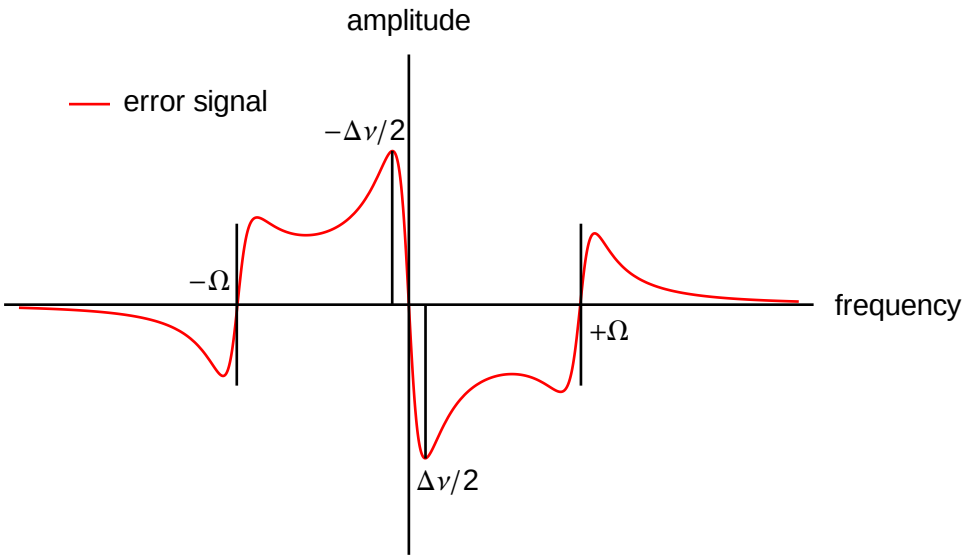

Figure A.1: Example of a calculated PDH error signal for a LO Phase of 0 °. The locking range is determined by the sideband-frequency Ω. The slope of the zero-crossing is dependent on the cavity linewidth $\Delta\nu$, which is also the distance between the two largest extrema in frequency space. The slopes at the sidebands have a different sign than the slope at the carrier frequency and thus, prevent locking to them.

reflective mirrors ($r \approx 1$) and a modulation frequency much higher than the linewidth of the cavity ($\Omega >> \Delta\nu$), the error signal near the zero crossing can be rewritten as

$$\epsilon = -8\frac{\sqrt{P_c P_s}}{\Delta\nu}\delta f. \tag{A.7}$$

Here δf is the frequency deviation of the laser from the cavity resonance. For a good locking performance, a suitable cavity linewidth has to be chosen and the part $\sqrt{P_c P_s}$ of the upper expression should be optimized depending on the modulation index β. The expression above is a product of the Bessel functions of first and second order and it is maximal for $\beta = 1.08$. At this modulation index, the approximation (A.2) is not valid anymore. However, the independence of the slope of the error signal on the modulation index is discussed in reference [Kir06].

A.2 Assembling of the ULE cavity

In this Section, I describe the crucial steps I followed for assembling the ULE cavity. Some problems and suggestions for improvement are also discussed. For visual support of my description, I will refer to a series of images, which have been made during the task of assembling the cavity; see Figures A.2 to A.11.

Cleaning of the cavity parts
All the surfaces of the parts that are inside the vacuum chamber had to be cleaned properly for high vacuum applications. For the cleaning of the cavity parts, I followed a procedure which has been previously successfully used in our group, combined with cleaning hints from Ref. [Bir05].
For parts contaminated with oil, mainly coming from our workshop, I used soap and distilled water for pre-cleaning. The main cleaning has been done with technical grade[1] acetone and isopropanol. For the aluminum parts, we additionally used "P3 Almeco 18"[2], which is a sophisticated free degreaser. In the following, the main cleaning steps are described.

1. Pre-cleaning with distilled H_2O and standard soap to remove oil and dirt. (only if necessary)
2. 10 min in supersonic bath at 60 °C. Solution: Almeco dissolved in distilled water with a concentration of about 30 g/L (only aluminum parts)
3. 10 min in supersonic bath at 40 °C. Solution: distilled water (only aluminum parts)
4. 15 min in supersonic bath at 40 °C. Solution: acetone
5. 15 min in supersonic bath at 40 °C. Solution: isopropanol
6. Cleaning surfaces with special wipes[3] and blasts of nitrogen

Viton degrades if exposed to acetone. Therefore, cleaning step 4. is not used for the V-block after the Viton has been glued to it. All the other parts, including the flanges, the Capton

[1] About 99.5% purity
[2] Henkel - P3 Almeco 18C
[3] VWR - Spec wipes

wires and the Peltier elements have been cleaned this way.

Viton cylinders
The spacer is supported on 4 Viton cylinders glued to the V-block. First, the cylinders have been cut from a large Viton ring. As a next step, they are glued into accurately fitting cutouts; see image A.2. For this, we use high temperature epoxy. After that, the V-block including the Viton cylinders has been machine-finished with a CNC-milling-machine while taking care not to contaminate the pre-cleaned V-block. Finally, the finished V-block has been cleaned with isopropanol only, as acetone degrades the Viton.

Temperature sensors
Inside the vacuum chamber we have placed six temperature sensors. Figure A.3 shows five of the sensors which are glued to the bottom plate of the outer shield with high-temperature epoxy. The sensors are soldiered to shielded Capton wires with vacuum soldier. For positional stability of the sensors, the Capton wires are clamped to the aluminum plate. For drying of the glue, we placed the whole aluminum plate on a heating plate.
There is an additional sensor (PT1000-3) glued to a side plate of the inner shield.

Peltier elements
For cooling of the cavity, we use four Peltier elements. In the beginning, we controlled all four Peltier elements connected in series. Unfortunately, three months after successfully controlling the cavity temperature in this way, one Peltier element broke and the resistance of a second Peltier increased. We think, that this problem occurred due to several heating and cooling cycles, which decreased the lifetime of the Peltier elements. Now we control only one Peltier and use a fixed current for two Peltier units left. We are still able to cool the cavity down to the zero-expansion temperature.
Figure A.4 shows the Peltier coolers (labeled PE1 to PE4), which are glued to the bottom plate of the outer shield with silver loaded epoxy[4].
When we first cooled down the cavity, the difference in thermal expansion coefficient of the Peltier, aluminum and steel put mechanical stress on the Peltier elements and the outer shield. There may be better solutions for connecting the Peltier surfaces. For instance by using a flexible graphite sheet and nylon screws for fixation.

Glass plates
Figure A.5 shows the two glass plates, which are glued to front- and back- plates of the outer shield. We use vacuum epoxy, which dries at room temperature. The usage of high temperature epoxy would put mechanical stress onto the glass plates due to the temperature gradient caused during the drying process. The glue is placed on the edges of the glass plates.

Closing the chamber
Figure A.6 shows the vacuum chamber before we closed it and pumped it off. We maneuvered the optically contacted spacer inside the heat shields by using wires.

[4]RS Components - This epoxy has a good thermal conductance.

Closed chamber
Figure A.7 shows the finished vacuum chamber, which is already placed on the ULE cavity breadboard and surrounded by optics.

Optical contacting
We did the optical contacting ourselves in an clean room of ISO class 5. We recommend to do the contacting in a more clean atmosphere, but with a precise cleaning of the optics it was still possible.

First of all, we need to prepare the utensils we need for the process; see Fig. A.8. All the utensils are properly cleaned for usage in the clean room. We have a holder for the spacer made of Teflon, a lens to investigate the surface of the spacer, a bright light source, lens cleaning tissues. For cleaning of the surfaces, we use isopropanol and ethanol.

After bringing all the utensils to the clean room, we started with cleaning of the spacer by flushing it with isopropanol (Fig. A.9) and drying it with blasts of a clean nitrogen source. As a next step, we put the spacer into the holder and cleaned its end-facets with isopropanol in the beginning, and ethanol at last. The surface is ready for contacting if no dust at all can be seen anymore. After this task, the mirrors have been cleaned by using ethanol only, as the surfaces have been very clean from the beginning.

Figure A.10 shows the microscope in the clean room, which we used to inspect the mirror surfaces. Also here, no impurities should be seen. If all the surfaces are clean, we put the mirrors onto the spacer facets and put pressure on them. If the spacer is successfully contacted, no interference stripes should be seen anymore and one is able to lift the whole assembly by pulling the mirrors only. If the contacting is not successful, one should put some methanol between the surfaces and slide the mirror to the side and rip it off at a place, where the surface damages do not disturb a further try of contacting. Figure A.11 shows the successfully contacted spacer.

Electric wiring inside the vacuum chamber
Figure A.12 shows how the six temperature sensors and the four Peltier elements are connected to the D-Sub 25 pin connector on the vacuum side.

A.3 Cavity temperature monitoring

For logging the temperature of the inside of the cavity, we use a data logger[5], which has a 24-bit voltage resolution in a voltage range of 0 to 2.5 V which gives a temperature resolution of about 1 mK if used with our PT1000 sensors. For transforming the resistance of the temperature sensors into voltage, we use a measurement bridge; see Fig. A.13. Four precision resistors measure the voltage drop over the sensors; we use the NTC-2 and the three PT1000 sensors for the monitoring. As a reference voltage, we use the internal 2.5 V voltage reference of the Pico data logger, which we measured in the used configuration to $V_{\mathrm{Ref}} = 2.4973\,\mathrm{V}$. It is very important that all the four sensors are connected to the logger at the same time because one disconnection changes the total current and has an influence on the reference voltage in the millivolt-range, which can cause a change in the measured temperature of up to 1 °C.
The NTC-10K[6] sensors we use are linearized in the following way.

$$T(R_{\mathrm{NTC}})/^{\circ}\mathrm{C} = \frac{B \cdot T_n}{B + ln(R_{\mathrm{NTC}}/R_n) \cdot T_n} - 273.16. \tag{A.8}$$

Here, R_{NTC} is the resistance of the used sensor, $B = 3450$ is a material constant, $T_n = (273.16 + 25)\,\mathrm{K}$ is the nominal temperature and $R_n = 10\,\mathrm{k}\Omega$ is the nominal resistance of the sensor.
For the PT1000 sensors[7], we transform the resistance into temperature in the following way.

$$T(R_{\mathrm{PT}})/^{\circ}\mathrm{C} = \frac{R_{\mathrm{PT}} - 1000}{TCR} 10^{-6} + \delta. \tag{A.9}$$

Here, R_{PT} is the resistance of the sensor, and $TCR = 3.85 \times 10^{-6}$ is the temperature coefficient of the sensor. The offset $\delta = -1.076$ is introduced by us. It is only used to calibrate the temperature of the PT1000 sensors at the zero-expansion temperature. We get the value by manually measuring the resistance of the PT1000-3 sensor and comparing it to the resistance measured by the Pico data logger[8].
The voltage drop U over the temperature sensors is transformed into resistance by the following function.

$$R(U) = U \frac{R_{\mathrm{INP}} R_{\mathrm{PR}}}{V_{\mathrm{Ref}} R_{\mathrm{INP}} + U(R_{\mathrm{PR}} - R_{\mathrm{INP}})}. \tag{A.10}$$

In this equation, $R_{\mathrm{INP}} = 1\,\mathrm{M}\Omega$ is the input impedance of the measurement channel and R_{PR} is the resistance of the precision resistor (for values see Fig. A.13) used for the particular channel. By combining the three above equations, the measured voltage U is converted into temperature.

[5] Pico Technology - ADC-24
[6] EPKOS G560/10K/+
[7] INNOVATIVE SENSOR TECHNOLOGIES - Platinum 600 °C MiniSens
[8] The resistance of the PT1000-3 sensor is 978.2 Ω at the zero-expansion temperature.

Figure A.2: Gluing of Viton cylinders

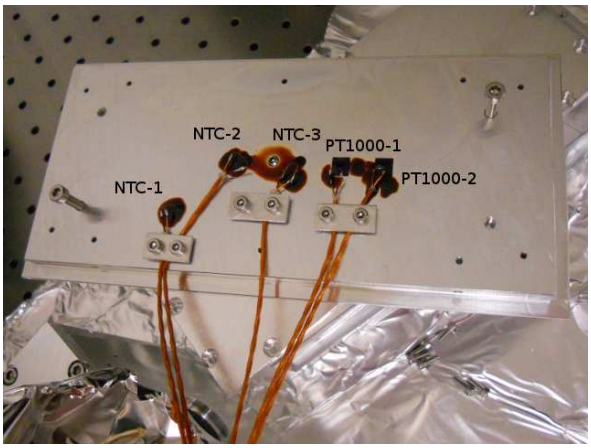

Figure A.3: Gluing of temperature sensors

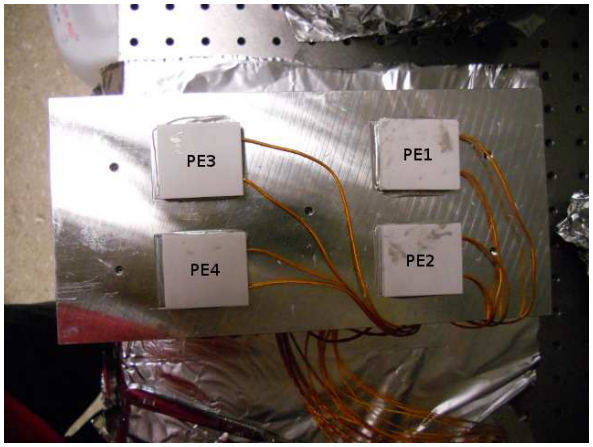

Figure A.4: Gluing of Peltier elements

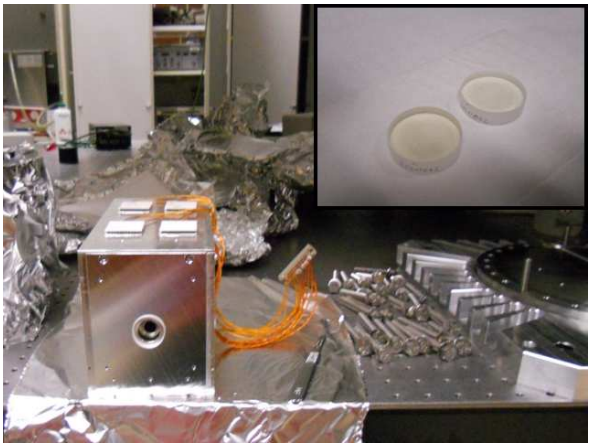

Figure A.5: Gluing of glass plates

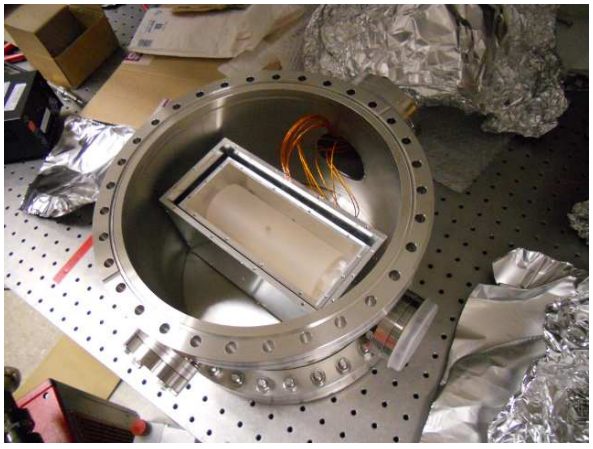

Figure A.6: Closing the vacuum chamber

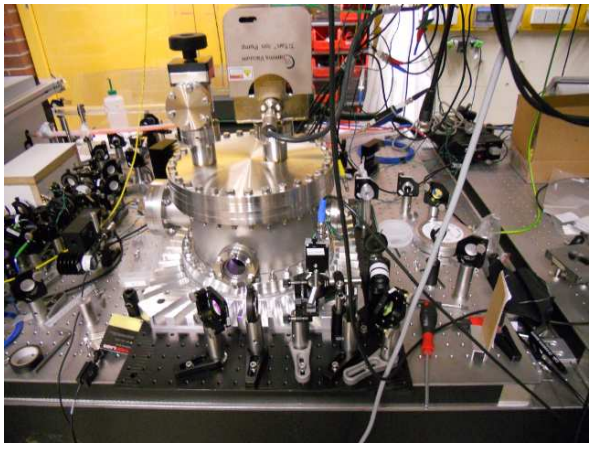

Figure A.7: Finished chamber

Figure A.8: Utensils used for optical contacting

Figure A.9: Cleaning of the spacer

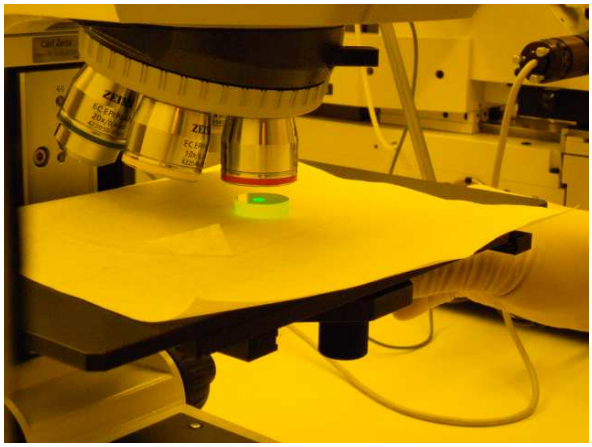

Figure A.10: Checking of the mirror surface

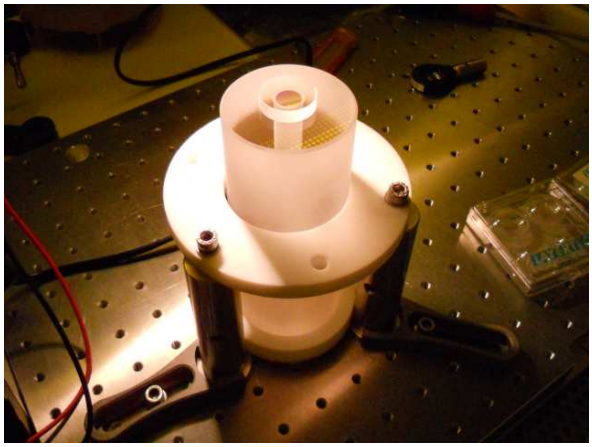

Figure A.11: Finished optical contacting

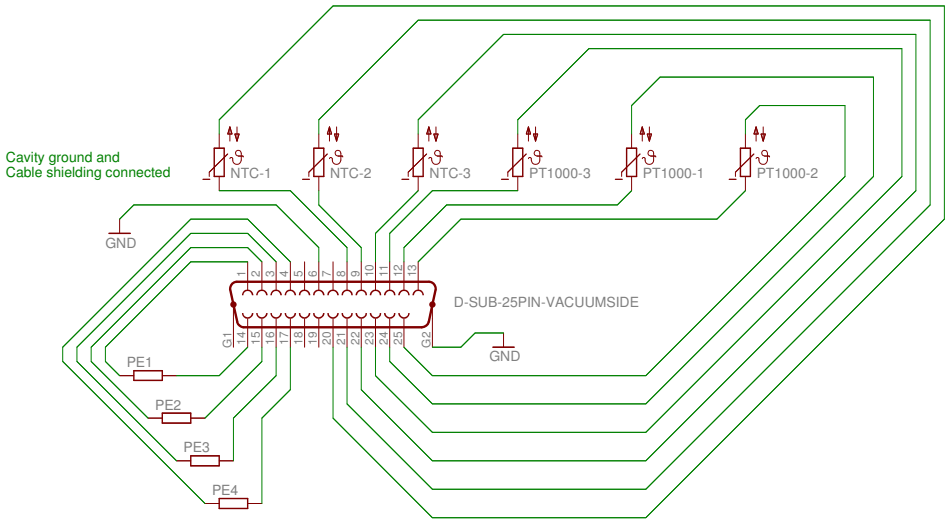

Figure A.12: Electric connections inside the vacuum chamber

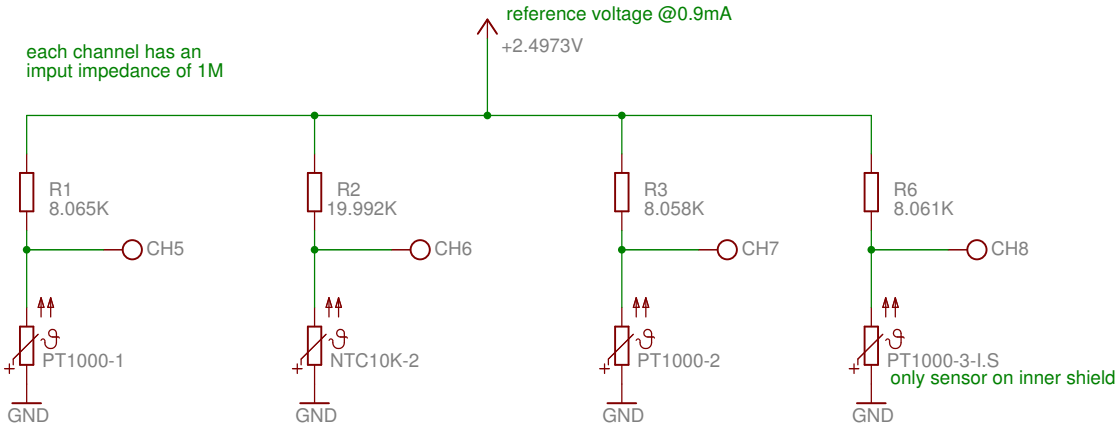

Figure A.13: The measurement bridge used for temperature monitoring with the Pico data logger.

Appendix B

Electronics

In this Section, diagrams of several electronic circuits used are shown.

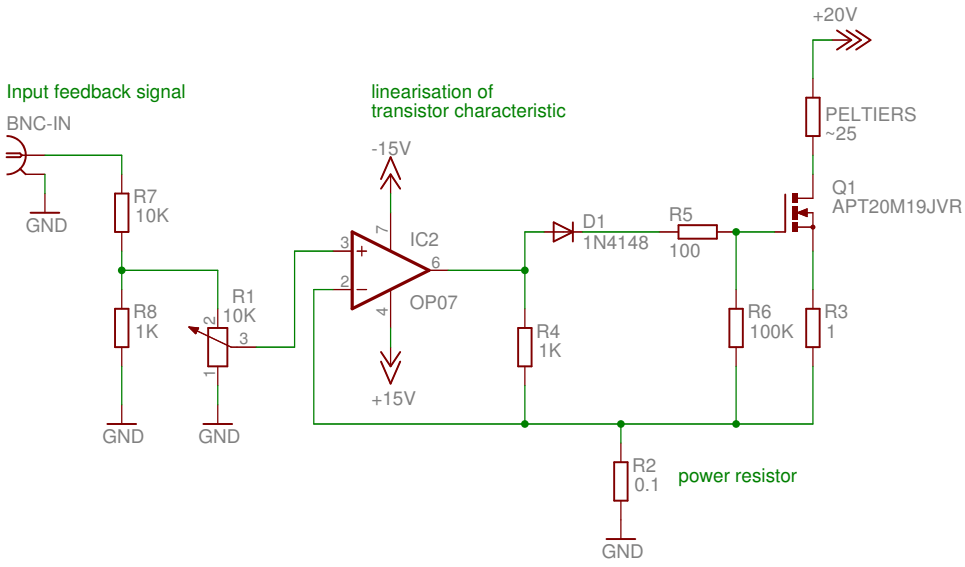

Figure B.1: The current output stage.

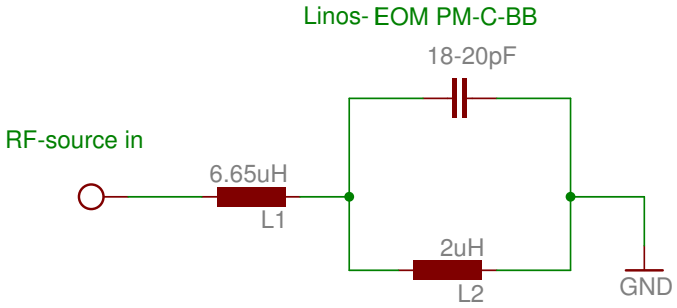

Figure B.2: Resonant circuit for amplifying the voltage drop over the EOM. The inductances are self-wound toroidal coils suited for HF-applications. The circuit is resonant at 31 MHz.

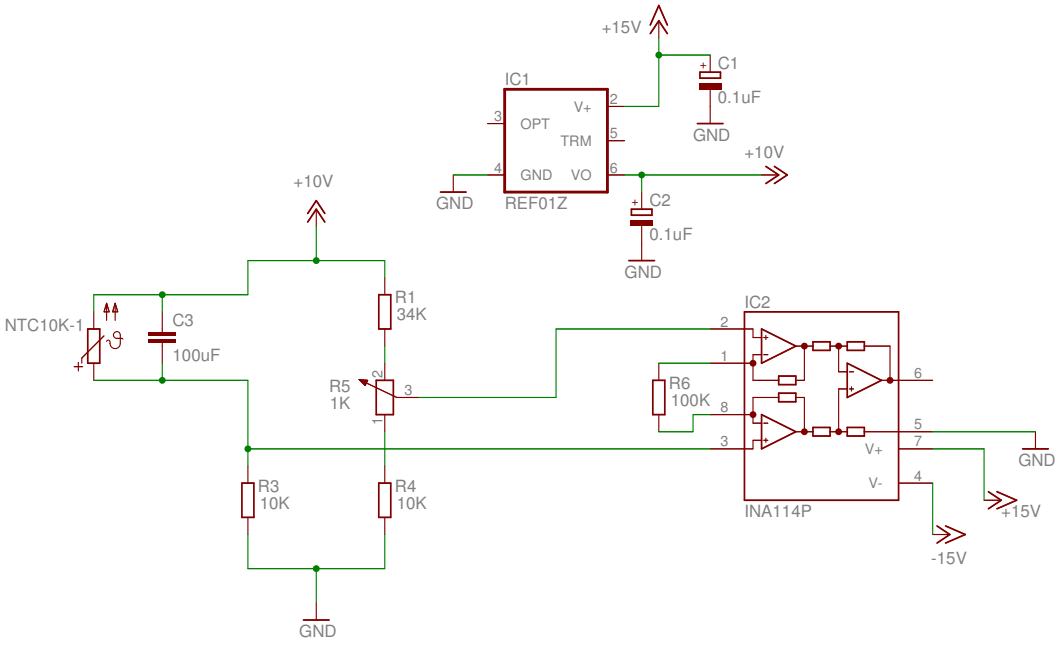

Figure B.3: The measurement bridge used for the control of the Peltier elements.

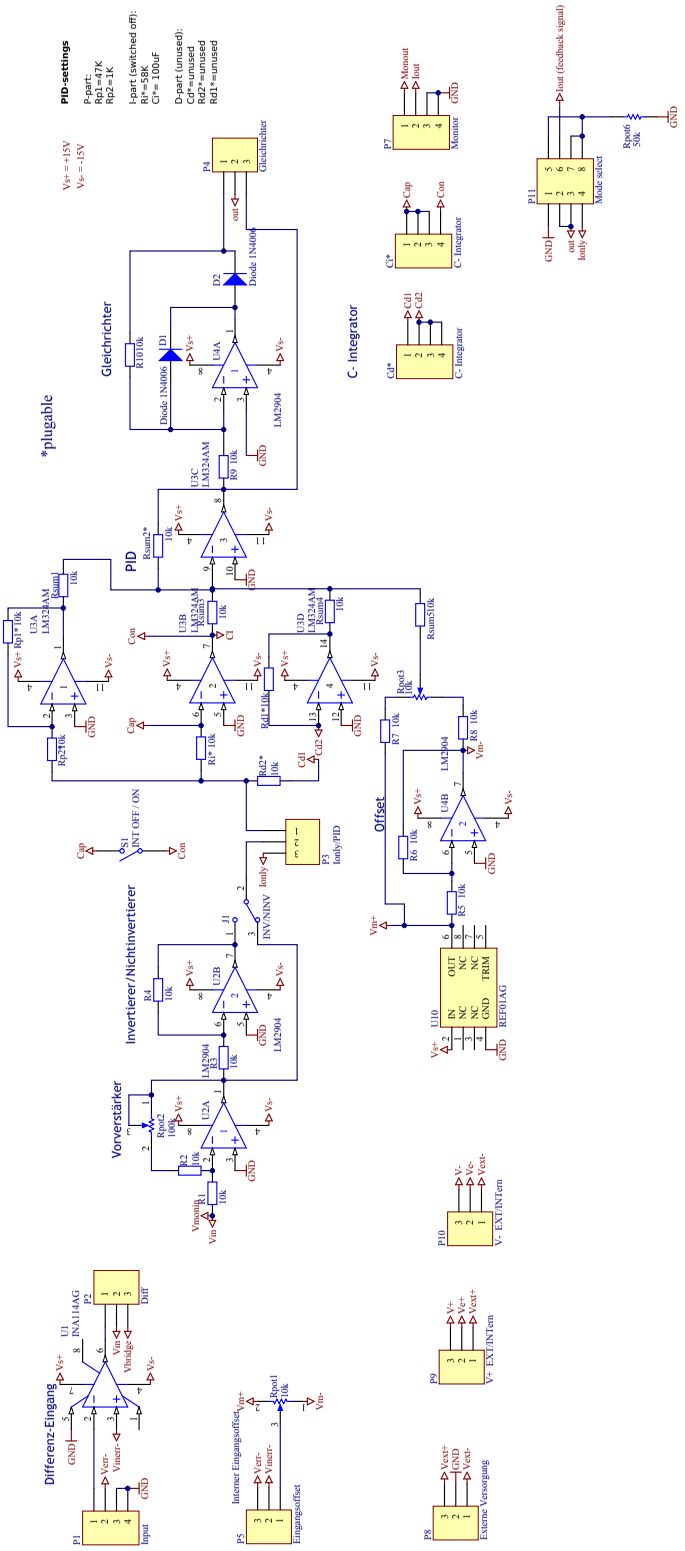

Figure B.4: The temperature PI controller used for the control of the cavity temperature. This controller is made by our electronic workshop and modified by myself.

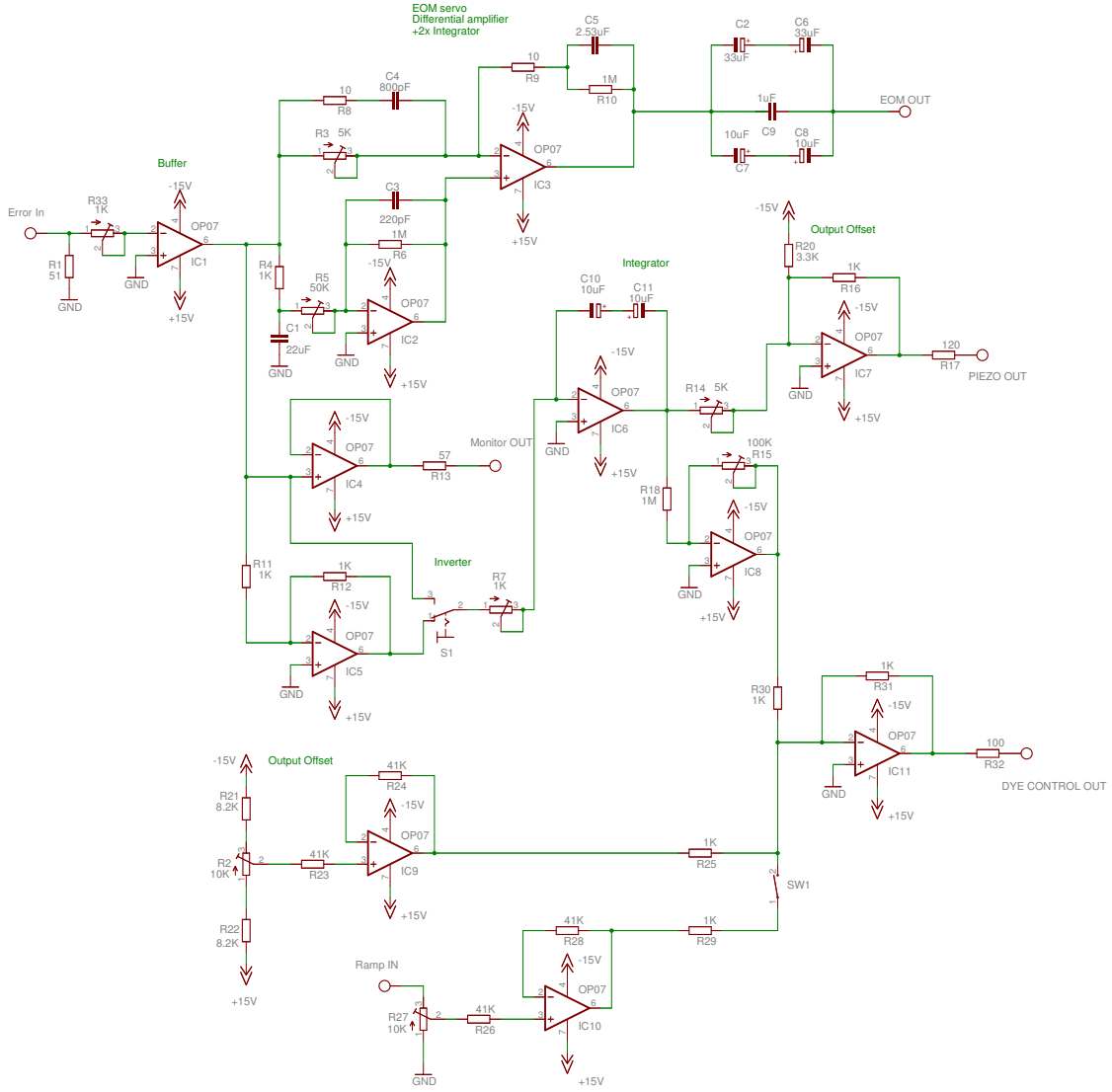

Figure B.5: Dye servo. The servo is used to apply feedback onto the EOM, the piezo mirror and the galvo plate of the dye laser.

Appendix C

Hyperfine structure of the fermionic isotope

For calculation of the energy E of hyperfine states of the ^{167}Er isotope, we use the following formula [Ari77]

$$\begin{aligned} E[J,F] &= A\frac{K}{2} + B\frac{3K(K+1) - 4I(I+1)J(J+1)}{8I(2I-1)J(2J-1)}, \\ K &= F(F+1) - J(J+1) - I(I+1). \end{aligned} \tag{C.1}$$

Here, A and B are the hyperfine constants, which are known for the ground state and the excited 583 nm state. They are taken from Refs. [Smi65, Chi83], and have the values $A_{\mathrm{GS}} = -120.4864\,\mathrm{MHz}$, $B_{\mathrm{GS}} = -4552.959\,\mathrm{MHz}$, $A_{583} = -172.5\,\mathrm{MHz}$, $B_{583} = -4440\,\mathrm{MHz}$. The nuclear spin quantum number is $I = 7/2$. For the ground state, we have $J = 6$ and F ranging from 5/2 to 19/2, whereas for the excited state we have $J = 7$ and F' ranging from 7/2 to 21/2. In first order, only transitions having $F' - F = \Delta F = 0, +1, -1$ are allowed. The corresponding frequency shifts are calculated by

$$\Delta E = E[J = 7, F'] - E[J = 6, F] - \delta E, \tag{C.2}$$

where $\delta E = -335.2\,\mathrm{MHz}$ is the shift of the unperturbed ^{167}Er transition relative to the the transition of ^{166}Er at 583 nm [Jin90]. Figure C.1 shows all the transitions $F \to F'$ for the 583-nm line.

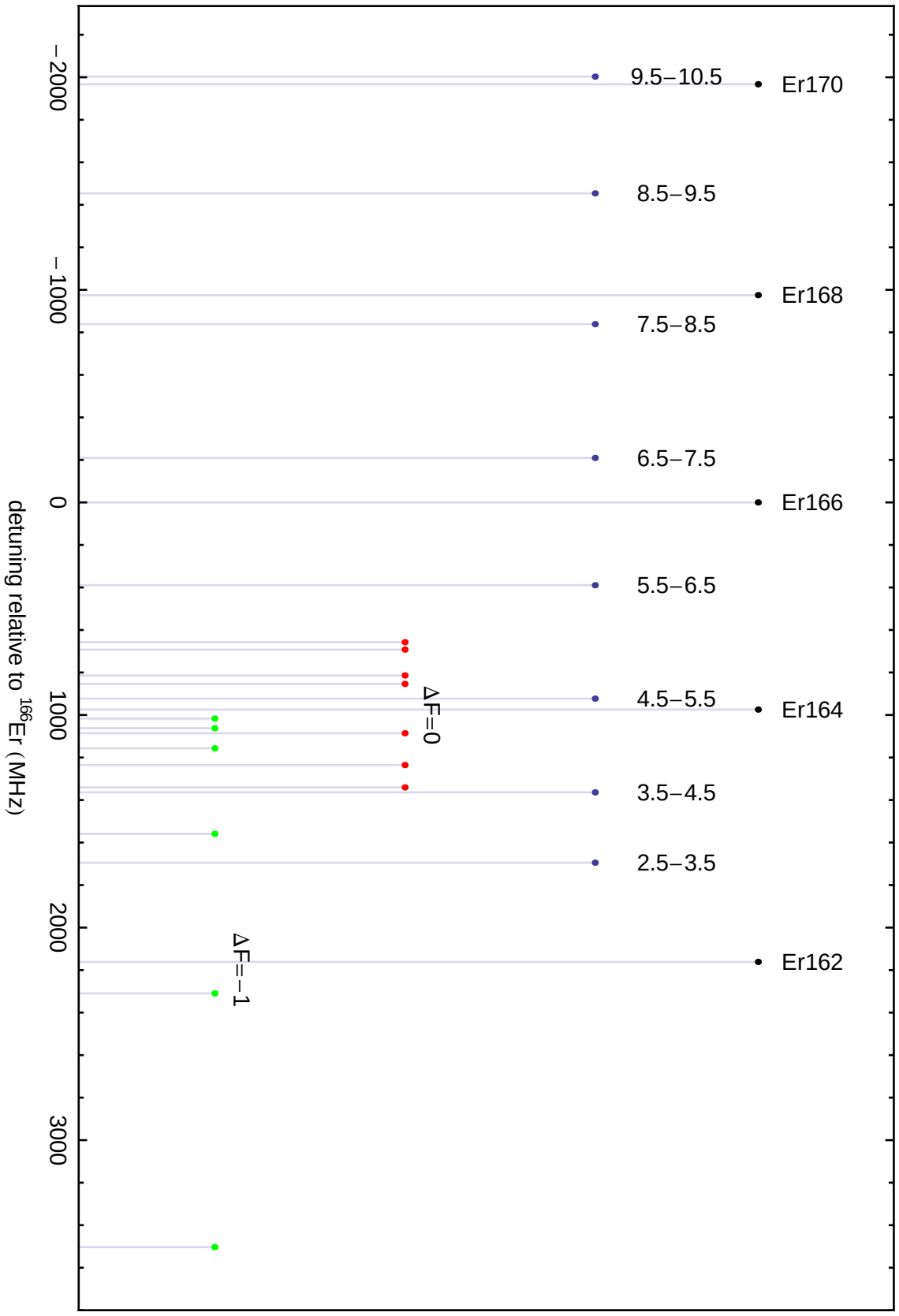

Figure C.1: Erbium hyperfine structure at 583 nm.

Appendix D

PRL: Narrow-line magneto-optical trap for erbium

Narrow-line magneto-optical trap for erbium

A. Frisch,[1] K. Aikawa,[1] M. Mark,[1] A. Rietzler,[1] J. Schindler,[1] E. Zupanič,[1,2] R. Grimm,[1,3] and F. Ferlaino[1]
[1]*Institut für Experimentalphysik and Zentrum für Quantenphysik, Universität Innsbruck, Technikerstraße 25, A-6020 Innsbruck, Austria*
[2]*Jožef Stefan Institute, Jamova 39, SI-1000 Ljubljana, Slovenia*
[3]*Institut für Quantenoptik und Quanteninformation, Österreichische Akademie der Wissenschaften, A-6020 Innsbruck, Austria*
(Received 7 March 2012; published 7 May 2012)

We report on the experimental realization of a robust and efficient magneto-optical trap for erbium atoms, based on a narrow cooling transition at 583 nm. We observe up to $N = 2 \times 10^8$ atoms at a temperature of about $T = 15\ \mu$K. This simple scheme provides better starting conditions for direct loading of dipole traps as compared to approaches based on the strong cooling transition alone, or on a combination of a strong and a narrow kHz transition. Our results on Er point to a general, simple, and efficient approach to laser cool samples of other lanthanide atoms (Ho, Dy, and Tm) for the production of quantum-degenerate samples.

DOI: 10.1103/PhysRevA.85.051401 PACS number(s): 37.10.De, 67.85.−d, 37.10.Vz

Laser cooling of non-alkali-metal atoms has become a very active and challenging field of research. The great appeal of unconventional atomic systems for experiments on ultracold atomic quantum gases stems from the possibility of engineering complex interactions and of accessing rich atomic energy spectra. Both features are at the foundation of a number of novel and fascinating phenomena. For instance, the energy spectra of two-valence-electron species, such as alkaline-earth-metal and alkaline-earth-metal-like atoms, feature narrow and ultranarrow optical transitions, which are key ingredients for ultraprecise atomic clocks [1], efficient quantum computation schemes [2], and novel laser cooling approaches, as demonstrated in experiments with Sr, Yb, and Ca [3–5].

As a next step in complexity, multivalence-electron atoms with a non-S electronic ground state such as lanthanides are currently attracting increasing experimental and theoretical interest. Among many, one of the special features of lanthanides is the exceptionally large magnetic dipole moment of atoms in the electronic ground state (e.g., $7\mu_B$ for Er and $10\mu_B$ for both Dy and Tb), which provides a unique chance to study strongly dipolar phenomena with atoms. Highly magnetic atoms interact with each other not only via the usual contact interaction but also via an anisotropic and long-range interaction, known as the dipole-dipole interaction [6]. Chromium was the first atomic species used for experiments on atomic dipolar quantum gases [7,8], and the even more magnetic lanthanides are nowadays in the limelight thanks to laser cooling experiments on Er and Tm [9,10] and to the recent realization of quantum-degenerate Dy gases [11,12].

Similarly to Yb and the alkaline-earth-metal atoms, the atomic energy spectra of magnetic lanthanides include broad, narrow, and ultranarrow optical transitions. This collection of lines is reflected in a wide choice of possible schemes for laser cooling experiments. However, all experiments on Zeeman slowing and cooling in a magneto-optical trap (MOT) with magnetic lanthanides so far have relied on an approach that is essentially based on the strongest cycling transition [9,10,13]. This broad transition typically lies in the *blue* between 400 and 430 nm and has a linewidth on the order of few tens of MHz. As a consequence, the Doppler temperature is close to 1 mK. Such a high temperature makes direct loading from a MOT into a dipole trap difficult and inefficient, even when sub-Doppler mechanisms take place [14,15]. To further decrease the temperature of atoms prior to the dipole trap loading, an additional MOT stage based on an ultranarrow kHz-linewidth transition was applied in Refs. [11,13], making the whole experimental procedure more involved.

Taking advantage of the rich atomic spectrum of lanthanides, we identify a different transition to be the most suitable one for MOT operation toward production of a quantum-degenerate gas. This transition, which for Er lies at 583 nm and has a linewidth of 190 kHz, represents an intermediate case between the broad (blue) and the ultranarrow (red) transitions available in the lanthanide spectra and has very similar properties to the Yb intercombination line [16,17]. Based on this narrow yellow line, we demonstrate a MOT of 2×10^8 Er atoms at a temperature as low as 15 μK. Our approach, inspired by Yb experiments [4], provides better starting conditions for direct loading into a dipole trap than the conditions achieved in other experiments with magnetic lanthanides [11].

Erbium is a heavy rare-earth element of the lanthanide series. It has six stable isotopes, among which the three bosonic isotopes ^{166}Er (34%), ^{168}Er (27%), and ^{170}Er (15%) and the fermionic isotope ^{167}Er (23%) have a high natural abundance. The Er electronic configuration is characterized by a xenonlike core, an inner open $4f$ shell, and an outer closed $6s$ shell, $[\mathrm{Xe}]4f^{12}6s^2$. The electron vacancies in the inner f shell are a common feature of all the lanthanides (with the exception of Yb) and are at the origin of the strong magnetism as well as various interesting collisional effects [18–20].

The atomic level spectrum of Er is shown in Fig. 1. In the ground state, Er has a highly anisotropic electronic density distribution with a large orbital angular momentum $L = 5$ (H state) and a total electronic angular momentum $J = 6$. The bosonic isotopes have zero nuclear spin ($I = 0$) and consequently do not exhibit a hyperfine structure. On the contrary, the fermionic isotope ^{167}Er has a nuclear spin $I = 7/2$, leading to eight hyperfine levels, from $F = 5/2$ to $F = 19/2$, in the electronic ground state.

In Ref. [22], five different $J \rightarrow J + 1$ laser cooling transitions were identified with linewidths ranging from tens of MHz to a few Hz. Here we focus on the blue and

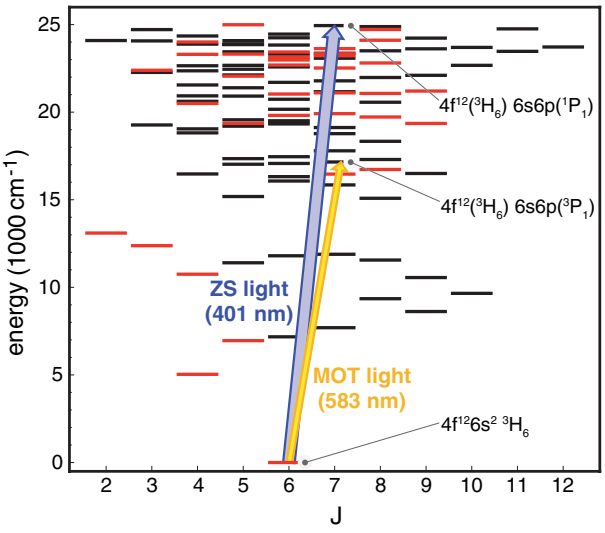

FIG. 1. (Color online) Energy levels of atomic erbium up to 25 000 cm^{-1} for different total electronic angular momentum quantum numbers J [21]. States with odd (even) parity are indicated by black (red/gray) horizontal lines. The two relevant laser cooling transitions at 401 and 583 nm are indicated by arrows [22].

the yellow transition at 401 and 583 nm, respectively; see the arrows in Fig. 1. The corresponding excited levels are the singlet $^1P_1$ and triplet $^3P_1$ states coming from the transition of an s electron into a p shell. The strong blue transition at 401 nm has a linewidth of $\Gamma_{401}/2\pi = 27.5$ MHz [23], corresponding to a Doppler temperature of $\hbar\Gamma_{401}/(2k_B) = 660\,\mu$K. We use the blue light for both Zeeman slowing and transversal cooling of the Er atomic beam. The MOT operates on the narrow yellow transition at 583 nm, which has a natural linewidth of $\Gamma_{583}/2\pi = 190$ kHz and a corresponding Doppler temperature of 4.6 μK. The line may exhibit weak leaks from the excited level into two intermediate levels with very low calculated leakage rates (0.017 and 0.0049 s^{-1}) [22]. Note that we find these losses irrelevant for all practical purposes. For ^{167}Er the hyperfine structure in the 401- and 583-nm excited states gives rise to eight levels ranging from $F' = 7/2$ to $F' = 21/2$. For the 583-nm line, the hyperfine constants are known [26]. On the contrary the hyperfine constants for the 401-nm line are currently unknown, making the operation of the fermionic MOT more challenging.

We generate the blue light from two independent blue diode lasers injection locked to a master laser. The master laser light is produced by frequency doubling methods based on a tapered amplified diode laser at 802 nm. The blue light from the master laser is locked to a hollow-cathode discharge lamp [4] via modulation transfer spectroscopy. With this setup we spectroscopically resolve the lines of the four most abundant bosonic isotopes as well as the hyperfine structure of the fermionic isotope ^{167}Er. Since the hyperfine constants of the excited level at 401 nm are unknown, we could not assign the absorption features to specific hyperfine transitions. We derive the yellow light from a dye laser operating with Rhodamin 6G. By using an intracavity electro-optic modulator (EOM) and an external reference cavity, we stabilize the laser to a linewidth of about 50 kHz. By additionally locking the laser to an ultralow-expansion cavity, we achieve a long-term stability better than 30 kHz within a day [27].

Our experimental procedure is as follows. We load the Zeeman slowed atomic beam from an effusive, high-temperature oven directly into the narrow-line MOT. Our commercial oven typically operates at a temperature of 1300 °C, which is about 200 °C below the Er melting point. Two 3-mm apertures, separated by 50 mm, provide a geometrical collimation of the atomic beam. In addition, the atomic beam is further collimated and transversally cooled by a two-dimensional (2D) optical molasses, working on the broad 401-nm transition with a total power of about 100 mW. The beams are elliptically shaped to increase the interaction time between the atoms and the light. Thanks to the transversal cooling stage, we increase the loading flux by almost an order of magnitude.

The atomic beam then enters the Zeeman slower (ZS). Because of the limited capture velocity (a few m/s) imposed by the narrow cooling transition used for the MOT, it is crucial to design a ZS that provides enough atomic flux at low velocities [4]. We build a 360-mm-long spin-flip Zeeman slower, which can slow the atoms from 500 to about 5 m/s. The ZS light is focused at the oven position and has a total power of about 60 mW. At the MOT position, we estimate a beam diameter of about 11 mm, corresponding to an intensity of about one $I_{s,401}$, where $I_{s,401} = 56$ mW/cm^2 is the saturation intensity. Our ZS operates with light detuned by about $-20\Gamma_{401}$ (-540 MHz) from the unshifted resonance.

The narrow-line MOT is operated in a standard six-beam configuration with retroreflected beams. To increase the capture velocity of the MOT, we use large MOT beam diameters of about 30 mm. Typical MOT loading parameters include a magnetic field gradient B' (along the symmetry axis) of 4 G/cm, a laser intensity of $12I_{s,583}$ per beam with $I_{s,583} = 0.13$ mW/cm^2, and a detuning δ_{583} from the atomic transition of $-50\Gamma_{583}$ (-9.5 MHz). To measure the number of atoms in the MOT after loading, we optically compress the MOT by reducing δ_{583} to $-0.5\Gamma_{583}$ and we apply standard absorption imaging on the blue transition.

A special feature of our narrow-line MOT is the large detuning of the MOT light (typically $-50\Gamma_{583}$) needed for optimal loading. At this detuning, we observe a very strong effect of gravity on the position and shape of the atom cloud [3]. The atoms are located well below the center of the magnetic quadrupole field, and the cloud takes the form of a large semishell. To elucidate the reason for the large detuning, we monitor the loading dynamics and the lifetime of the MOT; see Fig. 2. Our measurements focus on the ^{166}Er isotope, but we have observed the same qualitative behavior also for the other isotopes.

Figure 2(a) shows the atom number in the MOT as a function of the loading time for different values of δ_{583}. We fit our data by using a standard loading rate equation [28], which includes a capture rate R and a decay rate γ; the latter accounts for both collisions between trapped atoms and collisions with the background gas. For a detuning of $-50\Gamma_{583}$ the atom number approaches its steady state in about 10 s with $N_{ss} \approx 2 \times 10^8$. For a lower value of the detuning

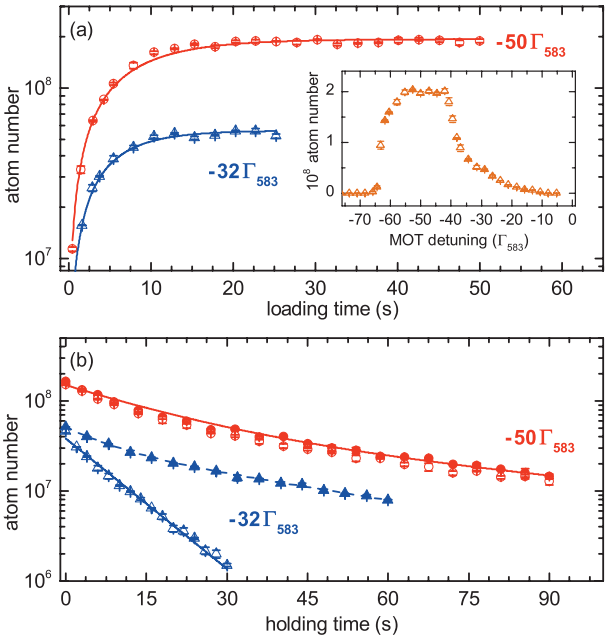

FIG. 2. (Color online) Loading (a) and decay (b) of the narrow-line MOT with ^{166}Er atoms for $\delta_{583} = -50\Gamma_{583}$ (circles) and $\delta_{583} = -32\Gamma_{583}$ (triangles). (a) Atom numbers are plotted as a function of the MOT loading time. The solid lines are fits to the data using $N(t) = N_{ss}(1 - e^{-\gamma t})$ with $N_{ss} = R/\gamma$. From the fits we obtain $\gamma = 0.137(2)$ s^{-1}, $R = 2.6(4) \times 10^7$ s^{-1}, and $\gamma = 0.200(4)$ s^{-1}, $R = 1.1(1) \times 10^7$ s^{-1} for $-50\Gamma_{583}$ and $-32\Gamma_{583}$, respectively. The inset shows the atom number after 10-s loading time as a function of the MOT detuning. (b) Atom numbers are plotted as a function of the holding time in the MOT in presence (open symbols) and absence of the ZS light (solid symbols). The solid lines are fits to the data using a double-exponential function; see text.

to $-32\Gamma_{583}$ we observe a substantial decrease of the atom number to $N_{ss} \approx 5 \times 10^7$. This behavior is clearly shown in the inset, where we monitor the number of atoms N_{ss} for a fixed loading time of 10 s as a function of the MOT light detuning. For detunings exceeding $\delta_{583} = -30\Gamma_{583}$ we observe a rapid increase in the atom number. When further increasing the detuning, N_{ss} first stays constant and then rapidly decreases.

We believe that the large detuning of the MOT light serves to minimize the detrimental effects of off-resonant pumping processes driven by the ZS light. According to the Zeeman shift in the quadrupole field of the MOT, we observe a spatial displacement of the atomic cloud with δ_{583} of about 1.4 mm/MHz [29]. For large detunings, this shift becomes so large that the atoms can no longer be kept in the MOT. For intermediate detunings in the range from -40 to $-55\Gamma_{583}$, the cloud displacement is advantageous for MOT operation since the atoms become spatially separated from the region of interaction with the ZS light. For small detunings, the ZS light leads to substantial losses of atoms.

The effect of the ZS light also shows up in lifetime measurements, where we monitor the number of atoms in the MOT as a function of the holding time with the ZS light being present or absent; see Fig. 2(b). For these measurements we switch off the ZS magnetic field and the atomic beam after 10 s of MOT loading. For large detuning ($\delta_{583} = -50\Gamma_{583}$) the evolution of the atom number is not affected by the ZS light. In both cases, i.e., with the ZS light on and off, we observe faster losses in the earlier stage of the decay, which we attribute to inelastic two-body collisional processes, and a slower decay at a later time, which is finally limited by background collisions. For simplicity we use a double-exponential fit function to estimate the time constants [30]. We extract time constants of 19(3) and 80(20) s for the fast and slow dynamics, respectively. At lower MOT detuning ($-32\Gamma_{583}$), the ZS light strongly affects the decay. When the blue light is turned off, our observations are qualitatively similar to the ones at $-50\Gamma_{583}$ while with the blue light turned on the atomic loss dramatically increases. In this case the decay curve is well described by a single exponential function with a time constant $\tau = 9.0(1)$ s. This decay time is consistent with a simple estimate of pumping losses. By considering the absorption rate Γ_a of the 401-nm light at the actual intensity and detuning [31] and the branching ratio b for decay from the excited state to all the possible metastable states [9], we estimate a decay rate $1/\tau = b\Gamma_a$ of the order of 0.1 s^{-1}.

We could also demonstrate trapping of all the other Er isotopes, with the exception of the rare ^{162}Er (0.1% natural abundance). For all the bosonic isotopes we used about the same values for the detuning of the ZS and the MOT light. Figure 3(a) shows the atom number in the MOT for the different isotopes as a function of their natural abundance. For a long loading time of 20 s we observe similar atom numbers exceeding 10^8 for the three most abundant bosonic isotopes, indicating that saturation effects might apply. For a short loading time of 5 s, the atom number increases with the natural abundance. However, we observe a more complicated

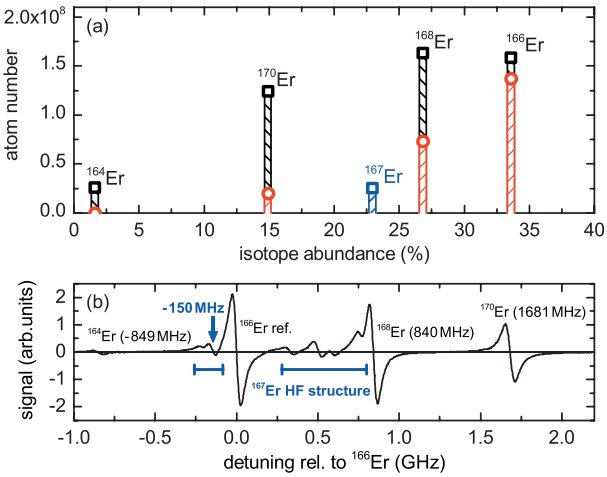

FIG. 3. (Color online) Behavior of different Er isotopes. (a) MOT atom number for the four most abundant bosonic isotopes as well as for the ^{167}Er fermionic isotope is plotted as a function of the natural abundance for 20-s (squares) and 5-s (circles) loading times. (b) Spectroscopy signal of the blue transition shows the isotope shifts for the bosonic isotopes and the HF structure of ^{167}Er. The arrow indicates the locking point used for the ZS light to produce the ^{167}Er MOT.

behavior than the expected linear growth. This might be due to slight differences in the optimal MOT parameters, but may also point to differences in scattering and collisional properties among the different isotopes.

For the fermionic isotope ^{167}Er we observe a MOT with atom number of about 3×10^7, which is substantially lower than the numbers measured for the bosonic isotopes. A simple explanation of this behavior can be that we decelerate and cool only atoms in the $F = 19/2$ hyperfine state, which has a statistical weight of about 20%. Note that a similar behavior has been observed with the fermionic ^{161}Dy MOT, which also shows lower atom numbers than the ones of bosonic MOTs [13]. An additional complication stems from the unknown hyperfine splitting of the 401-nm line. From the spectroscopic signal we could not identify *a priori* where to lock the Zeeman slower light to be resonant with the desired $F = 19/2 \rightarrow F' = 21/2$ hyperfine transition. To produce the ^{167}Er MOT, we had to proceed blindly by first locking the 583-nm MOT light on the cooling transition and then by trying different locking points for the ZS light until the MOT was visible. We finally succeed in creating a MOT by locking the ZS light to the spectroscopic line located 150 MHz below the blue transition frequency of the ^{166}Er isotope; see the arrow in Fig. 3(b).

After loading the MOT we apply a stage of compression to reduce the temperature of the atomic cloud and to achieve good starting conditions for direct loading of an optical dipole trap. With the optimized parameters $\delta_{583} = -0.5\Gamma_{583}$, $I = 0.16 I_{s,583}$, and $B' = 0.8$ G/cm, we measure a temperature of 15 μK via time-of-flight experiments. In addition, Stern-Gerlach experiments indicate that atoms in the compressed MOT phase are naturally pumped in the lowest Zeeman sublevel $m_J = -6$ by the MOT light. This can be explained by considering a combined effect of the narrow cooling transition used for the MOT and of gravity. The latter pushes the atoms downward, creating an effective imbalance in the trap and leading to a preferential absorbtion of the σ^- polarized light from the lower vertical beam. For 2×10^8 atoms at $T = 15\ \mu$K we estimate a peak number density of the polarized sample of 1.5×10^{11} cm^{-3}, corresponding to a phase-space density of about 4×10^{-6}. These values are similar to the ones observed in Yb experiments using the intercombination light [4]. Compared to other experiments on magnetic lanthanides, such as Dy [11], our much simpler approach based on a single cooling light for the MOT provides higher atom numbers and similar final temperatures. We suggest that this scheme can be successfully implemented with Dy, Ho, and Tm, using the 626-nm ($\Gamma/2\pi = 135$ kHz) [32], the 598-nm ($\Gamma/2\pi = 146$ kHz) [33], and the 531-nm ($\Gamma/2\pi = 370$ kHz) [34] transitions, respectively.

In conclusion, we have demonstrated an efficient and simple approach for an Er MOT based on a single narrow-line transition. Our scheme works with all abundant Er isotopes and allows for direct loading of an optical dipole trap. In first experiments we were able to load up to 10^7 Er atoms into the dipole trap in a single focused-beam configuration. Optimization of the dipole trap loading and evaporative cooling experiments are under way in our laboratory.

We are grateful to J. J. McClelland and A. J. Berglund for sharing with us their knowledge on Er and to S. Kotochigova, O. Dulieu, M. Lepers, and J. F. Wyart for fruitful discussions. We also thank the Sr team in Innsbruck and the Yb team in Tokyo for their support. This work is supported by the Austrian Ministry of Science and Research (BMWF) and the Austrian Science Fund (FWF) through a START grant under Project No. Y479-N20 and by the European Research Council under Project No. 259435.

[1] T. Ido and H. Katori, Phys. Rev. Lett. **91**, 053001 (2003).
[2] A. J. Daley, M. M. Boyd, J. Ye, and P. Zoller, Phys. Rev. Lett. **101**, 170504 (2008).
[3] H. Katori, T. Ido, Y. Isoya, and M. Kuwata-Gonokami, Phys. Rev. Lett. **82**, 1116 (1999).
[4] T. Kuwamoto, K. Honda, Y. Takahashi, and T. Yabuzaki, Phys. Rev. A **60**, R745 (1999).
[5] E. A. Curtis, C. W. Oates, and L. Hollberg, Phys. Rev. A **64**, 031403 (2001).
[6] T. Lahaye, C. Menotti, L. Santos, M. Lewenstein, and T. Pfau, Rep. Prog. Phys. **72**, 126401 (2009).
[7] A. Griesmaier, J. Werner, S. Hensler, J. Stuhler, and T. Pfau, Phys. Rev. Lett. **94**, 160401 (2005).
[8] Q. Beaufils, R. Chicireanu, T. Zanon, B. Laburthe-Tolra, E. Maréchal, L. Vernac, J.-C. Keller, and O. Gorceix, Phys. Rev. A **77**, 061601 (2008).
[9] J. J. McClelland and J. L. Hanssen, Phys. Rev. Lett. **96**, 143005 (2006).
[10] D. Sukachev, A. Sokolov, K. Chebakov, A. Akimov, S. Kanorsky, N. Kolachevsky, and V. Sorokin, Phys. Rev. A **82**, 011405 (2010).
[11] M. Lu, N. Q. Burdick, S. H. Youn, and B. L. Lev, Phys. Rev. Lett. **107**, 190401 (2011).
[12] M. Lu, N. Q. Burdick, and B. L. Lev, e-print arXiv:1202.4444.
[13] S. H. Youn, M. Lu, U. Ray, and B. L. Lev, Phys. Rev. A **82**, 043425 (2010).
[14] A. J. Berglund, J. L. Hanssen, and J. J. McClelland, Phys. Rev. Lett. **100**, 113002 (2008).
[15] D. Sukachev, A. Sokolov, K. Chebakov, A. Akimov, N. Kolachevsky, and V. Sorokin, JETP Lett. **92**, 703 (2010).
[16] Y. Takasu, K. Honda, K. Komori, T. Kuwamoto, M. Kumakura, Y. Takahashi, and T. Yabuzaki, Phys. Rev. Lett. **90**, 023003 (2003).
[17] Y. Takasu, K. Maki, K. Komori, T. Takano, K. Honda, M. Kumakura, T. Yabuzaki, and Y. Takahashi, Phys. Rev. Lett. **91**, 040404 (2003).
[18] R. V. Krems, G. C. Groenenboom, and A. Dalgarno, J. Phys. Chem. A **108**, 8941 (2004).
[19] C. B. Connolly, Y. S. Au, S. C. Doret, W. Ketterle, and J. M. Doyle, Phys. Rev. A **81**, 010702 (2010).
[20] S. Kotochigova and A. Petrov, Phys. Chem. Chem. Phys. **13**, 19165 (2011).

[21] Y. Ralchenko, A. Kramida, J. Reader, and N. A. Team, NIST Atomic Spectra Database, 2011.
[22] H. Y. Ban, M. Jacka, J. L. Hanssen, J. Readerand, and J. J. McClelland, Opt. Express **13**, 3185 (2005).
[23] In Ref. [24] a linewidth of $\Gamma_{401}/2\pi = 36$ MHz has been measured via fluorescence spectroscopy on atomic beams while in Ref. [25] a value of $\Gamma_{401}/2\pi = 29.5$ MHz has been obtained from lifetime measurements. We measure a linewidth of 27.5(4) MHz by using an absorption imaging technique on magneto-optically trapped atoms in the regime of low saturation parameters.
[24] J. J. McClelland, Phys. Rev. A **73**, 064502 (2006).
[25] J. E. Lawler, J.-F. Wyart, and E. A. D. Hartog, J. Phys. B **43**, 235001 (2010).
[26] W. J. Childs, L. S. Goodman, and V. Pfeufer, Phys. Rev. A **28**, 3402 (1983).
[27] Although we could clearly observe the spectroscopic signals for the different Er isotopes using a hollow-cathode lamp, we prefer to lock the 583-nm light to an ultralow-expansion cavity in order to reach higher-frequency stability.
[28] J. Weiner, V. S. Bagnato, S. Zilio, and P. S. Julienne, Rev. Mod. Phys. **71**, 1 (1999).
[29] The atomic cloud displacement Δ_x from the trap center is given by $\Delta\mu B'\Delta_x = \hbar\Delta_{583}$, where $\Delta\mu$ is the difference in magnetic moments between the ground and excited state.
[30] The standard rate equation approach is problematic, because the distorted (semishell) shape of the MOT makes it difficult to extract reliable values for the density and because the MOT may be in the high-density limit regime [28].
[31] H. J. Metcalf and P. van der Straten, *Laser Cooling and Trapping* (Springer, New York, 1999).
[32] M. Lu, S. H. Youn, and B. L. Lev, Phys. Rev. A **83**, 012510 (2011).
[33] M. Saffman and K. Mølmer, Phys. Rev. A **78**, 012336 (2008).
[34] D. Sukachev, K. Chebakov, A. Sokolov, A. Akimov, N. Kolachevsky, and V. Sorokin, Opt. Spectrosc. **111**, 633 (2011).

Bibliography

[Aik12] K. Aikawa, A. Frisch, M. Mark, S. Baier, A. Rietzler, R. Grimm, and F. Ferlaino, *Bose-Einstein Condensation of Erbium*, Phys. Rev. Lett. **108**, 210401 (2012).

[Aln08] J. Alnis, A. Matveev, N. Kolachevsky, T. Udem, and T. W. Hänsch, *Subhertz linewidth diode lasers by stabilization to vibrationally and thermally compensated ultralow-expansion glass Fabry-Pérot cavities*, Phys. Rev. A **77**, 053809 (2008).

[And95] M. H. Anderson, J. R. Ensher, M. R. Matthews, C. E. Wieman, and E. A. Cornell, *Observation of Bose-Einstein Condensation in a Dilute Atomic Vapor*, Science **269**, 198 (1995).

[Ari77] E. Arimondo, M. Inguscio, and P. Violino, *Experimental determinations of the hyperfine structure in the alkali atoms*, Rev. Mod. Phys. **49**, 31 (1977).

[Ban05] H. Ban, M. Jacka, J. Hanssen, J. Reader, and J. McClelland, *Laser cooling transitions in atomic erbium.*, Opt. Express **13**, 3185 (2005).

[Bar08] M. Baranov, *Theoretical progress in many-body physics with ultracold dipolar gases*, Phys. Rep. **464**, 71 (2008).

[Bea08] Q. Beaufils, R. Chicireanu, T. Zanon, B. Laburthe-Tolra, E. Maréchal, L. Vernac, J.-C. Keller, and O. Gorceix, *All-optical production of chromium Bose-Einstein condensates*, Phys. Rev. A **77**, 061601 (2008).

[Ber08] A. Berglund, J. Hanssen, and J. McClelland, *Narrow-Line Magneto-Optical Cooling and Trapping of Strongly Magnetic Atoms*, Phys. Rev. Lett. **100**, 113002 (2008).

[Bir05] K. Birnbaum, *Ultra-High Vacuum Chambers* (2005), available online at `http://www.scribd.com/doc/78125406/UHV-Chambers-Birnbaum` (30 Sept. 2005).

[Bla98] E. Black, *Notes on the Pound-Drever-Hall Technique*, Technical Notes of the LIGO Project (1998).

[Bon86] B. Bonarev and S. Kobtsev, *Calculation and optimization of a birefringent filter for a cw dye laser*, Opt. Spektrosk. **60**, 814 (1986).

[Bra95] C. Bradley, C. Sackett, J. Tollett, and R. Hulet, *Evidence of Bose-Einstein Condensation in an Atomic Gas with Attractive Interactions*, Phys. Rev. Lett. **75**, 1687 (1995).

[Che06] L. Chen, J. Hall, J. Ye, T. Yang, E. Zang, and T. Li, *Vibration-induced elastic deformation of Fabry-Perot cavities*, Phys. Rev. A **74**, 053801 (2006).

[Chi83] W. Childs, L. Goodman, and V. Pfeufer, *Hyperfine structure of the* $4f^{12}6s^2\,{}^3H$ *and* ${}^3F$ *terms of* ${}^{167}Er$ *I by atomic-beam, laser-rf double resonance*, Phys. Rev. A **28**, 3402 (1983).

[Chi06] J. K. Chin, D. E. Miller, Y. Liu, C. Stan, W. Setiawan, C. Sanner, K. Xu, and W. Ketterle, *Evidence for superfluidity of ultracold fermions in an optical lattice*, Nature **443**, 961 (2006).

[Con10] C. B. Connolly, Y. S. Au, S. C. Doret, W. Ketterle, and J. M. Doyle, *Large spin relaxation rates in trapped submerged-shell atoms*, Phys. Rev. A **81**, 010702 (2010).

[Cor08] Corning, *ULE Product information sheet* (2008), available online at `http://www.corning.com/specialtymaterials/products_capabilities/ULE.aspx` (2008).

[CVI09] CVI Melles Griot, *Sources of Vibration - CVI Melles Griot Technical Guide* (2009), available online at `http://www.cvimellesgriot.com/products/Documents/TechnicalGuide/Sources_of_Vibration.pdf` (2009).

[Dav95] K. B. Davis, M. Mewes, M. R. Andrews, N. J. van Druten, D. S. Durfee, D. M. Kurn, and W. Ketterle, *Bose-Einstein Condensation in a Gas of Sodium Atoms*, Phys. Rev. Lett. **75**, 3969 (1995).

[DeM99] B. DeMarco and D. Jin, *Onset of Fermi degeneracy in a trapped atomic gas*, Science **285**, 1703 (1999).

[Dem03] W. Demtröder, *Laser spectroscopy: basic concepts and instrumentation*, Springer Verlag (2003).

[Dem05] W. Demtröder, *Experimentalphysik 3, Atome, Moleküle und Festkörper*, Springer Verlag (2005).

[Den10] E. a. Den Hartog, J. P. Chisholm, and J. E. Lawler, *Radiative lifetimes of neutral erbium*, Journal of Physics B: Atomic, Molecular and Optical Physics **43**, 155004 (2010).

[Don05] E. a. Donley, T. P. Heavner, F. Levi, M. O. Tataw, and S. R. Jefferts, *Double-pass acousto-optic modulator system*, Rev. Sci. Instrum. **76**, 063112 (2005).

[Dra96] G. W. Drake, *Atomic, Molecular, and Optical Physics Handbook*, AIP (1996).

[Esc09] Y. de Escobar, P. G. Mickelson, M. Yan, B. J. Desalvo, S. B. Nagel, and T. C. Killian, *Bose-Einstein Condensation of* ^{84}Sr, Phys. Rev. Lett. **103**, 200402 (2009).

[Fer10] F. Ferlaino and R. Grimm, *Forty years of Efimov physics: How a bizarre prediction turned into a hot topic*, Physics **3**, 9 (2010).

[Foo05] C. Foot, *Atomic physics*, Oxford University Press (2005).

[Fri12] A. Frisch, K. Aikawa, M. Mark, A. Rietzler, J. Schindler, E. Zupanič, R. Grimm, and F. Ferlaino, *Narrow-line magneto-optical trap for erbium*, Phys. Rev. A **85**, 051401 (2012).

[Gre08] M. Greiner, *Optical lattices*, Nature **453**, 736 (2008).

[Gri05] A. Griesmaier, J. Werner, S. Hensler, J. Stuhler, and T. Pfau, *Bose-Einstein Condensation of Chromium*, Phys. Rev. Lett. **94**, 160401 (2005).

[Han04] C. I. Hancox, S. C. Doret, M. T. Hummon, and L. Luo, *Magnetic trapping of rare-earth atoms at millikelvin temperatures*, Nature **431**, 281 (2004).

[Jac06] J. D. Jackson, *Klassische Elektrodynamik (german edition)*, Walter de Gruyter, 4th edition (2006).

[Jin90] W. Jin, T. Horiguchi, M. Wakasugi, and Y. Yoshizawa, *Hyperfine Structure and Isotope Shift in Er I by the Atomic-Beam Laser Spectroscopy*, J. Phys. Soc. Jpn. **59**, 3148 (1990).

[Kir06] G. Kirchmair, *Frequency stabilization of a Titanium-Sapphire laser for precision spectroscopy on Calcium ions* (2006), diploma thesis, available online at `http://heart-c704.uibk.ac.at/publications/diploma/diplom_kirchmair.pdf`.

[Kra09] S. Kraft, F. Vogt, O. Appel, F. Riehle, and U. Sterr, *Bose-Einstein Condensation of Alkaline Earth Atoms:* ^{40}Ca, Phys. Rev. Lett. **103**, 130401 (2009).

[Lah08] T. Lahaye, J. Metz, B. Fröhlich, T. Koch, M. Meister, A. Griesmaier, T. Pfau, H. Saito, Y. Kawaguchi, and M. Ueda, *d-Wave Collapse and Explosion of a Dipolar Bose-Einstein Condensate*, Phys. Rev. Lett. **101**, 080401 (2008).

[Lah09] T. Lahaye, *The physics of dipolar bosonic quantum gases*, Rep. Prog. Phys. **72** (2009).

[Leg10] T. Legero, T. Kessler, and U. Sterr, *Tuning the thermal expansion properties of optical reference cavities with fused silica mirrors*, J. Opt. Soc. Am. B **27**, 914 (2010).

[Lip93] R. J. Lipert and S. C. Lee, *Isotope shifts and hyperfine structure of erbium, dysprosium, and gadolinium by atomic-beam diode-laser spectroscopy*, Appl. Phys. B **58**, 85 (1993).

[Lu11] M. Lu, N. Q. Burdick, S. H. Youn, and B. L. Lev, *Strongly Dipolar Bose-Einstein Condensate of Dysprosium*, Phys. Rev. Lett. **107**, 190401 (2011).

[Mar78] W. Martin, R. Zalubas, and L. Hagan, *Atomic Energy Levels: The Rare-earth Elements*, NSRDS-NBS, U.S. Government Printing Office (1978).

[McC06a] J. McClelland, *Natural linewidth of the 401-nm laser-cooling transition in ErI*, Phys. Rev. A **73**, 064502 (2006).

[McC06b] J. McClelland and J. Hanssen, *Laser cooling without repumping: a magneto-optical trap for erbium atoms*, Phys. Rev. Lett. **96**, 143005 (2006).

[McC08] D. J. McCarron, S. a. King, and S. L. Cornish, *Modulation transfer spectroscopy in atomic rubidium*, Meas. Sci. Tech. **19**, 105601 (2008).

[Met99] H. J. Metcalf and P. van der Straten, *Laser Cooling and Trapping*, Springer, New York (1999).

[Ome03] Omega, *Table of Total Emissivity* (2003), available online at `http://www.monarchserver.com/TableofEmissivity.pdf` (2003).

[Osp10] S. Ospelklaus, K. K. Ni, D. Wang, M. H. G. de Miranda, B. Neyenhuis, G. Quemener, P. Julienne, J. L. Bohn, D. S. Jin, and J. Ye, *Quantum-State Controlled Chemical Reactions of Ultracold Potassium-Rubidium Molecules*, Science **327**, 853 (2010).

[Pet02] C. Pethick and H. Smith, *Bose-Einstein Condensation in Dilute Gases*, Cambridge University Press (2002).

[Py09] Z. Peng-yi, X. Zhuan-xian, L. Yun, and H. E. Ling-xiang, *Realization of Green MOT for Ytterbium Atoms*, Chin. Phys. Lett. **26**, 083702 (2009).

[Rad11] Radiant Dyes, *Dye Tuning Curves and Dye Efficiency of Narrow Scan* (2011), available online at `http://www.radiant-dyes.com/images/stories/RDL/Laser_Dyes/dye_spectrum.png` (2011).

[Raj80] R. Raj, D. Bloch, J. Snyder, and G. Camy, *High-frequency optically heterodyned saturation spectroscopy via resonant degenerate four-wave mixing*, Phys. Rev. Lett. **44**, 1251 (1980).

[Sch01] F. Schreck, G. Ferrari, K. Corwin, J. Cubizolles, L. Khaykovich, M. Mewes, and C. Salomon, *Sympathetic cooling of bosonic and fermionic lithium gases towards quantum degeneracy*, Phys. Rev. A **64**, 011402 (2001).

[Sie02] R. Siegel and J. Howell, *Thermal radiation heat transfer*, volume 1, Taylor & Francis (2002).

[Smi65] K. Smith and P. Unsworth, *The hyperfine structure of* ^{167}*Er and magnetic moments of* ^{143,145}*Nd and* ^{167}*Er by atomic beam triple magnetic resonance*, Proc. Phys. Soc **86**, 1249 (1965).

[Ste09] S. Stellmer, M. K. Tey, B. Huang, R. Grimm, and F. Schreck, *Bose-Einstein Condensation of Strontium*, Phys. Rev. Lett. **103**, 200401 (2009).

[Tie99] U. Tietze, *Halbleiterschaltungstechnik (german edition)*, Springer Verlag, 11 edition (1999).

[Tru01] A. G. Truscott, K. E. Strecker, W. I. McAlexander, G. B. Partridge, and R. G. Hulet, *Observation of Fermi Pressure in a Gas of Trapped Atoms*, Science **291**, 2570 (2001).

[Wyb07] B. Wybourne and L. Smentek, *Optical spectroscopy of lanthanides: magnetic and hyperfine interactions*, CRC Press (2007).

[Yam08] A. Yamaguchi, *Metastable State of Ultracold and Quantum Degenerate Ytterbium Atoms : High-Resolution Spectroscopy and Cold Collisions* (2008), PhD thesis, available online at `http://yagura.scphys.kyoto-u.ac.jp/publications/thesis/PhD_yamaguchi.pdf`.